RESISTIVE Z-PINCH EQUILIBRIA AND STABILITY

BY

IAN DENNIS CULVERWELL

BLACKETT LABORATORY
IMPERIAL COLLEGE
LONDON

THESIS SUBMITTED FOR THE DEGREE OF DOCTOR OF PHILOSOPHY OF THE UNIVERSITY OF LONDON AND FOR THE DIPLOMA OF MEMBERSHIP OF IMPERIAL COLLEGE

OCTOBER 1989

ABSTRACT

Theoretical work is presented on the effects of resistivity in a Z-pinch.

Two new classes of time-dependent resistive Z-pinch equilibria are described in detail. The stationary equilibria in the first class are sustained by a rising current, those in the second expand while carrying a falling current. A wide spectrum of equilibria is found, from models of gas-embedded pinches to thermally isolated pinches confined by skin currents at the plasma edge.

The stability of the stationary equilibria in the ideal MHD regime is studied.

Resistive Z-pinch stability is studied numerically by using an initial-value code. This work demonstrates that a Z-pinch can be stable to $m = 0$ and $m = 1$ perturbations in the low current regime. It is shown that this result can at least partly explain the enhanced stability observed in some Z-pinch experiments.

The compressional Z-pinch experiment at Imperial College is modelled using a one-dimensional Lagrangian code. It is thereby shown to be anomalously stable.

CONTENTS

Title page 1

Abstract 2

Contents 3

Acknowledgements 5

The role of the author in this work 6

Chapter one: Introduction

1.1 Introduction 8

1.2 Review 8

1.3 Ideal MHD 10

1.4 Resistive MHD 16

1.5 Summary and outline of thesis 21

Chapter two: Time-dependent Z-pinch equilibria

2.1 Separable solutions 22

2.2 Stationary equilibria: $v = 0$ 23

2.2.(i) Zero thermal conductivity 25

2.2.(ii) Finite thermal conductivity 28

2.2.(iii) Infinite thermal conductivity 30

2.3 Non-stationary equilibria: $v = r/t$ 35

2.3.(i) Zero thermal conductivity 37

2.3.(ii) Finite thermal conductivity 37

2.3.(iii) Infinite thermal conductivity 40

2.4 Discussion and conclusions 42

Chapter three: The ideal MHD stability of time-dependent equilibria

3.1 The validity of ideal MHD at high temperatures 46

3.2 The effect of thermal conductivity 46

3.3 The boundary condition in the presence of skin currents 47

3.4 The effect on stability of a skin current 52

3.5 Discussion and conclusions 55

Chapter four: The development of axisymmetric ($m = 0$) perturbations in the resistive regime

4.1 Introduction 57

4.2 Equations and boundary conditions 58
4.3 Details of the numerical scheme 60
4.4 Tests of the numerical scheme 65
4.5 Results 67
4.6 Discussion and conclusions 72

Chapter five: The development of helical (m = 1) perturbations in the resistive regime
5.1 Introduction 77
5.2 Equations and boundary conditions 77
5.3 Details of the numerical scheme 79
5.4 Tests of the numerical scheme 85
5.5 Results 86
5.6 Discussion and conclusions 91

Chapter six: The inverse skin effect and its occurrence in the compressional pinch
6.1 The inverse skin effect 94
6.2 Lagrangian code modelling 95
6.3 A simple example: linear current fall 95
6.3.(i) t_o = 100 ns 95
6.3.(ii) t_o = 10 ns 97
6.3.(iii) t_o = 1 ns 99
6.4 The compressional pinch 102
6.5 Discussion and conclusions 105

Chapter seven: Conclusions and discussion
7.1 Introduction 109
7.2 Chapter one 109
7.3 Chapter two 110
7.4 Chapter three 111
7.5 Chapter four 111
7.6 Chapter five 113
7.7 Chapter six 113

References 115

ACKNOWLEDGEMENTS

It is a pleasure to thank the following for their help:

Prof. M. G. Haines, my supervisor, for his support and his interest in this work, and for obtaining an SERC 'Instant Award' to sustain me during its execution;
Dr. M. Coppins, without whose enthusiasm, encouragement and unfailing good humour much of the work described here could hardly have begun;
AERE Harwell, my employers, for granting me leave of absence to perform this work;
P. Baldock for a detailed description of the Imperial College compressional pinch experiment;
Dr. A. R. Bell for the use of his Lagrangian code and for many valuable suggestions concerning the numerical solution of initial-value problems;
Dr. A. K. L. Dymoke-Bradshaw for the use of his graphics routine GPLOT;
Dr. G. J. Rickard for his help with the Lagrangian code and the shooting code;
Drs. A. E. Robson, J. D. Sethian and F. L. Cochran (Naval Research Laboratory, Washington DC, USA) for detailed descriptions of their experiments and for many illuminating discussions on the Z-pinch;
and all the members of the Plasma Physics group at Imperial College who have made this experience more enjoyable than it would otherwise have been.

THE ROLE OF THE AUTHOR IN THIS WORK

Much of the work contained in this thesis was performed while the author was under the close supervision of Dr. M. Coppins (Imperial College). Although this collaboration benefitted all of the work described here, some parts are entirely the work of Dr. Coppins. These are: the original derivation of the stationary separable solutions in section 2.2 of chapter two; the physical interpretation of the solutions in section 2.4; the MHD boundary condition in the presence of skin currents (section 3.3, chapter three); and the recognition that the constant radius observed in the compressional pinch experiment could be used to estimate its rate of cooling (section 6.5, chapter six).

The shooting code used in chapter three was originally written by Dr. C. Davies (Imperial College), although the implementation of the revised boundary condition of section 3.3 was the work of the author. Similarly the one-dimensional Lagrangian code employed in chapter six was originally written by Dr. A. R. Bell, developed by Dr. G. J. Rickard (both from Imperial College), and modified to include the effects of end losses (section 6.4) by the author.

The use of perturbed kinetic energy to measure the amplitude of a perturbation (chapters four and five) was originally suggested by Dr. A. E. Robson (Naval Research Laboratory, Washington DC, USA).

To the memory of my father;
and for my mother, without whose unfailing support none of this would have been possible.

CHAPTER ONE

INTRODUCTION

1.1 Introduction

This chapter begins with a brief review of the history of the Z-pinch in order to explain the motivation behind the work contained in this thesis. There follows a short review of ideal magnetohydrodynamics (MHD), the simplest possible theory of plasma behaviour in Z-pinch geometry, concentrating on those aspects of the theory that are relevant to the work of later chapters. The complexities that arise from the addition of resistivity to the basic model are then summarised. The chapter concludes with an outline of the rest of the thesis.

1.2 Review

The pure Z-pinch is probably the simplest possible plasma containment device, consisting of a column of plasma held in balance against the radially outward pressure by the combined action of an axial current j_z with its induced magnetic induction B_θ (figure 1.1). The pinching effect of this inwardly directed force was first analysed theoretically by Bennett (1934) and Tonks (1939). Previously, Atkinson and Houtermans (1929) had suggested that thermonuclear reactions between protons at high temperatures were the source of the sun's energy. The conjunction of these two ideas – that a pinched electrical discharge could liberate abundant energy if it could contain plasma at high enough temperatures and densities for sufficiently long (quantitative conditions for this effect to occur being given by Lawson in 1957) – led to a programme of vigorous experimental research into the Z-pinch (Thonemann 1950, Cousins and Ware 1951).

It soon became apparent, however, that the simple Z-pinch suffers from gross, short-timescale catastrophic instabilities (Carruthers and Davenport 1957) as well as severe particle (and therefore energy) end losses. Thus, in spite of the need for complicated and expensive auxiliary heating sources and external magnetic field coils (none of which are needed for the self-contained, high-β Z-pinch), research turned towards toroidal fusion devices such as the tokamak and the

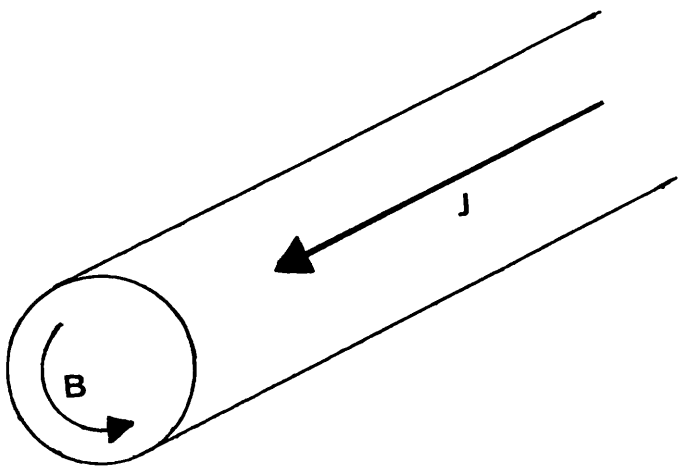


Figure 1.1 The pure Z-pinch.

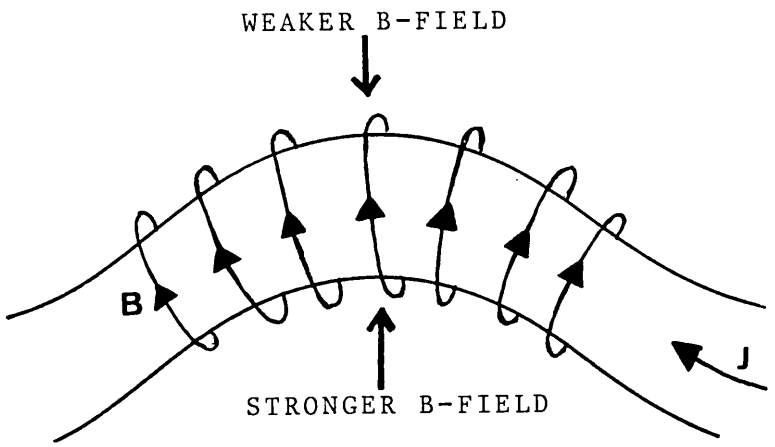


Figure 1.2 Physical mechanism of the m = 1 instability.

stellarator.

Following more recent developments in high−current, high−voltage pulse technology the simple high density Z−pinch has become fashionable once more (Haines 1982, Robson 1984) and the need for a detailed theoretical description of Z−pinch behaviour has become apparent. This is particularly true in the light of recent very encouraging experimental results from high density pinches made from frozen deuterium fibres (Hammel and Scudder 1987, Sethian *et. al.* 1987) which appear to show enhanced stability while the pinch current is rising. The main purpose of this thesis is to attempt to understand and explain the 'anomalous' stability seen in these and other experiments.

1.3 Ideal MHD

Ideal magnetohydrodynamics (MHD) is the simplest possible model of large scale, low frequency plasma behaviour in Z−pinch geometry. In ideal MHD the plasma is represented as a fluid, the equations describing its behaviour being obtained by taking moments over velocity space of the equations describing the evolution of the ion and electron distribution functions. If the 'plasma approximation' of quasi−neutrality is made, and the limit $m_e/m_i \rightarrow 0$ is taken, then the ion and electron fluid equations can be combined to produce a set of single fluid equations that are given, for example by Freidberg (1982, pp 808 − 809).

By defining the variables

$$x = (m_i/m_e)^{1/2} V_{Ti} \tau_{ii} / a \qquad (1.1)$$

and

$$y = a_i / a \qquad (1.2)$$

where V_{Ti} is the ion thermal velocity, τ_{ii} is the ion−ion collision time, a_i is the ion Larmor radius, and a is the plasma length scale perpendicular to the $\underline{B}$ field, Freidberg was able to show that under the approximations of: (a) high collisionality ($x << 1$), (b) small ion Larmor radius ($y << 1$), and (c) low resistivity ($y^2/x << 1$) the following *ideal MHD equations* are valid:

Continuity: $\partial\rho/\partial t + \nabla.(\rho\underline{v}) = 0$ (1.3)

Equation of motion: $\rho\, d\underline{v}/dt - \underline{j} \wedge \underline{B} + \nabla p = \underline{0}$ (1.4)

Ohm's law: $\underline{E} + \underline{v} \wedge \underline{B} = \underline{0}$ (1.5)

Energy equation: $d\,(p / \rho^{\Gamma}) / dt = 0$ (1.6)

Faraday's law: $\nabla \wedge \underline{E} + \partial\underline{B} / \partial t = \underline{0}$ (1.7)

Ampere's law: $\nabla \wedge \underline{B} - \mu_o \underline{j} = \underline{0}$ (1.8)

In the above, $d/dt = \partial/\partial t + \underline{v}.\nabla$ is the convective derivative, Γ is the adiabatic index and the other symbols have their usual meanings.

There are two commonly used types of boundary condition for these equations. Fixed boundary conditions apply when the plasma is contained by perfectly conducting walls. In this case the standard electromagnetic boundary conditions enforce the continuity of the tangential component of the electric field and the normal component of the magnetic field across the plasma−wall interface. Free boundary conditions apply when the plasma is surrounded by a vacuum. In general there are discontinuities in the pressure and the tangential magnetic field across the boundary; integration of the equation of motion (1.4) across the moving plasma surface shows that in this case the appropriate boundary condition is given by the continuity of the total (thermal plus magnetic) pressure across the plasma−vacuum boundary (Goedbloed 1979 p 28).

The utility of ideal MHD was first proved in 1954 by Kruskal and Schwarzchild who used it to give a theoretical prediction of the 'm = 1' helical instability observed experimentally by Carruthers and Davenport in 1957. This mode of instability is illustrated in figure 1.2; its physical mechanism is as follows. Following a helical perturbation the magnetic field lines concentrate on the inside of the curve leading to an increased magnetic pressure there. Thus the perturbation is enhanced and the system is unstable. Another instability, the 'm = 0' or 'sausage' instability shown in figure 1.3. In this case, following an axisymmetric perturbation, the magnetic pressure is increased at neck due to the smaller radius there. Since the plasma is free to squeeze into the bulbous regions the perturbation develops and the system is unstable. These two modes are found

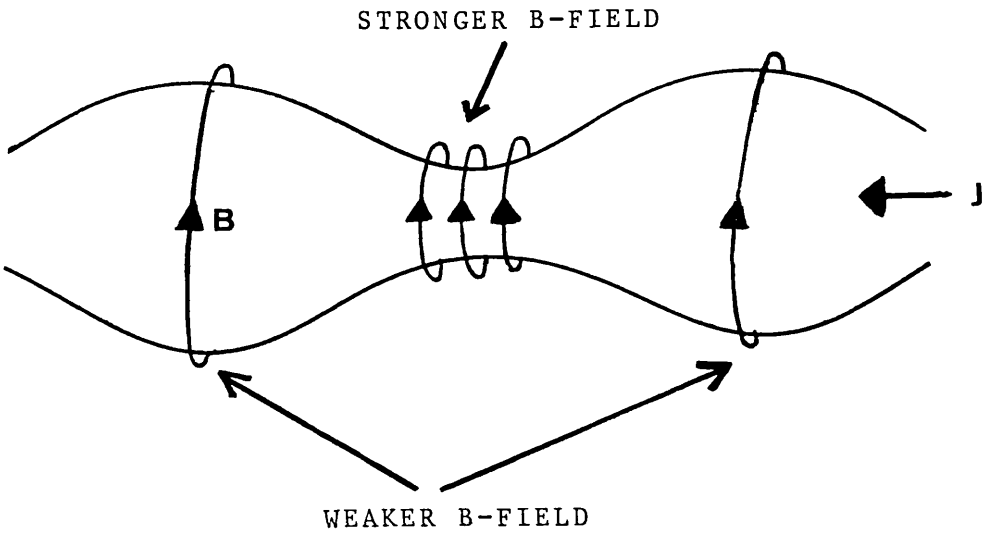


Figure 1.3 Physical mechanism of the m = 0 instability.

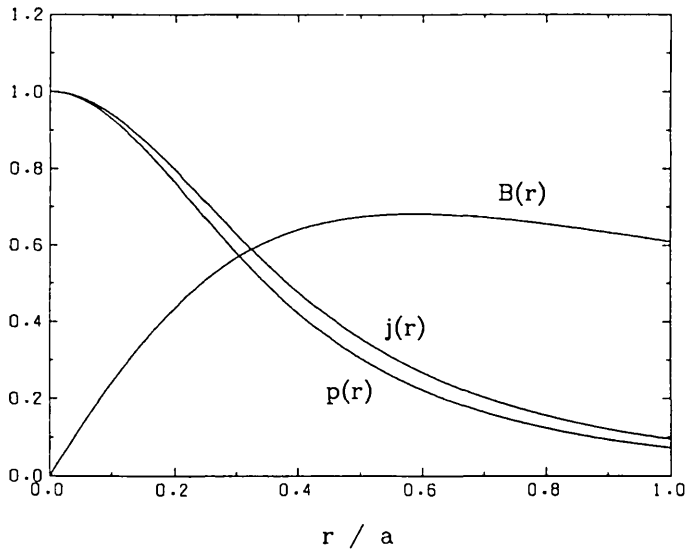


Figure 1.4 Marginally Kadomtsev stable profiles of pressure, current density and magnetic field. j(r) normalised w.r.t j(0), p(r) w.r.t. p(0), B(r) w.r.t. $\sqrt{(\mu_o p(0))}$, arbitrary length scale.

to be the most unstable both experimentally and theoretically (Tayler 1957a).

The conventional approach in ideal MHD stability theory is to linearise eqns. 1.3 to 1.8 and then to assume that the first order perturbed variables have the time dependence exp(iωt). This procedure leads to the linear ideal MHD equation of motion (Bernstein *et. al.* 1958):

$$\rho^0 \, \partial^2 \underline{\xi}/\partial t^2 \;=\; -\,\rho^0 \omega^2 \underline{\xi} \;=\; \underline{F}[\underline{\xi}] \qquad (1.9)$$

where $\underline{\xi}(\underline{r}, t)$ is the plasma displacement and the *ideal MHD force operator* $\underline{F}$ is defined by:

$$\mu_o \underline{F}[\underline{\xi}] = [\nabla \wedge \nabla \wedge (\underline{\xi} \wedge \underline{B}^0)] \wedge \underline{B}^0 + (\nabla \wedge \underline{B}^0) \wedge [\nabla \wedge (\underline{\xi} \wedge \underline{B}^0)]$$

$$+ \mu_o \nabla (\underline{\xi}.\nabla p^0 + \Gamma p^0 \nabla.\underline{\xi}), \qquad (1.10)$$

the superscripts '0' denoting equilibrium variables.

It can be shown that $\underline{F}$ is a *self−adjoint* operator (Goedbloed 1979 p 120) which implies that (e.g. Mathews and Walker 1970 p 263): (a) the eigenvalues, $-\omega_n^2$, of $\underline{F}[\underline{\xi}_n] = -\rho^0 \omega_n^2 \underline{\xi}_n$ are real; and (b) eigenfunctions $\underline{\xi}_n$ belonging to different eigenvalues are orthogonal. The first result implies that ω is either purely real (stable oscillations) or purely imaginary (exponential instability), i.e. there is no overstability in ideal MHD. The second result says that:

$$1/2 \int \underline{\xi}_n^* \cdot \underline{\xi}_m \, \rho^0 \, d^3r \;=\; 0 \qquad (1.11)$$

if $\omega_n^2 \neq \omega_m^2$, the integral being over the entire plasma volume.

The spectrum of the operator $\underline{F}$ has been studied in general by Goedbloed and Sakanaka (1974) and with particular reference to the Z−pinch by Appert *et. al.* (1974) and Kanellopoulos *et. al.* (1988). These works demonstrated that the stable side of the spectrum of $\underline{F}$ could contain *continua* (where the operator $\underline{F}$ becomes singular somewhere inside the plasma), and that there could be more than one unstable eigenmode for a given equilibrium configuration and perturbation wavelength. This is important: the existence of a collection of unstable eigenfunctions, each orthogonal to each of the others, will be used later in chapters four and five.

Since MHD instabilities are catastrophic when they occur, it is often sufficient to know if a particular configuration is stable or not, precise details of the growth rate and eigenfunction structures being superfluous. Bernstein *et. al.* (1958) showed that it was possible to determine precisely this by applying the *energy principle:* an equilibrium is linearly stable in ideal MHD theory if and only if $W[\underline{\xi}] > 0$ for all plasma displacements $\underline{\xi}(\underline{r}, t)$ bounded in energy and satisfying the appropriate boundary conditions. Here

$$W[\underline{\xi}] = -(1/2) \int \underline{\xi}.\underline{F}[\underline{\xi}]\, d^3r, \qquad (1.12)$$

which can be identified as the plasma potential energy. The sufficiency of the energy principle follows from the exact, non−linear energy conservation expressed in the ideal MHD force equation and boundary conditions: if the potential energy of the plasma increases following *any* perturbation then the system's kinetic energy can never increase and the system is stable. The necessity of the energy principle was first proved by Laval *et. al.* in 1965.

The energy principle was first applied to Z−pinches by Kadomtsev in 1966. He showed that for $m = 0$ modes the integrand of eqn. 1.12 could be written as a quadratic form in ξ_r and div $\underline{\xi}$, and that this form is positive definite i.e. the equilibrium is *unconditionally stable to m = 0 perturbations* if and only if

$$-(r/p^0)\, dp^0/dr < 4\Gamma/(2 + \Gamma\beta(r)) \qquad (1.13a)$$

where
$$\beta(r) = 2\mu_0 p^0(r)/B^{0\,2}(r). \qquad (1.13b)$$

This is the $m = 0$ Kadomtsev stability criterion. Note its lack of dependence on the axial wavelength of the perturbation. Marginally stable profiles of pressure, current density and magnetic field are shown in figure 1.4. Any equilibrium with a steeper pressure profile is unstable to $m = 0$ perturbations according to this criterion.

It is possible to use the same procedure to find a sufficient condition for stability to $m \geq 1$ modes, although in this case it is only a necessary condition for short wavelength ($\lambda \to 0$) modes:

$$d \log(B^0/r) \,/\, d \log r < (m^2 - 4)/2 \qquad (1.14)$$

Therefore a Z−pinch with a finite current density on axis is always unstable to m

= 1 modes, since in that case $B^0(r) \propto r$ for small r. Since $4\Gamma/(2 + \Gamma\beta) < 4/\beta$, eqns. 1.13 and 1.14, together with the pressure balance condition $\partial p^0/\partial r = -(B^0/\mu_0 r)\partial(rB^0)/\partial r$, show that a Z-pinch stable to m = 0 modes is stable to m > 1 modes as well, thus justifying the neglect of these highly twisted modes in the rest of this thesis.

The concrete calculation of instability growth rates and eigenfunctions is readily effected once it is realized that in Z-pinch geometry eqn. 1.9 can be rewritten as a pair of coupled ODEs for the total perturbed pressure $p^* = p^1 + \underline{B}^0 \cdot \underline{B}^1/\mu_0$ and the quantity $r\xi_r$ (Bateman 1978 pp 109 - 112, following earlier work by Appert *et. al.* in 1974). [This assumes a Fourier decomposition in space, all perturbed variables varying as exp (ikz - imθ), where m is integral and k is real. This explains the nomenclature of m = 0 and m = 1 to describe axisymmetric and helical perturbations. Since z and θ are ignorable coordinates in Z-pinch equilibria any perturbation may be decomposed into a sum of such modes, each evolving independently.] The resulting system of equations may be written as:

$$d\underline{f}/dr = M(m, k, p^0, \underline{B}^0, \omega^2)\ \underline{f} \qquad (1.15)$$

where $\underline{f} = (p^*, r\xi_r)$ and the 2 × 2 matrix M depends on m, k, the equilibrium fields *and* on the eigenvalue $-\omega^2$, a quantity that is not *a priori* known. Eqn. 1.15 is therefore solved in a trial-and-error fashion in a *shooting code*: 1.15 is integrated from the axis r = 0 to the edge $r = r_0$ for various values of ω^2 until one is found for which the solution obeys the correct boundary condition at the plasma-vacuum boundary. $-\omega^2$ is then an eigenvalue and the solution $(p^*, r\xi_r)$ is the corresponding eigenfunction. The other components of the solution, ξ_θ, ξ_z, ρ^1, T^1, $B_r{}^1$, $B_\theta{}^1$, and $B_z{}^1$, can then be obtained algebraically from p^* and $r\xi_r$. For internal modes the appropriate boundary condition is given by

$$\xi_r(r_0) = 0 \qquad (1.16)$$

while for m = 0 and m = 1 external modes the appropriate condition is given by (Bateman 1978):

$$p^* + [m^2 B_\theta{}^{0\,2} K_m(kr)/\mu_0 kr^3\ K_m'(kr)]\ r\xi_r = 0 \qquad (1.17)$$

at $r = r_0$. The derivation of eqn. 1.17, which essentially comes from the continuity of the total perturbed pressure across the perturbed boundary, will be

clarified in chapter three when a generalised version (appropriate to equilibria with skin currents) will be derived.

Typical eigenfunctions produced by the shooting code can be found in chapter three, figures 3.2 and 3.4. The basic features of the eigenfunctions are that:

(a) for m = 0 modes ξ_θ, B_r^1, and B_z^1 are zero, and ξ_z is $\pi/2$ out of phase with the other variables,

(b) for m = 1 modes ξ_θ, ξ_z and B_r^1 are $\pi/2$ out of phase with the other variables,

(c) as the wavelength of the perturbation decreases the growth rates increase and the eigenfunctions become more sharply peaked at the edge, and

(d) except for very long wavelength perturbations m = 0 modes have higher growth rates than the corresponding m = 1 modes.

Coppins (1988) reviewed the applicability of linear ideal MHD stability theory to the Z-pinch and found that it was more valid for this device than for any other (see also section 1.4 below). He showed that the enhanced stability of the gas-embedded Z-pinch (Dangor *et. al.* 1983), its inconsistently high axial temperature, and the complete absence of the m = 0 mode in this experiment could be explained by assuming that the pinch evolves into a Kadomtsev stable profile (figure 1.4) at an early stage in the discharge. He also attributed the anomalous stability of the Imperial College compressional pinch experiment (Haines *et. al.* 1988) to conducting wall stabilisation (an effect first analysed theoretically by Tayler 1957b) in the case of m = 1 modes, and to rapid cooling after peak current for m = 0 modes. Recent work however (Culverwell *et. al.* 1989, and also chapter six) suggests that this is not the case and that the absence of m = 0 instabilities in this experiment requires further investigation. The fibre experiments mentioned in the introduction last up to 100 ideal MHD growth times; it is with respect to this theory that these pinches are viewed as 'anomalously' stable. The investigation of this stability, and in particular whether it can be explained by resistive effects, forms the core of this thesis (chapters four and five).

1.4 Resistive MHD

It was stated in section 1.2 that ideal MHD is a legitimate model of Z-pinch dynamics provided that x, y, and y^2/x (defined by eqns. 1.1 and 1.2) were all much less than unity. The Bennett relation (Bennett 1934)

$$\mu_o I^2 = 16 \pi N k_B T_B \qquad (1.18)$$

(where I is the pinch current, N is the ion line density (number of ions per unit length) and T_B is the density-weighted mean temperature) expresses the $<\beta> = 1$ nature of the Z-pinch, the magnetic pressure on the left hand side balancing the thermal pressure on the right. Using this relation it is possible to show that x, y, and y^2/x depend on the macroscopic pinch parameters I, N, and radius r_o in the following way (for deuterium in SI units):

$$x = 2.56 \times 10^{41} \quad r_o \; I^4 \; N^{-3} \qquad (1.19)$$

$$y = 8.15 \times 10^{8} \quad N^{-1/2} \qquad (1.20)$$

$$y^2/x = 2.59 \times 10^{-24} \quad r_o^{-1} \; I^{-4} \; N^2 \qquad (1.21)$$

The curves defined by $x = y = y^2/x = 1$ can therefore be used to partition the $r_o I^4$ versus N plane as shown in figure 1.5 (Haines *et.al.* 1989). This figure shows the region of validity of ideal MHD and denotes the theories required in the other regions (for a review of these alternative theories see Culverwell 1988).

The region where resistivity is important is the most relevant to this thesis. This is because the small radius, high line density deuterium fibres remain resistive for a large part of the current rise time. Figure 1.5 shows typical positions on the $I^4 r_o$ - N plane of the NRL and LANL fibre experiments at peak current, demonstrating that they have only just reached the ideal phase at this time (NRL data (Sethian *et. al* 1987): $N = 5 \times 10^{20}$ m^{-1}, $I_{peak} = 500$ kA, $r_o = 200$ μm; LANL data (Hammel and Scudder 1987): $N = 6 \times 10^{19}$ m^{-1}, $I_{peak} = 230$ kA, $r_o = 100$ μm (est.)). This picture suggests that resistivity could have a significant effect on the dynamics of a fibre pinch before peak current, thus motivating the work of chapters two, four, and five.

The addition of resistivity modifies the ideal MHD equations 1.5 and 1.6 so that they read (Freidberg 1982 pp 809 - 811):

Ohm's law: $$\underline{E} + \underline{v} \wedge \underline{B} = \eta \underline{j} \qquad (1.22)$$

Energy equation: $$\rho^{\Gamma} \, d(p/\rho^{\Gamma})/dt = (\Gamma - 1)\{\eta j^2 - \nabla.\underline{q}\} \qquad (1.23)$$

The right-hand-side of 1.23 includes the heat flux term $\nabla.\underline{q}$ since in the

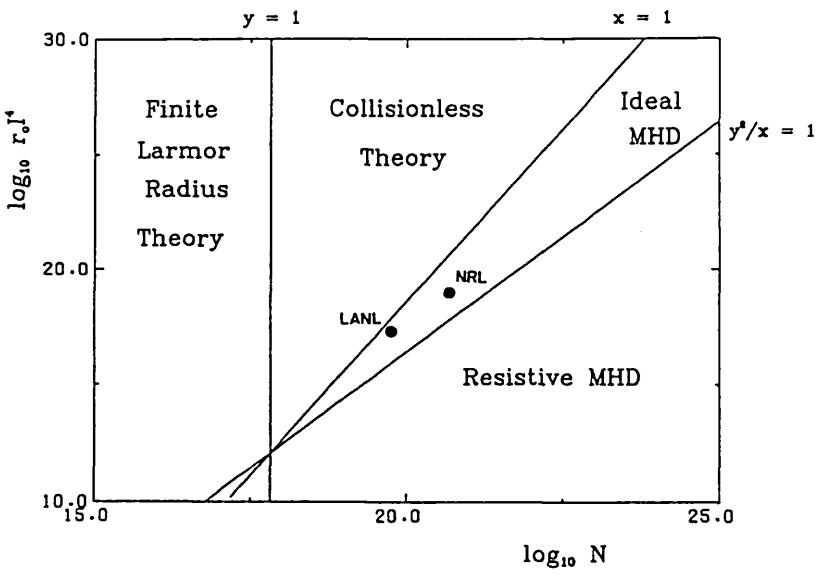


Figure 1.5 *Segregation of $I^4 r_o$ - N plane according to the criteria x, y, $y^2/x = 1$. 'NRL' = position of typical NRL fibre experiment, 'LANL' = position of typical LANL fibre experiment. SI units.*

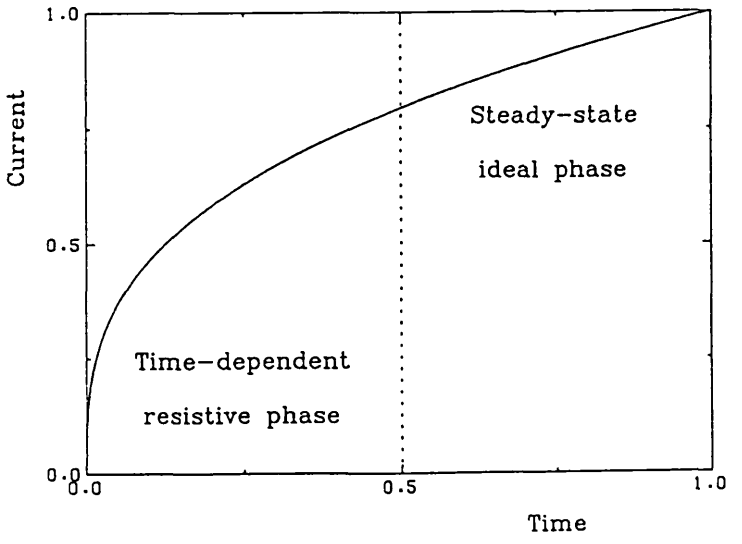


Figure 1.6 *Schematic 'Haines-Hammel' curve.*

collisionless regime (to be studied in chapter two) this term is of the same order of magnitude as the Ohmic heating term ηj^2, namely $O(y^2/x)$ if the magnitude of the left-hand-side is taken to be O(1). Similarly the RHS of eqn. 1.22 is $O(y^2/x)$ times larger than the individual terms of the LHS.

The resistivity η depends on the plasma temperature T which must be related to the other plasma variables through an equation of state. Throughout this thesis the plasma will be modelled as a fully ionised deuterium fluid (or hydrogen fluid, in chapter six) obeying the perfect gas equation of state

$$p = 2 n k_B T, \qquad (1.24)$$

the factor of 2 appearing because p is the total plasma pressure ($p = p_i + p_e$) whereas n is the single species number density. A constant γ log Λ of 10 will also be assumed. Coulomb logarithm

The inclusion of resistivity in Ohm's law (eqn. 1.22) breaks the topological constraint that magnetic fields are 'frozen into the flow' (Alfven 1950, Newcomb 1958) and allows plasma to diffuse across the lines of force. This might be expected to destabilise a pinch since it allows the plasma more degrees of freedom in its movement. Indeed early studies of Z-pinch stability involving incompressible plasmas (in which eqn. 1.23 is replaced with the condition $\nabla.\underline{v} = 0$) showed that this was the case (Tayler 1960). It is not clear however that the same is true in a compressible plasma since in this case resistive heating can dissipate energy that might otherwise drive an instability.

Resistive dissipation also has an important effect on the equilibrium, since in order to maintain pressure balance the resulting increase in thermal pressure must be balanced by an increasing confining force due to a rising current. The correct current profile (the 'Haines-Hammel' curve) was derived independently by Braginskii and Shafranov (1959), Haines (1960) and Hammel (1976) and is shown schematically in figure 1.6. It has two interesting limits. As t tends to infinity the current asymptotically approaches the Pease-Braginskii limiting current I_{PB} (of the order of 1 MA in deuterium) at which bremsstrahlung emission (a loss mechanism not included in eqn. 1.23) balances ohmic dissipation in a steady state Z-pinch (Pease 1957, Braginskii 1965). In the low current limit ($I << I_{PB}$) the current is proportional to $t^{1/3}$. This follows simply from the energy equation 1.23, which for static ($\underline{v} = \underline{0}$) equilibria reads:

$$\partial p/\partial t = (\Gamma - 1)\{\eta j^2 - \nabla.\underline{q}\} \qquad (1.25)$$

Multiplying this equation by $2\pi r$ and integrating with respect to r over the volume of the pinch, and assuming a uniform temperature (and therefore resistivity), gives

$$2Nk_B\, dT/dt = (\Gamma - 1)\, g\, \eta I^2/\pi r_o^2 \qquad (1.26)$$

where the shape factor $g = \langle j^2\rangle/\langle j\rangle^2 \simeq 1$ and the $\nabla.\underline{q}$ term has been transformed by Gauss' theorem into the surface integral $\oint \underline{q}.d\underline{S}$ which vanishes under the assumption that the equilibrium is thermally isolated. Application of the Spitzer resistivity formula $\eta \propto T^{-3/2}$ and the Bennett relation $I^2 \propto T$ to equation 1.26, followed by an integration in time, leads to

$$\eta(t) = \mu_o r_o^2/12(\Gamma-1)gt = \mu_o r_o^2/8gt \text{ if } \Gamma = 5/3 \qquad (1.27)$$

which in turn implies that

$$I(t) \propto T^{1/2} \propto \eta^{-1/3} \propto t^{1/3}. \qquad (1.28)$$

Relation 1.28 will be used in chapters two, three, four, and five.

The low resistivity condition $y^2/x << 1$ is more usually written in the form $S >> 1$, where the *Lundquist number* $S \simeq x/y^2$ is defined by:

$$S = \mu_o V_A r_o / \eta \qquad (1.29)$$

where
$$V_A^2 = \mu_o I^2/4\pi N m_i = 4k_B T/m_i \qquad (1.30)$$

Since $I \propto t^{1/3}$ the equilibrium can be seen to evolve on the *Ohmic heating timescale*

$$\tau_{ohm} = I / dI/dt = 3t = 3\mu_o r_o^2/8g\eta(t) \qquad (1.31)$$

Ideal MHD instabilities occur on the timescale (Tayler 1957a)

$$\tau_{mhd} = r_o / V_A \qquad (1.32)$$

Therefore, comparing eqns. 1.31 and 1.32 it can be seen that

$$\tau_{ohm} / \tau_{mhd} = 3\mu_o r_o V_A / 8g\eta = (3/8g)\, S \qquad (1.33)$$

Thus when resistivity is important ($S << 1$) it is essential to include the time-dependence of the equilibrium since it is then changing on a timescale very much smaller than the ideal MHD instability growth time. Conversely, if $S >> 1$ then the equilibrium is changing very slowly and ideal MHD is the correct model to use in a stability analysis. This conclusion is fundamental to the rest of this thesis: it motivates the search for the equilibria described in chapter two, justifies the use of ideal MHD to study the high current stability of those equilibria in chapter three, and explains the necessity of the initial-value approach to the study of resistive stability in chapters four and five.

1.5 Summary and outline of thesis

In this chapter the elements of ideal MHD and resistive MHD that are of relevance to the rest of this thesis have been briefly reviewed. Worth particular note are: the three conditions for the applicability of ideal MHD (high collisionality, small ion Larmor radius, and low resistivity); the orthogonality of ideal MHD eigenfunctions belonging to different eigenvalues and the reality of those eigenvalues due to the self-adjoint nature of the ideal MHD force operator; the region of the $r_o I^4 - N$ plane where ideal MHD is valid; and the segregation of the Haines-Hammel curve into an early, time-dependent, resistive part and a later, steady state, ideal part.

The plan of the rest of the thesis is as follows. Chapter two discusses two new classes of time-dependent Z-pinch equilibria which respect pressure balance exactly. Chapter three studies the high current ideal MHD stability of these equilibria. Chapter four studies the stability of axisymmetric perturbations in the low current resistive regime, and chapter five generalises this work to the study of $m = 1$ modes. Chapter six concerns the inverse skin effect (Haines 1959) and its occurrence in the Imperial College compressional pinch, enabling a quantitative estimate of the stability of that pinch to be made. Finally in chapter seven the principal conclusions of the thesis are collated and suggestions for possible future work are made.

CHAPTER TWO

TIME-DEPENDENT Z-PINCH EQUILIBRIA

2.1 Separable solutions

In this chapter solutions of the time-dependent equilibrium Z-pinch equations are discussed. From the totality of all possible solutions only those respecting exact pressure balance will be considered here i.e. those in which

$$\underline{j} \wedge \underline{B} - \nabla p = \rho \, d\underline{v}/dt = \underline{0}. \qquad (2.1)$$

This is a legitimate assumption in the modelling of pinches formed from frozen deuterium fibres since these pinches expand at less than one-tenth of the ion thermal speed (Sethian *et. al.* 1987). Quasi-equilibria in which $\underline{j} \wedge \underline{B} - \nabla p = \underline{0}$ while $\rho d\underline{v}/dt$ is finite have been studied by Glasser (1989) and Rosenau *et. al.* (1989), but because of the simplicity of the exact pressure balance equilibria, particularly with regard to the stability analyses of chapters three, four, and five, attention here will be restricted to exact equilibria only.

The time-dependent Z-pinch equations (1.3, 1.4, 1.7, 1.8, 1.22, 1.23, 1.24) form a set of non-linear coupled partial differential equations for the plasma variables. By making the following assumptions this problem can be reduced to the solution of a set of coupled *ordinary* differential equations for the plasma variables with respect to the radial coordinate 'r'. This simplification requires the assumptions of cylindrical symmetry, collisionless (large $\omega_{ci}\tau_{ii}$) transverse ion thermal conductivity

$$\kappa_{\perp}^{(i)} = 2nk_B T/m_i \omega_{ci}^2 \tau_{ii} = g_o \, n^2/B^2 T^{1/2} \qquad (2.2)$$

where $g_o = 2.26 \times 10^{-40} \log\Lambda \quad Jm^5 T^2 (eV)^{-1/2} s^{-1}$, transverse Spitzer resistivity

$$\eta_{\perp} = m_e/ne^2\tau_{ei} = g_1 \, T^{-3/2} \qquad (2.3)$$

where $g_1 = 1.03 \times 10^{-4} \log\Lambda \quad \Omega m (eV)^{3/2}$, and a constant $\log\Lambda$. Throughout this chapter the plasma will be modelled as a single-temperature, fully ionised

deuterium fluid. In addition to these assumptions bremmstrahlung radiation is neglected: thus any solutions found by this analysis will only be strictly valid for currents much less than the Pease-Braginskii limiting current of about 1 MA. However, the work of Rosenau *et. al.* suggests that this is over-cautious and that the solutions found in this chapter are hardly changed by the inclusion of radiation effects in the basic model. These authors also claim that the plasma variables develop 'self-similar' profiles very much like the ones described below even if the *collisional* thermal conductivity is employed, which indicates that the constraint that the plasma is collisionless might be over-severe.

By separating out a power of time from the equilibrium variables, the equations reduce to ordinary differential equations in 'r'. It is only by neglecting bremsstrahlung and using the collisionless thermal conductivity that this can be done. There are only two ways of performing this separation while maintaining pressure balance: by assuming that the equilibrium is stationary ($v_r = 0$), or by assuming that it expands with a velocity $v_r = r/t$. The equilibrium profiles of each class are described in sections 2.2 and 2.3. Section 2.4 concludes with a discussion of the main results and conclusions of the chapter.

2.2 Stationary equilibria: v = 0

By factorising the plasma variables 'f' according to the rule

$$f(r, t) = \hat{f}(r)\, t^{\alpha} \qquad (2.4)$$

with a different value of α for each variable f, the following *separable solutions* are found to satisfy the time-dependent parts of the general Z-pinch equations:

$$v(r, t) = 0 \qquad (2.5)$$

$$j_z(r, t) = \hat{j}(r)\, t^{1/3} \qquad (2.6)$$

$$B_\theta(r, t) = \hat{B}(r)\, t^{1/3} \qquad (2.7)$$

$$E_z(r, t) = \hat{E}(r)\, t^{-2/3} \qquad (2.8)$$

$$p(r, t) = \hat{p}(r)\, t^{2/3} \qquad (2.9)$$

$$n(r, t) = \hat{n}(r) \tag{2.10}$$

$$T(r, t) = \hat{T}(r)\, t^{2/3} \tag{2.11}$$

$$\eta(r, t) = \hat{\eta}(r)\, t^{-1}. \tag{2.12}$$

The constancy of 'n' follows from the continuity equation with zero velocity, while the current density relation (2.6) implies that the pinch current I is proportional to $t^{1/3}$, in agreement with the early part ($I << I_{PB}$) of the Haines−Hammel curve (equation 1.28 and figure 1.6 in chapter one). These solutions are therefore stationary equilibria in which the increasing plasma pressure is balanced by an increasing confining force due to a rising current.

By introducing the normalised variables:

$$x = r / r_* \tag{2.13}$$

$$y_1 = \hat{p}(r) / \hat{p}(0) \tag{2.14}$$

$$y_2 = \hat{j}(r) / \hat{j}(0) \tag{2.15}$$

$$y_3 = \hat{\eta}(r) / \hat{\eta}(0) \tag{2.16}$$

$$y_4 = \hat{B}(r) / \mu_o\, \hat{j}(0)\, r_* \tag{2.17}$$

$$y_5 = r\, d\hat{\eta}/dr \,/\, \hat{\eta}(0) \tag{2.18}$$

where $$r_*^2 = \hat{\eta}(0) / \mu_o, \tag{2.19}$$

the equations 1.4, 1.7, 1.8, 1.22, 1.23, and 1.24, together with the substitutions 2.2 and 2.3 reduce to the following first order ordinary differential equations:

pressure balance $$dy_1 / dx = - y_2\, y_4 / \Omega \tag{2.20}$$

Faraday - Ohm's law $$dy_2 / dx = (xy_4 - 3y_2y_5) / 3xy_3 \tag{2.21}$$

definition of y_5 $$dy_3 / dx = y_5 / x \tag{2.22}$$

Ampere's law $$dy_4 / dx = (xy_2 - y_4) / x \tag{2.23}$$

energy equation $\quad dy_5 / dx = xy_4^2(y_3y_2^2 - \Omega y_1)/\Psi\Omega^2 y_1^2$

$$+ \; 2y_5(xy_2(\Omega y_1 + y_4^2) - \Omega y_1 y_4)/\Omega x y_1 y_4 \qquad (2.24)$$

where $\quad \Psi = (m_i/18m_e)^{1/2} \simeq 14.28$ for deuterium $\qquad (2.25)$

and $\quad \Omega = \hat{p}(0)/\hat{\eta}(0)\hat{j}^2(0).$ $\qquad (2.26)$

The number Ψ is essentially the ratio of g_0 to g_1 in eqns. 2.2 and 2.3 above, and can therefore be regarded as a normalised measure of the magnitude of the thermal conductivity compared to that of the resistivity. The initial conditions obeyed by the variables $\{y_i,\ i = 1,5\}$ follow from the normalisations 2.13 to 2.18:

$$y_1 = y_2 = y_3 = 1; \quad y_4 = y_5 = 0 \qquad \text{at } x = 0. \qquad (2.27)$$

It can be seen that Ω is the only free parameter in these normalised equations and boundary conditions, and so there is a *family* of solutions to these equations, each member of the family being characterised by a particular value of Ω. The set of normalised non-linear coupled ODEs 2.20 to 2.24 is the ultimate reduced version of the original problem; the next three subsections are concerned with its analysis in three different regimes.

2.2.(i) Zero thermal conductivity

At low temperatures plasma is collisional ($\omega_{ce}\tau_{ei} << 1$) and the parallel electron thermal conductivity $\kappa_{||}^{(e)} \propto T^{5/2}$ should be used. Unfortunately this formula does not scale in the appropriate way to allow a separable solution of the type discussed above (although see the remark in section 2.1 concerning the work of Rosenau *et. al.*). In the collisional regime the only way exactly separable solutions can be found is by *neglecting* thermal conduction altogether i.e. by taking the artificial limit $\Psi = 0$ in eqns. 2.20 to 2.24. In this case eqn. 2.24 becomes

$$\Omega\, y_1 = y_2^2\, y_3, \qquad (2.28)$$

which, when considered with the initial condtions 2.27 shows that for zero thermal conductivity, $\Omega = 1$ i.e. there is only one possible separable solution in the zero

thermal conductivity limit.

Equations 2.20 to 2.24 (with the conditions $\Omega = 1$ and $\Psi = 0$) can be numerically integrated out from the axis by a fourth order Runge-Kutta integration scheme (e.g Gear 1971). Profiles of current density, magnetic induction, pressure, axial electric field, number density, and temperature up to a radius $r_o = 10r_*$ are shown in figure 2.1. Since the number density never decreases (to be proved later) there is no natural way to define the 'edge' of the pinch - the profiles have to be truncated at some arbitrary radius. As can be seen from the figure, the pressure, current density and temperature profiles are peaked on axis, while the density increases monotonically. There is some experimental evidence of an edge-peaked density profile occuring during the pre-ionising phase of the gas-embedded Z-pinch (Favre-Dominguez, 1985) in which the mean value of $\omega_{ci}\tau_{ii}$ is of the order of 0.1. In view of the qualitative similarity of these profiles to those of figure 1.4 it is not surprising to find that this zero thermal conductivity equilibrium is stable to $m = 0$ perturbations according to the Kadomtsev criterion.

Equations 2.20 to 2.23 and 2.28 admit some interesting scaling relations. Inserting 2.28 into 2.20 shows that

$$y_2\, y_3' + 2\, y_2'\, y_3 = -\, y_4 \qquad (2.29)$$

while eqn. 2.21 shows that

$$3\, y_2\, y_3' + 3\, y_2'\, y_3 = y_4. \qquad (2.30)$$

Adding 2.29 to 2.30 and then dividing by $y_2 y_3$ leads to the result

$$4\, y_3' / y_3 + 5\, y_2' / y_2 = 0 \qquad (2.31)$$

so that

$$y_2 \propto y_3^{\,-4/5}. \qquad (2.32)$$

Substitution of this result back into the original equations then produces the following set of scaling relations:

$$\hat{j} \propto \hat{n}^{-12},\ \hat{E} \propto \hat{n}^{3},\ \hat{p} \propto \hat{n}^{-9},\ \hat{T} \propto \hat{n}^{-10},\ \text{and}\ \hat{B} \propto \hat{n}^{2}\, d\hat{n}/dr. \qquad (2.33)$$

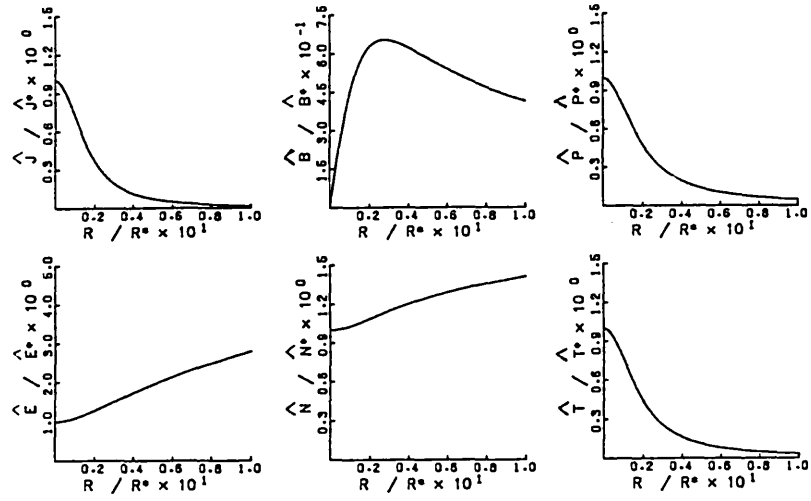


Figure 2.1 *Zero thermal conductivity stationary equilibrium.* $\hat{j}$, $\hat{p}$, $\hat{E}$, $\hat{n}$, *and* $\hat{T}$ *normalised w.r.t. values on axis,* $\hat{B}$ *normalised w.r.t.* $\mu_o \hat{j}(0) r_*$.

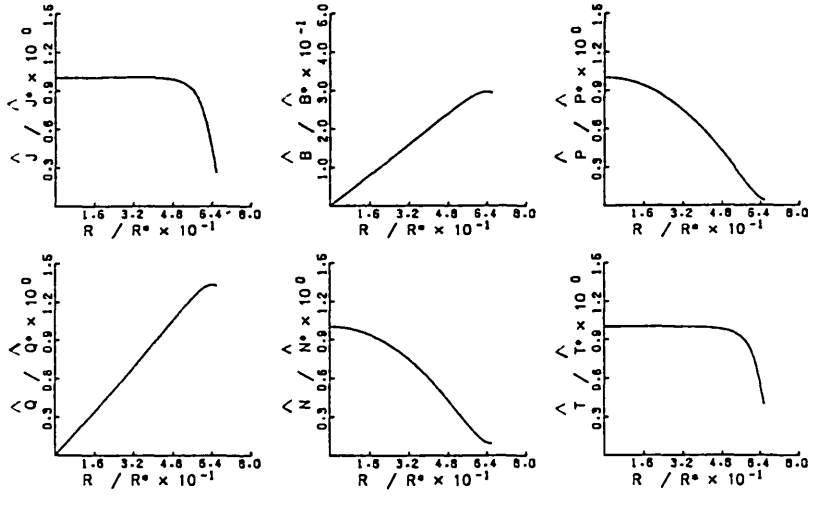


Figure 2.2 *Finite thermal conductivity stationary equilibrium.* $\Omega = 0.1$. $\hat{q}$ *normalised with respect to* $(3\Psi/2)\Omega\hat{p}(0)r_*$, *other variables normalised as in figure 2.1.*

These strong dependences on the number density 'n' suggest why this quantity is so nearly uniform: a more rapidly varying density profile could lead to unphysically high gradients in the other variables. The scalings also show that the number density never vanishes, for the following reason. The current density must be positive everywhere since it is positive on axis, assumed to be continuous and cannot vanish anywhere since this would imply (eqn. 2.33) an infinite number density, a possibility that can be rejected on physical grounds. Thus, the total current flowing in a cylinder of radius 'r' is positive, and therefore so is $B(r) = \mu_0 I(r)/2\pi r$. Faraday's law, $\partial E_z/\partial r = \partial B_\theta/\partial t = B/3t$ as $B \propto t^{1/3}$, then implies that $\partial E_z/\partial r > 0$, so that E_z is an everywhere positive, monotonically increasing function of r. But by eqn. 2.33 $n \propto E^{1/3}$ which implies that the same is true for n, and so the number density never vanishes.

2.2.(ii) Finite thermal conductivity

High temperature pinches are collisionless and in this regime the thermal conductivity coefficient obeys the correct scaling law (eqn. 2.2) to allow a separable solution. In this section we therefore study the system of equations 2.20 to 2.24 in which Ψ assumes its true value of 14.28 (for deuterium). As said before, there is a one−parameter (namely, Ω) family of solutions to these equations. Empirically the equilibria are found to be radically different if Ω is less than, equal to, or greater than the *critical value* $\Omega_{crit} \simeq 3.43$.

If Ω is less than Ω_{crit} the profiles are like those in figure 2.2, which shows the $\Omega = 0.1$ solutions. The current density and temperature are centre−peaked whereas the number density falls from its peak axial value to a minimum value, after which it begins to increase (not shown). Defining the *edge* of the pinch $r = r_0$ as the position of this minimum number density and truncating the solutions there, it is found that the radial heat flow at the plasma edge $q_r(r_0)$ is positive i.e. *outwards*. These solutions may therefore be described as 'gas−embedded' equilibria (Coppins *et. al.* 1988) since they share the basic features (finite edge density, thermal conduction into the surrounding gas) of gas−embedded pinches.

As Ω increases (figure 2.3 shows the $\Omega = 1$ profiles) the plasma edge density and heat flux decrease until at $\Omega = \Omega_{crit}$ they both vanish and the profiles become *thermally isolated*. Figure 2.4 shows the Ω_{crit} profiles. Note that the temperature and current density are now slightly peaked at the edge.

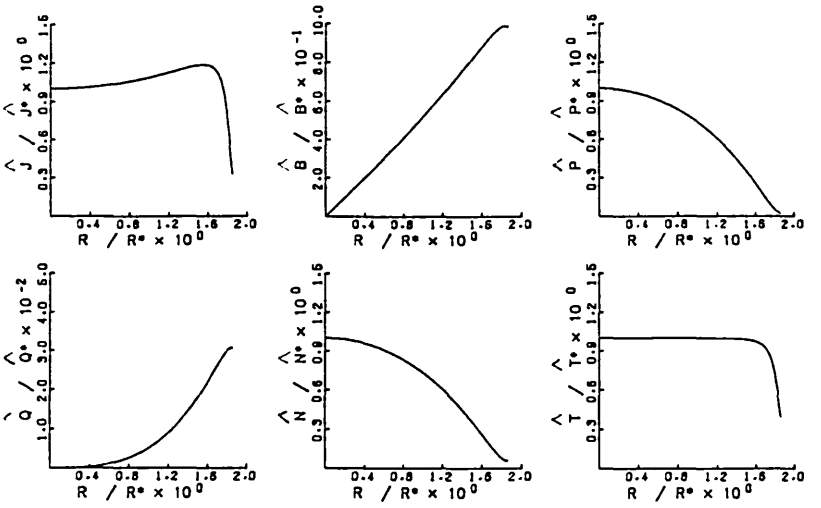


Figure 2.3 Finite thermal conductivity stationary equilibrium.
Ω = 1.0 Normalisation as in figure 2.2.

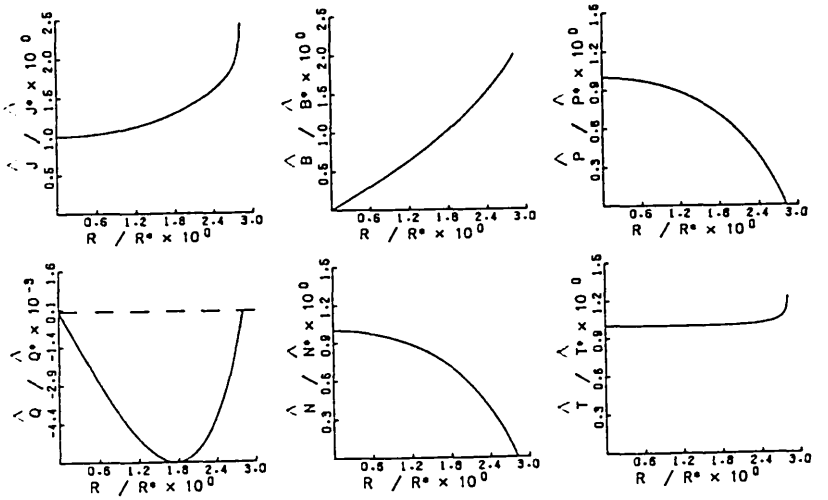


Figure 2.4 Finite thermal conductivity stationary equilibrium.
$\Omega = \Omega_{crit}$ = 3.43. Normalisation as in figure 2.2.

For Ω greater than Ω_{crit} the density still vanishes at the edge, the pressure approaches a finite value, the surface current density and temperature diverge, and the heat flux at the edge $q_r(r_o)$ becomes large and *inward*. These are all features of equilibria confined by a *skin current* at the plasma surface. Since the heat is being *generated* at the plasma edge and is not flowing *across* it from the vacuum these solutions may still be considered to be thermally isolated. These features become more enhanced as Ω increases: figure 2.5 shows the $\Omega = 10$ profiles, figure 2.6 shows those for $\Omega = 100$.

The plasma radius r_o is a monotonically increasing function of Ω (figure 2.7); asymptotically as $\Omega \to \infty$

$$r_o / r_* \quad \propto \quad \log \Omega. \qquad (2.34)$$

The fraction of the total current carried in the skin, determined by the thermal pressure imbalance at the plasma edge (see the discussion in section 3.4 of chapter three), is also found to be an increasing function of Ω for $\Omega > \Omega_{crit}$ (figure 2.8); again as $\Omega \to \infty$ the limiting behaviour is found numerically to be given by

$$I\ (skin)\ /\ I\ (inside) \quad \propto \quad \log \Omega. \qquad (2.35)$$

2.2.(iii) Infinite thermal conductivity

In view of the largely uniform temperature profiles shown in figures 2.2 to 2.6 it is interesting to study the infinite thermal conductivity solutions of eqns. 2.20 to 2.24. This limit has been studied before by Braginskii and Shafranov (1959) and by Haines (1960).

The infinite thermal conductivity regime is formally given by the $\Psi \to \infty$ limit of eqn. 2.24, in which case this equation and equation 2.22 are replaced by the uniform temperature conditions

$$y_5 \equiv 0 \quad \text{and} \quad y_3 \equiv 1. \qquad (2.36)$$

In this case eqn. 2.21 reduces to

$$3 \times dy_2/dx = xy_4 \qquad (2.37)$$

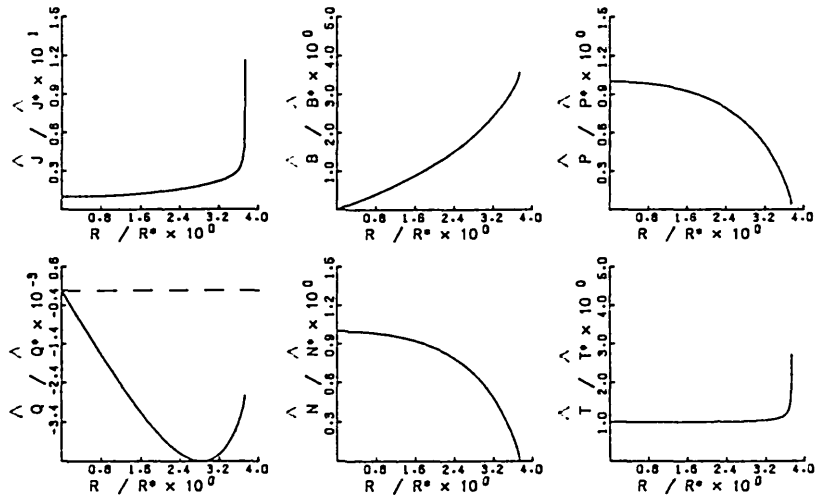


Figure 2.5 Finite thermal conductivity stationary equilibrium.
Ω = 10.0 Normalisation as in figure 2.2.

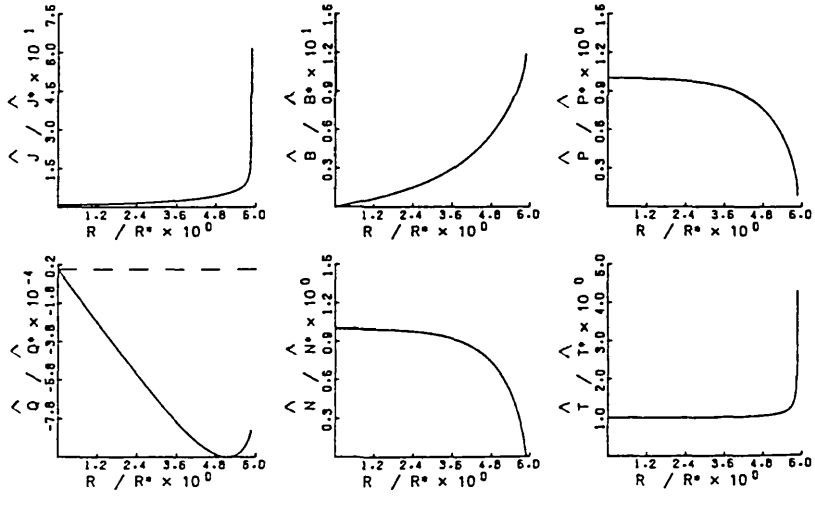


Figure 2.6 Finite thermal conductivity stationary equilibrium.
Ω = 100.0 Normalisation as in figure 2.2.

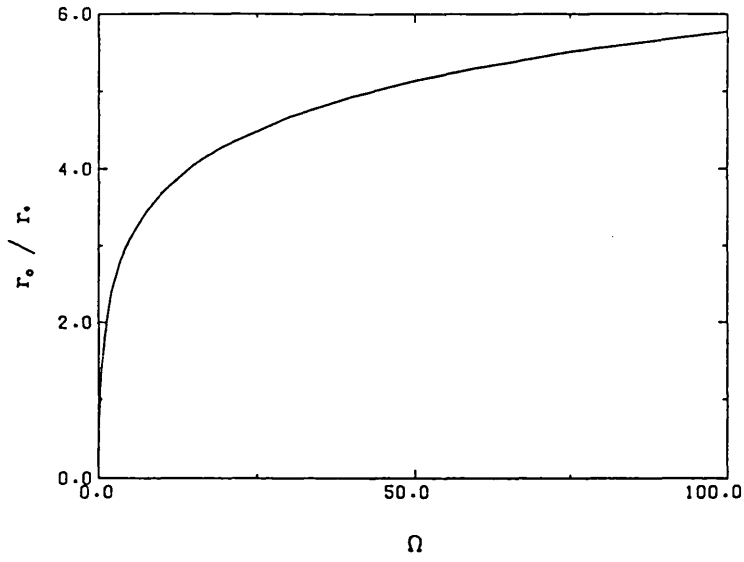


Figure 2.7 Stationary finite thermal conductivity equilibria: normalised pinch radius r_o/r_* as a function of Ω.

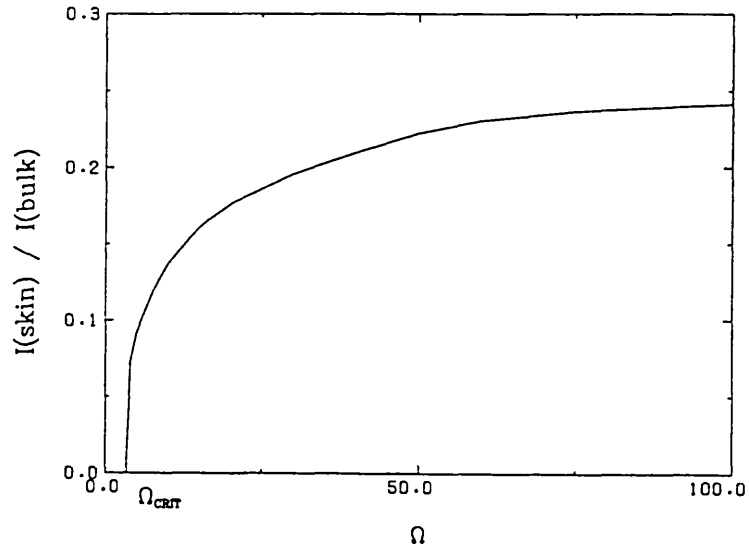


Figure 2.8 Stationary finite thermal conductivity equilibria: ratio of current flowing in skin to current carried inside pinch as a function of Ω.

which, when combined with eqn. 2.23 gives

$$3\ d(x\ dy_2/dx)\ /dx\ =\ d(x\ y_4)\ /\ dx\ =\ xy_2. \qquad (2.38)$$

The solution of this equation, subject to the boundary conditions

$$y_2(0)\ =\ 1; \qquad y_2'(0)\ =\ y_4(0)/3y_3(0)\ =\ 0 \qquad (2.39)$$

is

$$y_2(x)\ =\ I_0(x/\sqrt{3}) \qquad (2.40)$$

where I_0 is a modified Bessel function of the first kind. Substitution of 2.40 and 2.36 into 2.20 to 2.23 gives

$$y_4(x)\ =\ \sqrt{3}\ I_1(x/\sqrt{3}) \qquad (2.41)$$

and

$$y_1(x)\ =\ 1\ +\ (3/2\Omega)[1\ -\ I_0^2(x/\sqrt{3})]. \qquad (2.42)$$

This Bessel function density profile has a zero for all values of Ω, although since infinite thermal conductivity was assumed it does not follow that the radial heat flow automatically vanishes at the plasma edge. Indeed it can be shown by integrating the energy equation 1.23 over the plasma volume, and using Gauss' law to transform the volume integral of $\nabla.\underline{q}$ into the integral of $\underline{q}$ over the surface of the pinch, that $q_r(r_0)$ only vanishes when $\Omega = \Omega_{crit} \simeq 3.429$, the *same* critical value as in the finite thermal conductivity case of section 2.2.(ii). Figure 2.9 shows the infinite thermal conductivity $\Omega = \Omega_{crit}$ profiles. The radial heat flow at the edge is outward (inward) if Ω is less than (greater than) Ω_{crit}, and in the absence of finite plasma densities or skin currents at the pinch edge these $\Omega \neq \Omega_{crit}$ solutions must be rejected on physical grounds.

It is worth noting here that for the current density profile of equation 2.40 the shape factor $g = \langle j^2\rangle/\langle j\rangle^2$ of section 1.4 (chapter one) has the value 1.028, indicating that this current profile is only very weakly concentrated at the plasma edge (Haines 1960).

A discussion of the physical basis of the results of this section is postponed until section 2.4.

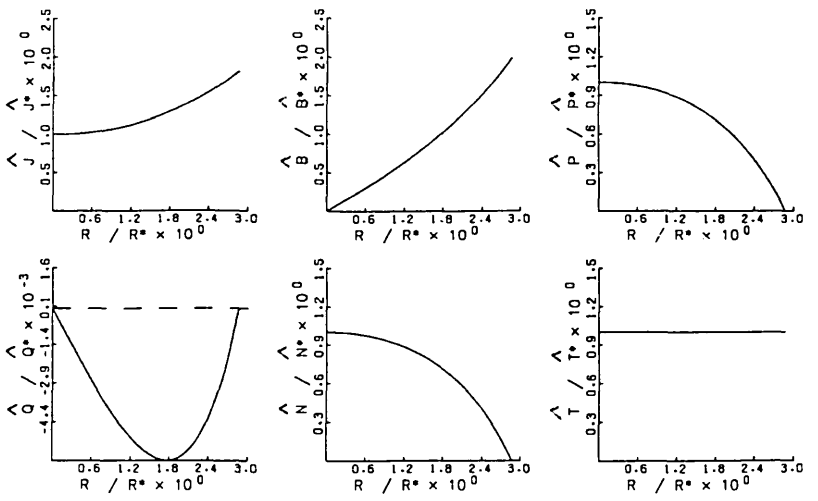


Figure 2.9 Infinite thermal conductivity stationary equilibrium. $\Omega = \Omega_{crit} = 3.43$. *Normalisation as in figure 2.1.*

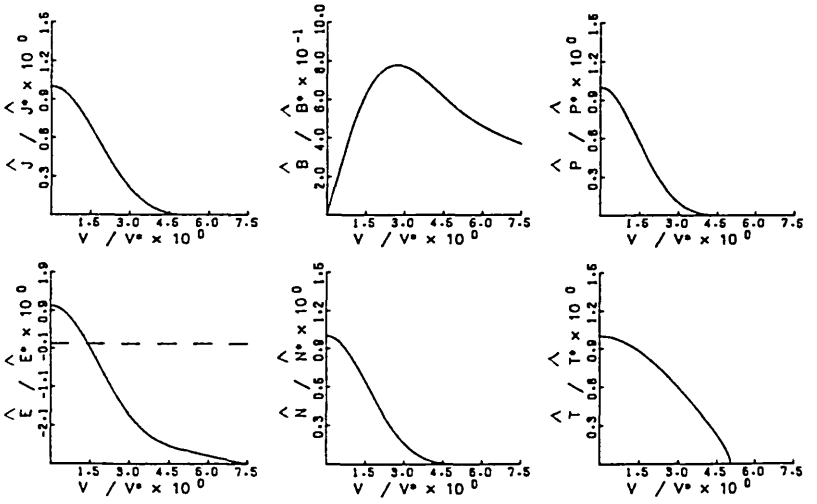


Figure 2.10 Zero thermal conductivity non-stationary equilibrium. $\hat{J}$, $\hat{p}$, $\hat{E}$, $\hat{n}$, *and* $\hat{T}$ *normalised w.r.t. values on axis,* $\hat{B}$ *normalised w.r.t.* $\mu_o \hat{J}(0) v_*$.

2.3 Non−stationary equilibria: v = r/t

Straightforward substitution shows that $\underline{v} = (r/t, 0, 0)$ is a solution of $d\underline{v}/dt = \partial\underline{v}/\partial t + \underline{v}.\nabla\underline{v} = \underline{0}$. Pinch configurations having this velocity field may therefore be described as non−stationary equilibria: this section studies such equilibria in some detail.

By factorising the plasma variables f according to the rule

$$f(r, t) = \hat{f}(r/t)\ t^{\alpha} \qquad (2.43)$$

with a different value of α for each variable f the following *separable solutions* to the basic plasma equations 1.3, 1.4, 1.7, 1.8, 1.22, 1.23, and 1.24 may be found:

$$v = r / t \qquad (2.44)$$

$$j_z(r, t) = \hat{j}(v)\ t^{-7/3} \qquad (2.45)$$

$$B_\theta(r, t) = \hat{B}(v)\ t^{-4/3} \qquad (2.46)$$

$$p(r, t) = \hat{p}(v)\ t^{-8/3} \qquad (2.47)$$

$$n(r, t) = \hat{n}(v)\ t^{-2} \qquad (2.48)$$

$$T(r, t) = \hat{T}(v)\ t^{-2/3} \qquad (2.49)$$

$$\eta(r, t) = \hat{\eta}(v)\ t^{1} \qquad (2.50)$$

and

$$E_z(r, t) = \hat{E}(v)\ t^{-4/3}. \qquad (2.51)$$

Equation 2.45 shows that the total pinch current $I(t) \propto t^{-1/3}$. This is because the pinch edge, if it has one, is defined by a certain value of r/t, say v_o. Since these equilibria are *exact* ($d\underline{v}/dt = \underline{0}$), the edge *maintains* this velocity at all times and thus at time 't' the pinch radius 'r_o' is given by $r_o = v_o t$. Therefore,

$$I(t) = \int_0^{V_o t} j_z(r, t)\ 2\pi r\ dr$$

$$\propto t^{-7/3} \cdot t^2 \cdot \int_0^{V_o} \hat{j}(v)\ v\ dv$$

i.e. $$I(t) = t^{-1/3} \times \text{some function of } v_o. \qquad (2.52)$$

These equilibria are therefore expanding while being held in pressure balance by a falling current.

Analogously to the work of section 2.2 the substitutions:

$$x = v / v_* \qquad (2.53)$$

$$y_1 = \hat{p}(v) / \hat{p}(0) \qquad (2.54)$$

$$y_2 = \hat{j}(v) / \hat{j}(0) \qquad (2.55)$$

$$y_3 = \hat{\eta}(v) / \hat{\eta}(0) \qquad (2.56)$$

$$y_4 = \hat{B}(v) / \mu_o \hat{j}(0) v_* \qquad (2.57)$$

$$y_5 = v \, d\hat{\eta}/dv / \hat{\eta}(0) \qquad (2.58)$$

where $$v_*^2 = \hat{\eta}(0) / \mu_o \qquad (2.59)$$

lead to the following system of ODEs for the quantities $\{y_i, i = 1,5\}$:

pressure balance $$dy_1 / dx = - y_2 y_4 / \Omega \qquad (2.60)$$

Faraday - Ohm's law $$dy_2 / dx = - (xy_4 + 3y_2y_5) / 3xy_3 \qquad (2.61)$$

definition of y_5 $$dy_3 / dx = y_5 / x \qquad (2.62)$$

Ampere's law $$dy_4 / dx = (xy_2 - y_4) / x \qquad (2.63)$$

energy equation $$dy_5 / dx = xy_4^2(y_3y_2^2 - \Omega y_1)/\Psi\Omega^2 y_1^2$$

$$+ 2y_5(xy_2(\Omega y_1 + y_4^2) - \Omega y_1 y_4)/\Omega x y_1 y_4 \qquad (2.64)$$

where again $$\Psi = (m_i/18m_e)^{1/2} \simeq 14.28 \text{ for deuterium} \qquad (2.65)$$

and $$\Omega = \hat{p}(0)/\hat{\eta}(0)\hat{j}^2(0). \qquad (2.66)$$

These equations are subject to boundary conditions 2.27.

[Remarkably, apart from a change in sign of one of terms of eqn. 2.61 equations 2.60 to 2.66 are formally identical to eqns. 2.20 to 2.26.]

The set of equations 2.60 to 2.64 is now studied in three different regimes.

2.3.(i) Zero thermal conductivity

The solutions in this limit are defined $\Omega = 1$ and $\Psi = 0$. The profiles of current density, magnetic induction, pressure, electric field, number density and temperature are shown in figure 2.10. Note that since these solutions are plotted against $(r/t)/v_*$ the radial scale length of these profiles increases linearly with time. The magnitudes also vary in time according to eqns. 2.45 to 2.51.

The solutions are found numerically to have an edge (i.e. a vanishing number density) at $v_o/v_* \simeq 5.06$.

The following scaling laws can be derived in exactly the same way as for the zero thermal conductivity stationary equilibria of section 2.2.(i):

$$\hat{j} \propto \hat{n}^{6/7}, \quad \hat{p} \propto \hat{n}^{9/7}, \quad \hat{T} \propto \hat{n}^{2/7}, \quad \hat{B} \propto d(\hat{n}^{3/7})/dv,$$

$$\hat{E} \propto - v^{2/3}\, d(v^{1/3}\, \hat{n}^{3/7})/dv. \qquad (2.67)$$

2.3.(ii) Finite thermal conductivity

The one−parameter family of solutions to eqns. 2.60 to 2.64, in which Ψ takes its correct value of 14.28 for deuterium, is found to depend on whether Ω is less than, equal to, or greater than a critical value $\Omega_{crit} \simeq 1.25$.

If Ω is less than Ω_{crit} then the pinch density never vanishes and the plasma edge heat flow $q_r(v_o)$ is outwards (figure 2.11 shows the $\Omega = 0.1$ profiles); these solutions may be described as 'gas−embedded'.

As Ω increases the plasma edge density and heat flow both decrease until

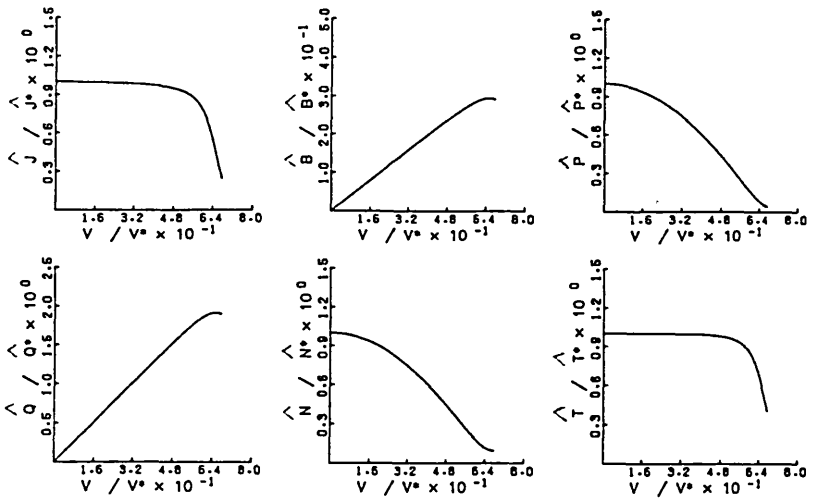


Figure 2.11 Finite thermal conductivity non-stationary equilibrium. $\Omega = 0.1$. $\hat{q}$ normalised with respect to $(3\Psi/2)\Omega\hat{p}(0)v_*$, other variables normalised as in figure 2.10.

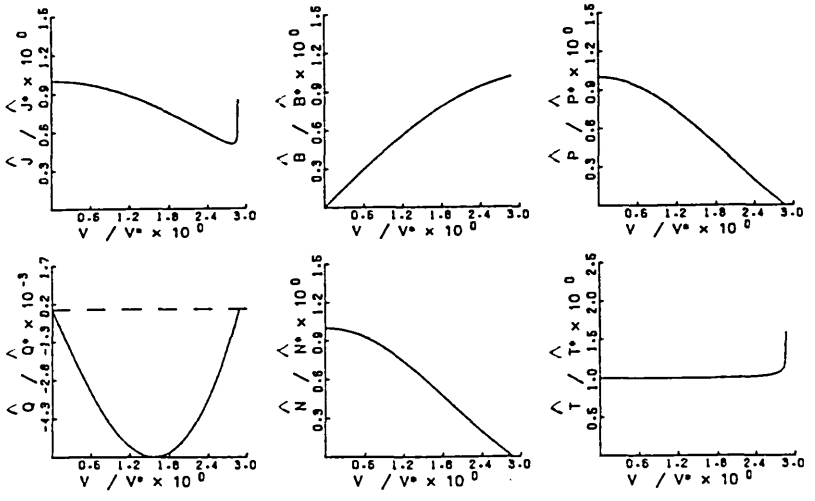


Figure 2.12 Finite thermal conductivity non-stationary equilibrium. $\Omega = \Omega_{crit} = 1.25$. Normalisation as in figure 2.11.

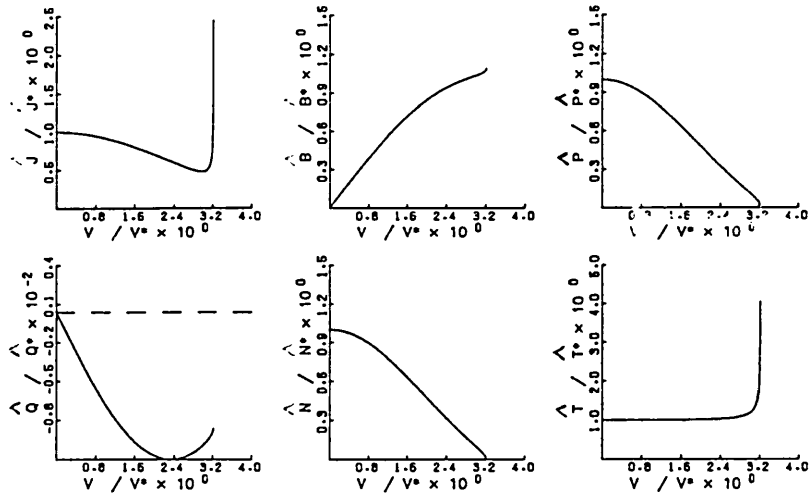


Figure 2.13 Finite thermal conductivity non-stationary equilibrium.
Ω = 1.5. Normalisation as in figure 2.11.

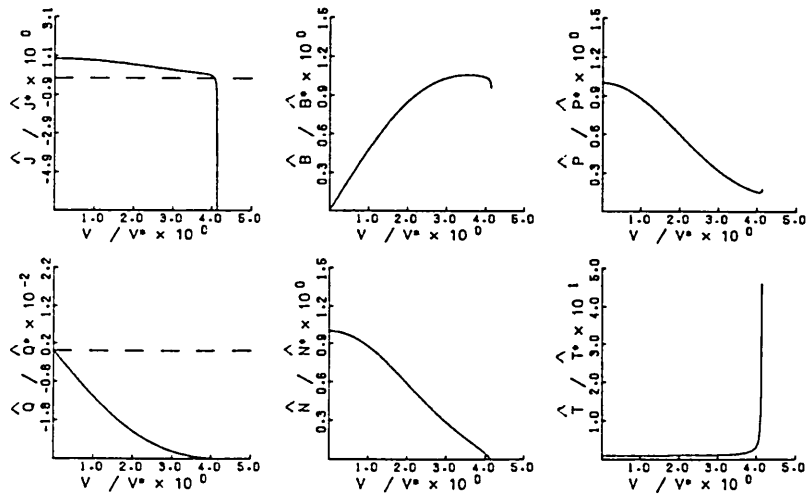


Figure 2.14 Finite thermal conductivity non-stationary equilibrium.
Ω = 1.95. Normalisation as in figure 2.11.

they vanish at Ω_{crit} at which point the equilibria become thermally isolated (figure 2.12).

If $\Omega_{crit} < \Omega < \Omega_{max} \simeq 1.96$ the equilibria are confined by skin currents at the plasma edge supplying heat into the plasma. Figure 2.13 shows the $\Omega = 1.5$ profiles. Just before Ω reaches Ω_{max} the skin current *reverses* (figure 2.14).

If Ω is greater than Ω_{max} the plasma edge density is finite once more and the solutions must be rejected on physical grounds as they require heat flow *into* the pinch from the outside, and do not therefore constitute acceptable gas—embedded equilibria.

Figure 2.15 shows that v_o/v_* is a monotonically increasing function of Ω. Figure 2.16 shows how the amount of current flowing in the skin varies with Ω when $\Omega_{crit} < \Omega < \Omega_{max}$. The maximum positive skin current occurs at $\Omega \simeq 1.7$ at which approximately 17% of the total current is flowing in the skin. The reversal of the skin current close to Ω_{max} is clearly shown.

2.3.(iii) Infinite thermal conductivity

As in section 2.2.(iii) the non—stationary separable solutions can be solved analytically in the $\Psi \to \infty$ limit. In a similar way to the analysis of that section the following solutions are found:

$$y_2(x) = J_0(x/\sqrt{3}) \qquad (2.68)$$

$$y_4(x) = \sqrt{3}\, J_1(x/\sqrt{3}) \qquad (2.69)$$

and

$$y_1(x) = 1 - (3/2\Omega)[1 - J_0^2(x/\sqrt{3})], \qquad (2.70)$$

where J_0 and J_1 are (unmodified) Bessel functions of the first kind. If $0 < \Omega < 3/2$ equation 2.70 has a zero (i.e. the plasma density vanishes) for some value of x between zero (for $\Omega = 0$) and $\sqrt{3} \times 2.4048 \simeq 4.165$ (for $\Omega = 3/2$). However the plasma edge heat flux $q_r(v_o)$ vanishes only when Ω equals a critical value, the *same critical value* ($\Omega_{crit} \simeq 1.25$) as for the finite thermal conductivity solutions. The Ω_{crit} profiles are shown in figure 2.17. All other solutions with Ω in this range must be rejected on the same physical criteria that were applied in section 2.2.(iii).

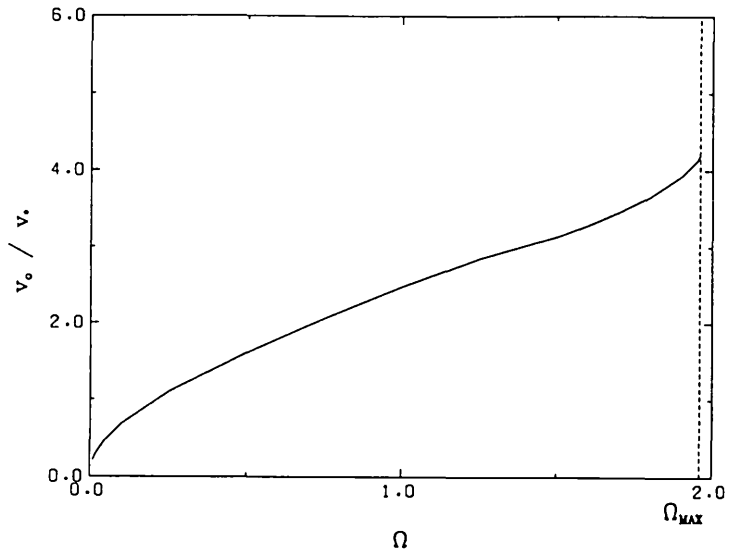


Figure 2.15 Non-stationary finite thermal conductivity equilibria: normalised edge velocity v_o/v_* as a function of Ω.

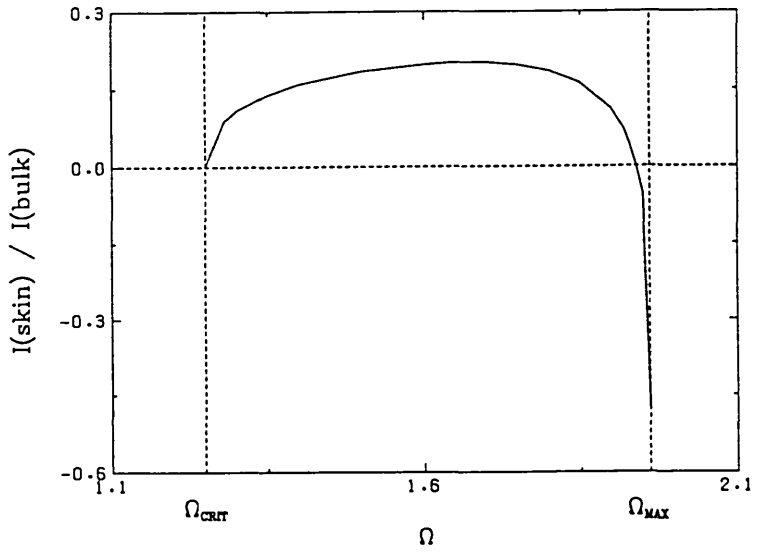


Figure 2.16 Non-stationary finite thermal conductivity equilibria: ratio of current flowing in skin to current carried inside pinch as a function of Ω.

If Ω exceeds 3/2 then the density never vanishes. However these solutions are not acceptable 'gas-embedded' equilibria since they require an *inward heat flow* at the plasma edge.

The physical interpretation of these non-stationary equilibria is discussed below.

2.4 Discussion and conclusions

Two classes of solution to the time-dependent Z-pinch equilibrium equations have been found: stationary equilibria confined by rising currents and expanding equilibria carrying falling currents. In both cases the form of the profiles has been found to depend critically on the value of a parameter Ω, defined by eqn. 2.26 or 2.66. The discussion in this section is primarily that of Coppins (Coppins *et. al.* 1988); for the sake of completeness his analysis is reproduced here.

For the stationary equilibria of section 2.2 the current density profiles become increasingly dominated by a skin current as Ω increased beyond a critical value Ω_{crit}. Physical insight into this behaviour is provided by considering the ratio of the field diffusion timescale $\tau_{diff} = \mu_o r_o^2/\eta$ to the characteristic timescale for the current rise $\tau_{ohm} = I / dI/dt = 3t$:

$$\tau_{diff}/\tau_{ohm} \simeq \mu_o r_o^2/3\eta(t)t = (1/3)\,(r_o/r_*)^2. \qquad (2.71)$$

Since r_o/r_* increases monotonically with Ω (figure 2.7) it can be seen that if $\Omega >> 1$ the pinch current is rising too rapidly for the current to diffuse into the pinch and so a skin current can be maintained. Increasing Ω therefore increases the fraction of the total current flowing in the skin (figure 2.8).

In the case of the non-stationary equilibria of section 2.3, the fact that at any time 't' the pinch radius is given by $r_o = v_o t$ shows that:

$$\tau_{diff}/\tau_{ohm} \simeq \mu_o v_o^2 t/3\eta(t) = (1/3)\,(v_o/v_*)^2 \qquad (2.72)$$

where in this case $\tau_{ohm} = I / |dI/dt| = 3t$ is the characteristic time for current *fall*. Again, since v_o/v_* is a monotonically increasing function of Ω (figure 2.15) it follows that if a fully diffused current is made to fall sufficiently rapidly (so that $\tau_{diff} >> \tau_{ohm}$) then a region of reversed current can arise at the edge of the

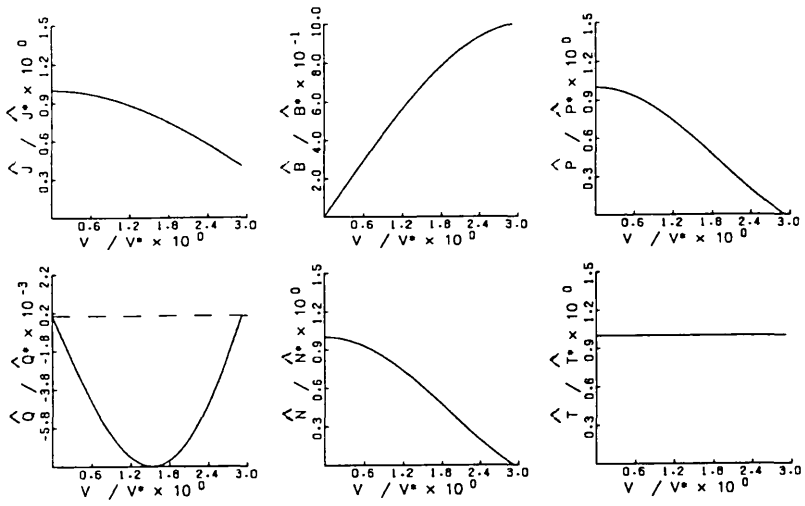


Figure 2.17 Infinite thermal conductivity non-stationary equilibrium.
$\Omega = \Omega_{crit} = 1.25$. *Normalisation as in figure 2.10.*

conductor (figures 2.14 and 2.16). This phenomenon has been called the *inverse skin effect* (Haines 1959, Culverwell *et. al.* 1989, and also chapter six) and it is a conspicuous feature of solutions close to Ω_{max}.

The normalised equations of this chapter can be be translated into more meaningful expressions by using equations 2.13 to 2.19 and 2.53 to 2.59: the radius 'r_o' of a stationary equilibrium pinch in SI units is then given by

$$r_o = 1.15 \times 10^{-7} \left[N^{3/4} \tau^{1/2} I_f^{-3/2}\right] x_o(\Omega) \qquad (2.73)$$

where τ is the duration of the dicharge, I_f is the final current (i.e $I_f = I(\tau)$), N is the pinch line density and $x_o(\Omega)$ is the value of r_o/r_* at the value of Ω. The calculation of eqn. 2.73 requires the use of the Bennett relation, which is justified since the bulk temperature profiles are relatively flat.

Since $x_o(\Omega_{crit}) \simeq 2.80$ the following classification of profiles is obtained:

$$\left.\begin{array}{ll} \text{Gas-embedded:} & r_o < \\ \text{Thermally isolated with} & \\ \text{a skin current:} & r_o > \end{array}\right\} 3.22\times10^{-7}\, N^{3/4}\, \tau^{1/2}\, I_f^{-3/2}. \qquad (2.74)$$

Similarly, the plasma edge expansion velocity of the non—stationary equilibria is found to be (SI units again)

$$v_o = 1.32 \times 10^{-14}\ N^{3/2}\, r_i^{-1}\, I_i^{-3}\ x_o^2(\Omega) \qquad (2.75)$$

where I_i and r_i are the initial current and radius respectively. Here, x_o is the value of v_o/v_*. Since thermally isolated equilibria are only obtainable in the range $\Omega_{crit} < \Omega < \Omega_{max}$ and

$$x_o(\Omega_{crit}) \simeq 2.84; \quad x_o(\Omega_{max}) \simeq 4.21 \qquad (2.76)$$

it follows that the possible expansion velocity of thermally isolated equilibria lies in the range

$$1.07 \times 10^{-13}\, N^{3/2} I_i^{-3} r_i^{-1} < v_o < 2.36 \times 10^{-13}\, N^{3/2} I_i^{-3} r_i^{-1}. \qquad (2.77)$$

If the fibre pinch experiments discussed in chapter one develop into the

'self−similar' equilibria described in this chapter (and numerical simulations by Rosenau *et. al.* (1989) and by Chittenden (private communication) suggest that they *do*) then those equilibria must be of the stationary thermally−isolated type. When typical parameters of the NRL experiment (I = 500 kA, τ = 130 ns, N = 5×10^{20} m^{-1}) are inserted into eqn. 2.74 a minimum radius of about 1 mm is produced. The observed pinch radius (formed from a 100 μm fibre) is about 0.2 mm − insufficient to allow the formation of a thermally isolated equilibrium. If, as is expected, the pinch is attempting to develop into one of these equilibria then it is clearly desirable to reduce the period of transition into one of these states since this will reduce the level of instability 'seeded' during the dynamic phase. Equation 2.74 shows that this can be done either by reducing the line density (i.e. fibre radius), increasing the peak current, or increasing the rate of rise of current.

The distributions of current, density, and temperature in the fibre pinch experiments have not been measured and so it is impossible to say which, if any, of the equilibria described here appear experimentally. This fact motivates the work of the next chapter, which is a study of the ideal MHD stability of the *entire range* of stationary equilibria described in this chapter.

Note added after viva:

Numerical simulations show that a Z−pinch always develops Ω_{crit} profiles with a radius given by eqn. 2.74 (Chittenden, private communication 1989). This is because the physics that determines the precise nature of the equilibrium (such as ion−acoustic instabilities in the low density region creating anomalous resistivity) is omitted from such simulations. There is no reason in principle why an experimental fibre pinch could not develop $\Omega > \Omega_{crit}$ profiles if its current were to rise rapidly enough, although a gas−embedded equilibrium ($\Omega < \Omega_{crit}$) would not be possible since fibre pinches are produced in vacuo. If Ω were to change during an experiment, the pinch would probably adjust its profiles and radius to those appropriate to the new value of Ω. It would be worth testing these hypotheses numerically, simulating $\Omega > \Omega_{crit}$ conditions by artificially supplying heat at the edge of the pinch.

CHAPTER THREE

THE IDEAL MHD STABILITY OF TIME-DEPENDENT EQUILIBRIA

3.1 The validity of ideal MHD at high temperatures

In the last chapter a class of stationary time-dependent resistive Z-pinch equilibria was studied. In these equilibria the current I(t) is proportional to $t^{1/3}$ which implies that $dI/dt \propto t^{-2/3}$, so that at late enough times the current varies arbitrarily slowly (see figure 1.6). In chapter one it was argued that in this regime the Lundquist number S is much greater than unity. Therefore ideal MHD is the correct model of Z-pinch stability in the high current, high temperature regime.

In this chapter the ideal MHD stability of the equilibria described in chapter two is discussed. This is to determine whether the anomalous stability of the fibre pinches described in chapter one could arise if the pinch developed into an equilibrium which had particularly enhanced stability properties in the ideal MHD regime.

In section 3.2 the effect on stability of the magnitude of the thermal conductivity is considered. The answer to this technical question is of great importance later in the thesis. In section 3.3 the modification of boundary condition 1.17 caused by a skin current in the equilibrium is discussed. This condition is then used in section 3.4 to analyse the effect of skin currents on the stability of a pinch in the ideal regime. There is a discussion of the main results of the chapter in section 3.5.

3.2 The effect of thermal conductivity

Ideal MHD is an adiabatic theory (zero thermal conductivity). The only 'realistic' equilibria (i.e ones with an edge) that are attainable in the resistive regime are the finite and infinite thermal conductivity solutions of sections 2.2.(ii) and 2.2.(iii). Nonetheless, the *magnitude* of the thermal conductivity term, $\nabla.\underline{q}$, is proportional to $t^{-1/3}$ for these equilibria and therefore vanishes as $t \to \infty$. For the same reason the Ohmic heating term, ηj^2, which is also proportional to $t^{-1/3}$ can be neglected in the large time limit. [It is precisely *because* ηj^2 and

$\nabla.q$ can be made to have the same time−dependence that a separable solution is possible.] Thus in the high temperature regime the stability of the resistive equilibria may be studied without inconsistency using ideal MHD theory.

The finite and infinite thermal conductivity $\Omega = \Omega_{crit}$ equilibria of figures 2.4 and 2.9 are incorporated into a shooting code (see chapter one), first written by C. Davies in 1979 (no references available). The respective $m = 0$, $kr_o = 1$ MHD eigenfunctions for each of these two equilibria are shown in figures 3.1 and 3.2, and for $m = 1$, $kr_o = 1$ modes in figures 3.3 and 3.4 respectively. The corresponding eigenfunctions are seen to be very similar in structure, the finite thermal conductivity solutions being slightly more sharply peaked in the higher temperature regime near the plasma edge. The growth rates, normalised with respect to the ion thermal transit time at the Bennett temperature, are 1.263, 1.238, 1.020, and 1.014 for figures 3.1, 3.2, 3.3, and 3.4 respectively. Over the range $0.1 < kr_o < 10$ the maximum difference in growth rates is less than 5% for both $m = 0$ and $m = 1$ modes. The conclusion is therefore clear: the magnitude of the equilibrium thermal conductivity has very little effect on the stability properties of a Z−pinch in the ideal MHD regime.

In chapters four and five a model of resistive Z−pinch behaviour is developed in which the perturbed temperature is uniform across the pinch. It is instructive to compare this isothermal model with the adiabatic ideal MHD theory. For the infinite thermal conductivity equilibria of section 2.2.(iii) the maximum difference in growth rates (in the ideal MHD phase) over the range $0.1 < kr_o < 10$ is less than 4% for $m = 0$ modes and less than 12% for $m = 1$ modes. Thus the difference in stability between the isothermal and adiabatic models is very small.

These considerations show that the stability properties of a Z−pinch in the high temperature regime are insensitive to the plasma temperature distribution in the pinch. This conclusion − and its extrapolation to the resistive regime − will be used in chapters four and five.

3.3 The boundary condition in the presence of skin currents

The $\Omega > \Omega_{crit}$ equilibria of section 2.2.(ii) are characterised by a finite pressure at the edge where the number density vanishes and the temperature diverges. The resulting discontinuity in the thermal pressure is balanced by the

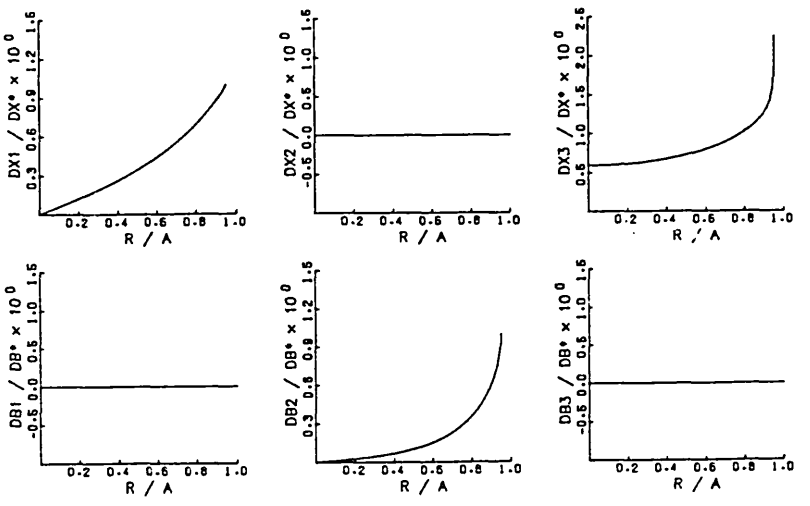


Figure 3.1 $m = 0$, $kr_o = 1$ *MHD eigenfunction for finite thermal conductivity* $\Omega = \Omega_{crit}$ *equilibrium (fig. 2.4).*
DX1 $= \xi_r/\max \xi_r$, *DX2* $= -i\xi_\theta/\max \xi_r$, *DX3* $= \xi_z/\max \xi_r$,
DB1 $= -iB_r^1/\max|B_\theta^1|$, *DB2* $= -B_\theta^1/\max|B_\theta^1|$,
DB3 $= -iB_z^1/\max|B_\theta^1|$, *a = pinch radius* r_o.

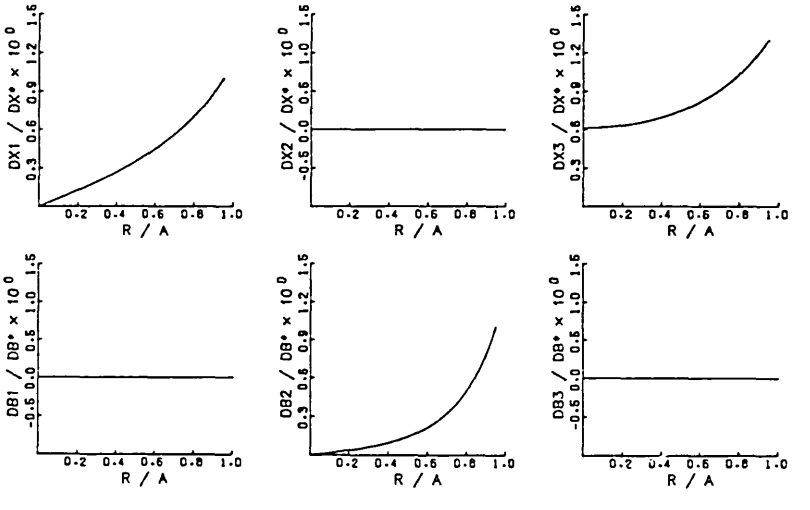


Figure 3.2 $m = 0$, $kr_o = 1$ *MHD eigenfunction for infinite thermal conductivity* $\Omega = \Omega_{crit}$ *equilibrium (fig. 2.9).*
Normalisation as in figure 3.1.

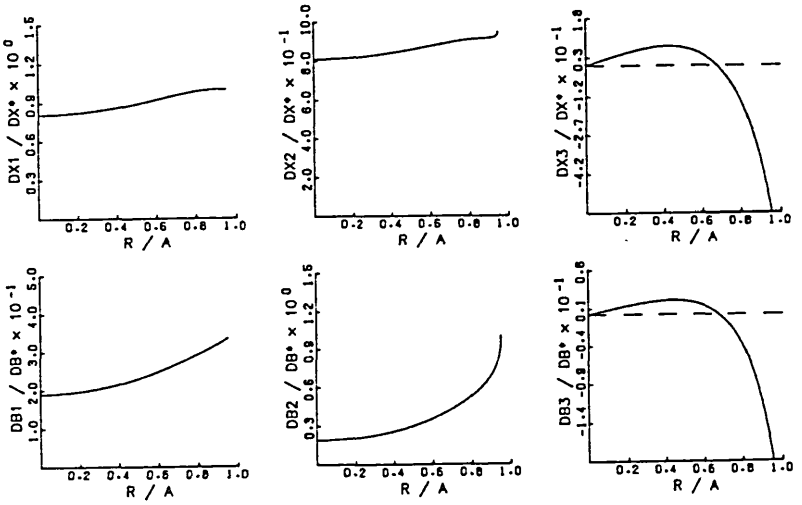


Figure 3.3 $m = 1$, $kr_o = 1$ *MHD eigenfunction for finite thermal conductivity* $\Omega = \Omega_{crit}$ *equilibrium (fig. 2.4). Normalisation as in figure 3.1.*

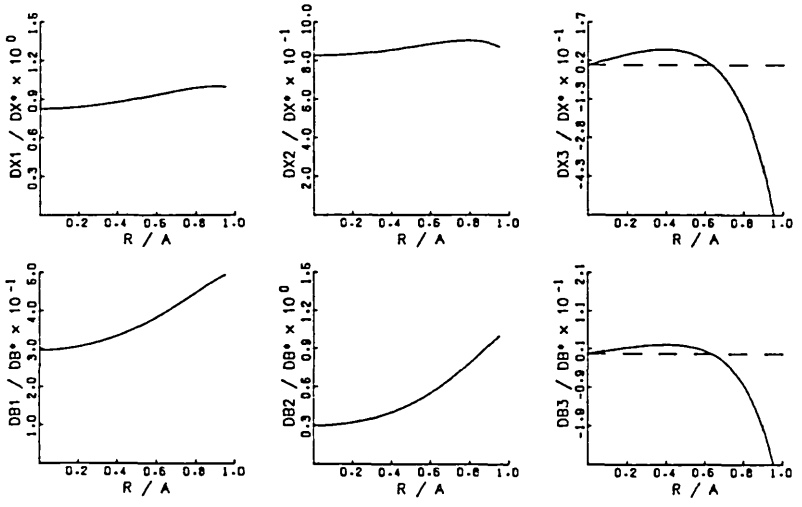


Figure 3.4 $m = 1$, $kr_o = 1$ *MHD eigenfunction for infinite thermal conductivity* $\Omega = \Omega_{crit}$ *equilibrium (fig. 2.9). Normalisation as in figure 3.1.*

discontinuity in the magnetic pressure associated with a skin current. The boundary condition in the presence of equilibrium skin currents is different from the standard condition (chapter one, eqn. 1.17) which assumes that the thermal pressure and magnetic field are continuous across the boundary. The modified boundary condition has been calculated by M. Coppins, although the derivation has never been published and so it is included here for the sake of completeness.

Schmidt (1979, p 119) considers the continuity of the total (thermal plus magnetic) pressure across the perturbed boundary of a Z−pinch and, after linearising, obtains the following expression for $\underline{\xi}$, the plasma displacement at the boundary in terms of the perturbed and equilibrium plasma variables:

$$- \mu_0 \Gamma p^0 \nabla.\underline{\xi} + \underline{B}^0.[\underline{B}^1 + (\underline{\xi}.\nabla)\underline{B}^0] = \underline{B}_v{}^0.[\underline{B}_v{}^1 + (\underline{\xi}.\nabla)\underline{B}_v{}^0] \qquad (3.1)$$

where the subscript 'v' denotes vacuum variables which are to be evaluated just *outside* the unperturbed boundary (i.e. at $r = r_0{}^+$), while the quantities on the left hand side of eqn. 3.1 are to be evaluated just *inside* the unperturbed radius (i.e. at $r = r_0{}^-$). The ideal MHD energy equation (1.6) and the continuity equation (1.3) give, after linearisation and integration with respect to time,

$$p^1 + (\underline{\xi}.\nabla)\, p^0 + \Gamma\, p^0\, \nabla.\underline{\xi} = 0. \qquad (3.2)$$

Use of the identity

$$\underline{B}.(\underline{\xi}.\nabla)\underline{B} = \underline{\xi}.\nabla(B^2/2), \qquad (3.3)$$

the equilibrium pressure balance condition

$$\nabla(p^0 + B^{0\,2}/2\mu_0) = (\underline{B}.\nabla)\underline{B}/\mu_0, \qquad (3.4)$$

and the result $B_{\theta v}{}^0 \propto r^{-1}$ enables eqn. 3.1 to be rewritten as

$$\mu_0 p^1 + B_\theta{}^0 B_\theta{}^1 + (\xi_r/r_0)(B_{\theta v}{}^{0\,2} - B_\theta{}^{0\,2}) - B_{\theta v}{}^0 B_{\theta v}{}^1 = 0. \qquad (3.5)$$

Outside the plasma the perturbed magnetic field $\underline{B}^1$ is divergence− and curl−free, and may therefore be written as the gradient of a harmonic potential φ. In cylindrical coordinates the solution of $\nabla^2\varphi = 0$, regular at infinity, having the z− and θ−dependence $\exp(ikz - im\theta)$ is

$$\varphi = C\, K_m(kr)\, \exp(ikz - im\theta) \qquad (3.6)$$

where C is an arbitrary constant and K_m is a modified Bessel function of the second kind. [The 'I_m' solution is rejected as it diverges at infinity.] The perturbed vacuum magnetic field is therefore

$$\underline{B}_v^1 = \nabla\varphi = C(kK_m'(kr),\ -imK_m(kr)/r,\ ikK_m(kr))\exp(ikz-im\theta). \qquad (3.7)$$

A further boundary condition is given by the continuity of the normal component of the magnetic field across the perturbed boundary. Schmidt (p 129) shows that this reduces to

$$B_{rv}^1(r_o^+) = -(im/r_o)\, B_\theta^0(r_o^+)\, \xi_r(r_o^-). \qquad (3.8)$$

Substitution of eqn. 3.8 into 3.7 then expresses C in terms of $\xi_r(r_o^-)$ which then enables eqn. 3.5 to be written:

$$(\xi_r/r_o)\{B_{\theta v}^{02} - B_\theta^{02} + B_{\theta v}^{02}[m^2K_m(kr_o)/kr_oK_m'(kr_o)]\}$$

$$+ \mu_o\, p^1 + B_\theta^0 B_\theta^1 = 0. \qquad (3.9)$$

Writing

$$2\pi r_o\, B_\theta^0 = \mu_o\, I_{bulk} \qquad (3.10)$$

and

$$2\pi r_o\, B_{\theta v}^0 = \mu_o\, (I_{bulk} + I_{skin}) \qquad (3.11)$$

(from Ampere's law) finally gives

$$\mu_o\, p^1 + B_\theta^0 B_\theta^1 + \xi_r[\mu_o^2/4\pi^2 r_o^3]\{I_{skin}(I_{skin} + 2I_{bulk}) +$$

$$(I_{skin} + I_{bulk})^2 m^2 K_m(kr_o)/kr_oK_m'(kr_o)\} = 0. \qquad (3.12)$$

Equation 3.12 is the required modified boundary condition. It agrees with the usual expression (eqn. 1.17) when $I_{skin} = 0$; when $I_{bulk} = 0$ it leads to Tayler's dispersion relation for a pure skin current equilibrium (Tayler 1957a):

$$\Gamma W_o^2 I_m(Z_o)/2Z_oI_m'(Z_o) = 1 + m^2K_m(X_o)/X_oK_m'(X_o) \qquad (3.13a)$$

where

$$X_o = kr_o,\ W_o^2 = \gamma^2 r_o^2 \rho^0/\Gamma p^0,\ Z_o^2 = X_o^2 + W_o^2, \qquad (3.13b)$$

and γ is the growth rate.

3.4 The effect on stability of a skin current

In this section the ideal MHD stability of the skin current equilibria of section 2.2.(ii) is studied.

The fraction of the total current carried in the skin can be calculated by the formula

$$I_{skin}/(I_{skin} + I_{bulk}) = 1 - [1 + 2\mu_o p^0(r_o^-)/B^{02}(r_o^-)]^{-1/2} \qquad (3.14)$$

which is derived by integrating the equilibrium pressure balance condition across the skin current at the boundary:

$$[p^0 + B^{02}/2\mu_o](r_o^-) = [B_v^{02}/2\mu_o](r_o^+), \qquad (3.15)$$

where $B^0(r_o^-)$ and $B_v^0(r_o^+)$ are related to the bulk current I_{bulk} and the skin current I_{skin} by equations 3.10 and 3.11. Equation 3.14 was used in the preparation of figures 2.8 and 2.16 of chapter two.

The application of eqn. 3.14 allows equilibria defined by any value of Ω (greater than Ω_{crit}) to be incorporated into the shooting code, modified by the appropriate boundary condition 3.12, enabling a study of their ideal MHD stability to be made.

Figure 3.5 shows the $m = 0$, $kr_o = 0.25$ eigenfunctions for the equilibrium defined by $\Omega = 100$. The skin current comprises nearly 20% of the total current in this equilibrium, which is shown in figure 2.6. Figure 3.6 is the corresponding graph for $m = 1$ modes. ξ_z and B_z^1 are clearly peaked at the edge. Figures 3.7 and 3.8 are the eigenfunctions corresponding to figures 3.5 and 3.6 for $kr_o = 10$ modes. As expected, the profiles become more concentrated near the plasma edge as the wavelength decreases. The normalised growth rates for figures 3.5, 3.6, 3.7, and 3.8 are 0.380, 0.462, 4.958, and 4.264 respectively.

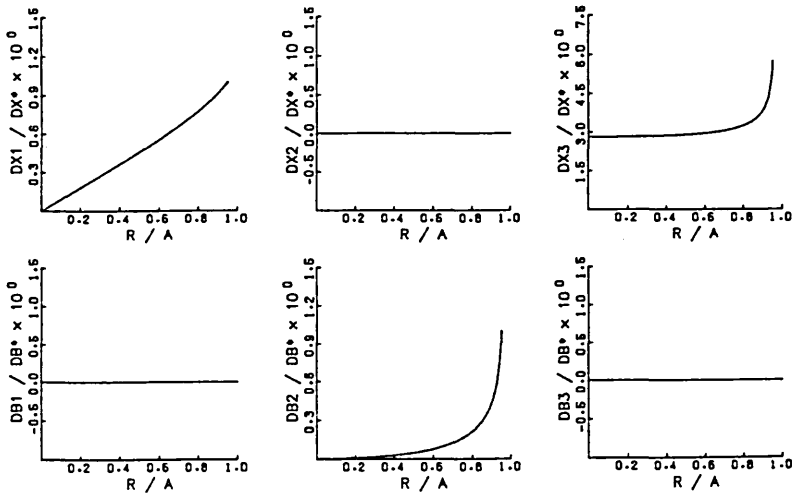


Figure 3.5 $m = 0$, $kr_o = .25$ *MHD eigenfunction for finite thermal conductivity* $\Omega = 100$ *equilibrium (fig. 2.6). Normalisation as in figure 3.1.*

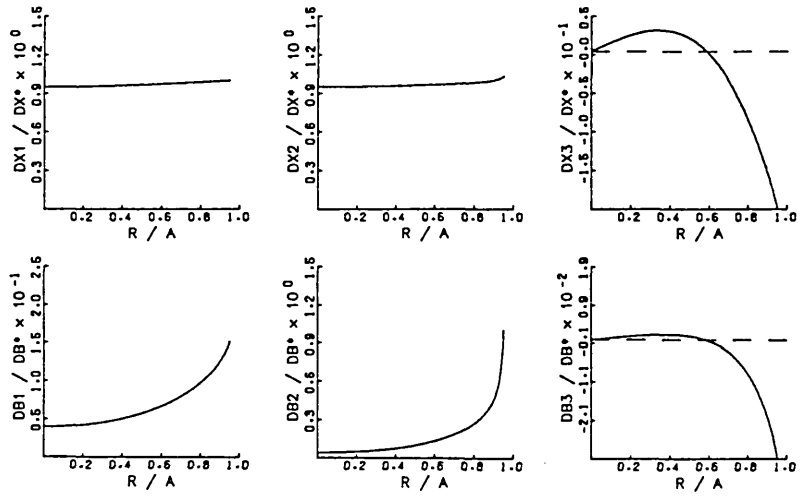


Figure 3.6 $m = 1$, $kr_o = .25$ *MHD eigenfunction for finite thermal conductivity* $\Omega = 100$ *equilibrium (fig. 2.6). Normalisation as in figure 3.1.*

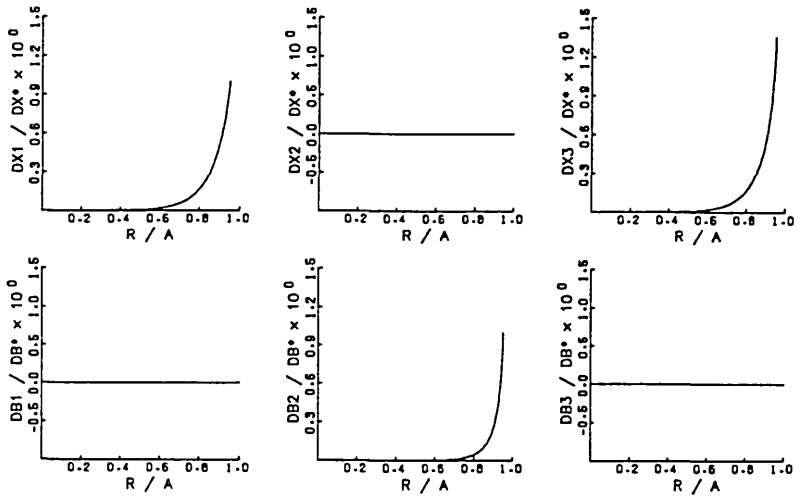


Figure 3.7 $m = 0$, $kr_o = 10$ *MHD eigenfunction for finite thermal conductivity* $\Omega = 100$ *equilibrium (fig. 2.6). Normalisation as in figure 3.1.*

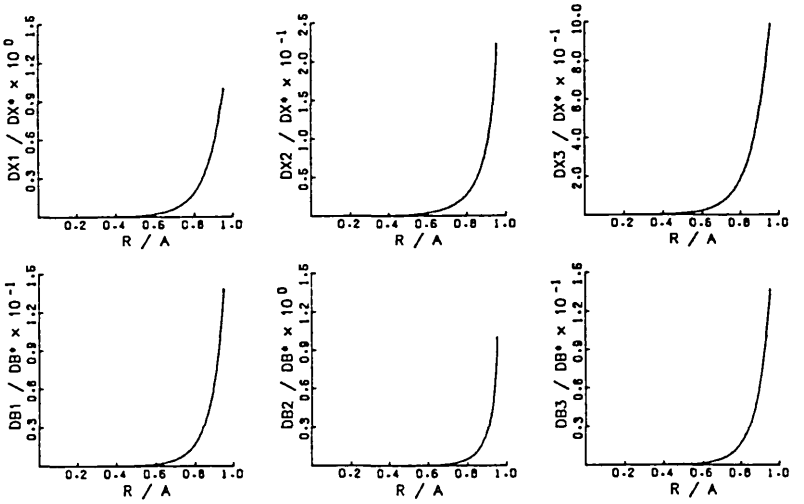


Figure 3.8 $m = 1$, $kr_o = 10$ *MHD eigenfunction for finite thermal conductivity* $\Omega = 100$ *equilibrium (fig. 2.6). Normalisation as in figure 3.1.*

Fig 3.9 displays the normalised ideal MHD growth rates as a function of the fraction of current carried in the skin for m = 0 and m = 1 modes at a wavelength given by kr_0 = 0.25. Figure 3.10 is the corresponding graph for kr_0 = 10 modes. Numerically it is possible to study equilibria with up to 95% of the current flowing in the skin (these are defined by $\Omega = 10^{96}$); the growth rates for the pure skin current equilibria were found by solving Tayler's dispersion relation 3.13. The weak destabilizing effect of a skin current on the pinch is apparent. Even where the effect is most pronounced, short wavelength m = 1 modes, the variation in growth rate over the entire range of skin currents is less than 50%.

3.5 Discussion and conclusions

In this chapter the ideal MHD stability of the stationary time-dependent thermally-isolated equilibria of chapter two has been studied. The use of this theory in the high temperature regime was justified by showing that the form of the temperature distribution, either in the equilibrium or in the perturbation, has very little effect on the stability of the pinch. This result will be of much help in chapters four and five.

It was shown in section 3.4 that there is little change in the growth rate over the entire range of accessible thermally isolated equilibria. This is a valuable result since it is not known which equilibrium appears in any particular experimental situation. The maximum current in the recent fibre pinch experiments is insufficient to allow the plasma to reach the *collisionless* regime (see figure 1.5). Since the work of this chapter shows that the enhanced stabilty of these pinches cannot be attributed to the development of a particularly stable equilibrium in the *ideal* phase, it must be due to *resistive* effects occurring in the early part of the experiment. The next two chapters are devoted to a detailed test of this hypothesis.

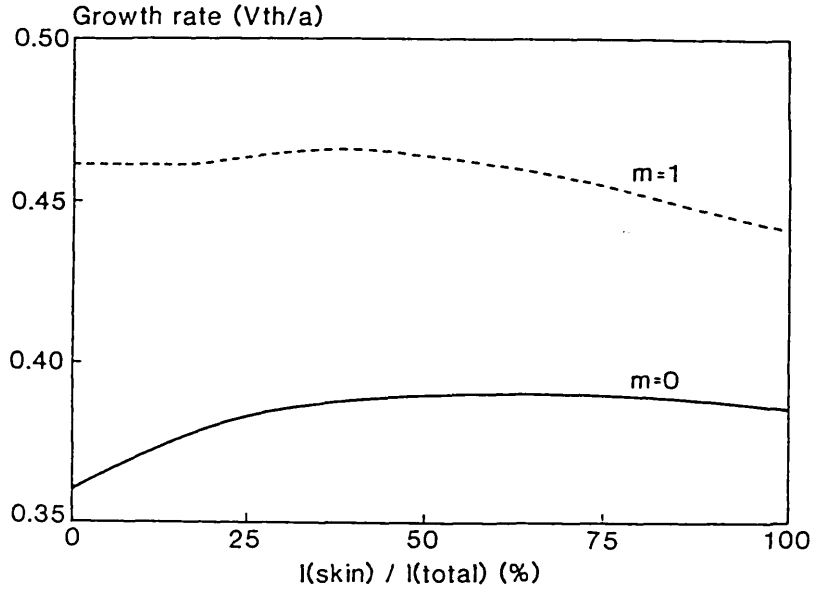


Figure 3.9 *m = 0 and m = 1 normalised ideal MHD growth rates as functions of the fraction of the total current carried in the skin.* $kr_o = 0.25$.

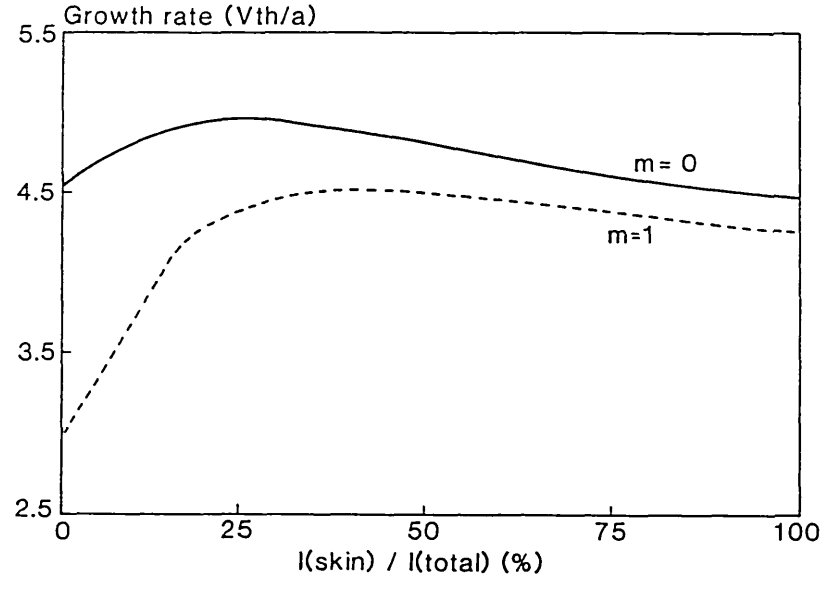


Figure 3.10 *m = 0 and m = 1 normalised ideal MHD growth rates as functions of the fraction of the total current carried in the skin.* $kr_o = 10.0$.

CHAPTER FOUR

THE DEVELOPMENT OF AXISYMMETRIC (M = 0) PERTURBATIONS IN THE RESISTIVE REGIME

4.1 Introduction

The analysis of chapter three concluded that the anomalous stability of the deuterium fibre Z-pinches could not be explained by the development of a stable equilibrium during the ideal phase: all of the equilibria of chapter two are unstable to a similar degree according to ideal MHD theory. It is therefore natural to ask if resistive effects during the low current phase of the experiments could be the cause of the enhanced stability. This chapter and the next are devoted to a study of this question.

It was repeatedly emphasised in chapter one that when resistivity is important it is essential to include the time-dependence of the equilibrium. This rules out the possibility of studying the problem via an eigenvalue equation (as can be done in ideal MHD) where the perturbed quantities are assumed to have the time dependence $\exp(i\omega t)$. Mathematically this is because 't' is not an ignorable coordinate in the resistive regime because the equilibrium is varying in time. However, the equilibrium is cylindrically symmetrical and so it *is* possible to Fourier analyse in θ and z, perturbed variables being proportional to $\exp(ikz - im\theta)$. In a linearised analysis each such normal mode evolves independently and attention can therefore be concentrated on each one separately.

This chapter is concerned with the development of axisymmetric (m = 0) perturbations in the time-dependent equilibrium of section 2.2.(iii). For the reasons discussed above, a linearised, Fourier analysed, initial value approach to the problem is adopted. The system of equations and boundary conditions are described in section 4.2. These equations are too complicated to study analytically and therefore in section 4.3 the details of the numerical scheme used to solve the equations are discussed. In section 4.4 various tests of the code are discussed. In section 4.5 the results of the code are described. Finally in section 4.6 the principal conclusions of the chapter are discussed.

4.2 Equations and boundary conditions

The basic equations are the standard resistive MHD equations 1.3, 1.4, 1.7, 1.8, 1.22, and 1.23 together with the perfect gas equation of state 1.24. Viscosity and bremsstrahlung emission are neglected. For the sake of reference the equations are repeated here.

$$\partial n/\partial t = -\nabla \cdot (n\underline{v}) \tag{4.1}$$

$$\rho \, d\underline{v}/dt = \underline{j} \wedge \underline{B} - \nabla p \tag{4.2}$$

$$\partial \underline{B}/\partial t = \nabla \wedge (\underline{v} \wedge \underline{B} - \eta \underline{j}) \tag{4.3}$$

$$\mu_o \, \underline{j} = \nabla \wedge \underline{B} \tag{4.4}$$

$$p = 2 \, n \, k_B \, T \tag{4.5}$$

$$n^\Gamma \, d(p/n^\Gamma)/dt = (\Gamma-1)\{\eta j^2 - \nabla \cdot \underline{q}\} \tag{4.6}$$

The equilibrium and perturbed temperatures are assumed to be uniform across the pinch (though not, of course, constant in time). Section 3.2 of chapter three demonstrated that these are excellent approximations in the ideal MHD regime, and in view of the very significant simplification of the system of equations that is achieved by assuming uniform temperatures, the same approximations are made in the following discussion. It would be possible in principle, though difficult in practice, to admit finite temperature gradients into the model.

For the reasons just discussed the equilibrium is assumed to be the infinite thermal conductivity model of section 2.2.(iii) which, again for completeness, is repeated here.

$$v_r{}^0(r, t) \equiv 0 \tag{4.7}$$

$$j_z{}^0(r, t) = j_z{}^0(0, \tau) I_0(r/\sqrt{3}r_*)(t/\tau)^{1/3} \tag{4.8}$$

$$n^0(r, t) = n^0(0, \tau)\{1 + (3/2\Omega_{crit})(1 - I_0{}^2(r/\sqrt{3}r_*))\} \tag{4.9}$$

$$T^0(r, t) = T^0(0, \tau)(t/\tau)^{2/3} \tag{4.10}$$

where $$r_*^2 = \eta^0(0, \tilde{\tau})\tilde{\tau}/\mu_o, \qquad (4.11)$$

$\tilde{\tau}$ is a convenient reference time, and the $\Omega = \Omega_{crit}$ limit has been taken to ensure that the equilibrium is thermally isolated. In order to obtain the equations describing the evolution of the perturbation the general plasma equations 4.1 to 4.6 are linearised and the perturbed variables are assumed to have the z−dependence exp(ikz). For m = 0 modes v_θ^1, B_r^1, and B_z^1 vanish by symmetry, and v_z^1 is $\pi/2$ out of phase with the other variables. Since the thermal conductivity is assumed to be infinite and the temperature gradients are zero the first order heat flux $\underline{q}^1$ is indeterminate. This difficulty is overcome by integrating eqn. 4.6 over the volume of the pinch: the troublesome term $\nabla.\underline{q}^1$ then becomes transformed to the integral of $\underline{q}^1$ over the surface of the pinch, and this term vanishes on the assumption that the pinch is thermally isolated. Further manipulation of the resulting equation leads to an expression for the rate of change of the perturbed temperature.

By implementing the above procedures the following system of equations is produced:

$$\partial n^1/\partial t = (-1/r)\partial(rn^0v_r^1)/\partial r - ikn^0v_z^1 \qquad (4.12)$$

$$m_i n^0 \partial v_r^1/\partial t = -\partial(p^1 + B_\theta^0 B_\theta^1/\mu_o)/\partial r - 2B_\theta^1 B_\theta^0/\mu_o r \qquad (4.13)$$

$$m_i n^0 \partial v_z^1/\partial t = -ik(p^1 + B_\theta^0 B_\theta^1/\mu_o) \qquad (4.14)$$

$$\partial B_\theta^1/\partial t = -ikv_z^1 B_\theta^0 - \partial(v_r^1 B_\theta^0 - \eta^1 j_z^0)/\partial r$$

$$- \eta^0 k^2 B_\theta^1/\mu_o + (\eta^0/\mu_o)(\partial/\partial r)(1/r\ \partial/\partial r(rB_\theta^1)) \qquad (4.15)$$

$$dT^1/dt = (1/N)\int_0^{r_o} ((\Gamma-1)/2k_B)\{\eta^1 j_z^{0\,2} + 2\eta^0 j_z^0 j_z^1 - 2k_B n^0 T^0 \nabla.\underline{v}\}$$

$$- n^1 dT^0/dt\ \ 2\pi r dr \qquad (4.16)$$

(where N is the line density of the pinch)

$$\mu_o j_z^1 = 1/r\ \partial(rB_\theta^1)/\partial r \qquad (4.17)$$

$$p^1/p^0 = n^1/n^0 + T^1/T^0 \qquad (4.18)$$

$$\eta^1/\eta^0 = (-3/2)\ T^1/T^0 \qquad (4.19)$$

In the above it must be remembered that the equilibrium variables (superscript 0) depend on time. Since this is a linear scheme, however, the perturbed variables (superscript 1) do not 'feed−back' onto the equilibrium variables, so that the time−dependencies of these latter quantities may be programmed according to the simple power law dependencies defined by equations 4.7 to 4.10. This is a great strength of the 'separable solutions' of chapter two numerically: the equilibrium profiles only need to be calculated once, not at every timestep, since it is only the *magnitudes* of the equilibrium variables, not their *profiles*, that depend on time.

The eight equations 4.12 to 4.19 are sufficient to determine the temporal evolution of the 8 variables v_r^1, v_z^1, B_θ^1, j_z^1, η^1, T^1, n^1, and p^1. The details of the numerical scheme used to solve these equations will be found in the next section, but briefly: the continuity equation 4.12 and the equations of motion 4.13 and 4.14 are solved in a leap−frog fashion, the energy equation 4.16 is solved by first order Euler integration and the magnetic field diffusion equation 4.15 is solved fully implicitly. The boundary condition, as in ideal MHD, is given by (equation 1.17, chapter one):

$$(p^1 + B_\theta^0 B_\theta^1/\mu_o) = 0 \qquad (4.20)$$

at $r = r_o$, together with the vanishing of $(\underline{j} \wedge \underline{B} - \nabla p)^1$ at the plasma edge. If this latter condition is not satisfied then the first−order perturbed velocities v_r^1 and v_z^1 would diverge at the edge since the equilibrium density n^0 vanishes there.

4.3 Details of the numerical scheme

The first step in the numerical analysis of equations 4.12 to 4.19 is to show that they may be normalised in such a way that the results of the code are 'universal', in the sense that the essential results of the problem can be found without having to solve the system of equations over a wide range of the parameters r_o, τ, $I(\tau)$ and N.

The normalising distance scale 'r_*' has already been defined by eqn. 4.11. If the normalising timescale 'τ' is defined through

$$r_*^2/\tau^2 = 2k_BT(0, \tau)/m_i \qquad (4.21)$$

and the other (equilibrium or perturbed) variables are normalised according to

$$\hat{r} = r / r_*, \quad \hat{t} = t / \tau, \quad \hat{\underline{v}} = \underline{v} / (r_*/\tau), \quad \hat{n} = n / n(0, \tau),$$

$$\hat{p} = p / p(0, \tau), \quad \hat{T} = T / T(0, \tau), \quad \hat{\eta} = \eta / \eta(0, \tau),$$

$$\hat{\underline{B}} = \underline{B} / \sqrt{(\mu_o\, p(0, \tau))}, \quad \hat{k} = k / r_*^{-1} \qquad (4.22)$$

then equations 4.12 to 4.19 can be reduced to PDEs in the 'hatted' variables with respect to $\hat{r}$ and $\hat{t}$, without any factors of m_i, $2k_B$ or μ_o and with no dimensionless free parameters left in the system (c.f. the appearance of Ω after the equilibrium equations of chapter two had been normalised). Henceforth 'hats' will be dropped, it being understood implicitly that all variables are normalised in this sense. Note that with the normalisation of eqns 4.22 the pinch radius r_o is *not* equal to unity: rather, $r_o = 2.80$ (section 2.2.(iii)).

The computational grid used in the numerical solution of the equations is an Eulerian (i.e. fixed) grid comprising NC (typically 100) equally spaced radial cells. The most natural way to difference the equations is to choose $v_r{}^1$ to be defined at the cell *boundaries* (subscript i+1/2 (= 1/2, 3/2, ..., NC+1/2)) and for the other variables to be defined at the cell *centres* (subscript i (= 1, 2, ..., NC)). The position of the axis of the pinch is defined by i=1/2, its edge by i=NC+1/2. In order to facilitate a leap−frog solution of the equations of continuity and motion the velocities $v_r{}^1$ and $v_z{}^1$ are defined at the 'half−times' (superscript m+1/2) while n^1, p^1, and $B_\theta{}^1$ are defined at the 'integer−times' (superscript m). T^1 and η^1 are defined at both times. The equilibrium variables are defined at the cell centres *and* boundaries since, as already stated, they only need to be calculated once; similarly they are defined at *both* time steps.

The initial conditions specify $v_r{}^1{}_{i+1/2}{}^{-1/2}$, $v_z{}^1{}_{i+1/2}{}^{-1/2}$, $B_\theta{}^1{}_i{}^0$, $n^1{}_i{}^0$, $p^1{}_i{}^0$, $T^1{}^0$, $\eta^1{}^0$, $T^1{}^{-1/2}$, and $\eta^1{}^{-1/2}$. These variables are then advanced to the next timestep according to the following set of equations (boundary conditions to be given later):

$$n^0_{i+1/2}\,\frac{v^1_{r\ i+1/2}{}^{m+1/2} - v^1_{r\ i+1/2}{}^{m-1/2}}{\Delta t} = -\frac{B^0_{\theta\ i+1/2}{}^{m}(B^1_{\theta\ i}{}^{m} + B^1_{\theta\ i+1}{}^{m})}{r_{i+1/2}}$$

$$-\frac{p^1_{i+1}{}^{m} - p^1_{i}{}^{m} + B^1_{\theta\ i+1}{}^{m}B^0_{\theta\ i+1}{}^{m} - B^1_{\theta\ i}{}^{m}B^0_{\theta\ i}{}^{m}}{\Delta r} \qquad (4.23)$$

$$n^0_{\ i}\,\frac{v^1_{z\ i}{}^{m+1/2} - v^1_{z\ i}{}^{m-1/2}}{\Delta t} = -ik(p^1_{\ i}{}^{m} + B^1_{\theta\ i}{}^{m}B^0_{\theta\ i}{}^{m}) \qquad (4.24)$$

$$\frac{n^1_{\ i}{}^{m+1} - n^1_{\ i}{}^{m}}{\Delta t} = -ikn^0_{\ i}\,v^1_{z\ i}{}^{m+1/2} -$$

$$\frac{r_{i+1/2}n^0_{i+1/2}\,v^1_{r\ i+1/2}{}^{m+1/2} - r_{i-1/2}n^0_{i-1/2}v^1_{r\ i-1/2}{}^{m+1/2}}{r_i\Delta r} \qquad (4.25)$$

$$\frac{T^1_{\ }{}^{m+1/2} - T^1_{\ }{}^{m-1/2}}{\Delta t} = \frac{1}{N}\sum_{i=1}^{NC}(\Gamma-1)\{\eta^1_{\ }{}^{m}\,j^0_{z\ i}{}^{m}\,j^0_{z\ i}{}^{m} + 2\eta^0_{\ }{}^{m}j^0_{z\ i}{}^{m}j^1_{z\ i}{}^{m}$$

$$-\,p^0_{\ i}{}^{m+1/2}\left(\frac{r_{i+1/2}v^1_{r\ i+1/2}{}^{m+1/2} - r_{i-1/2}v^1_{r\ i-1/2}{}^{m+1/2}}{r_i\Delta r} + ikv^1_{z\ i}{}^{m+1/2}\right)\}$$

$$-\frac{2n^1_{i}{}^{m}\,T^0_{\ }{}^{m}}{3\ t^m}\ .\ 2\pi r_i\Delta r \qquad (4.26)$$

where $N = \sum_{i=1}^{NC} n^0_{\ i}\ 2\pi r_i\Delta r$ is the pinch line density (4.27)

and $j^1_{z\ i}{}^{m} = \dfrac{r_{i+1/2}(B^1_{\theta\ i+1}{}^{m} + B^1_{\theta\ i}{}^{m}) - r_{i-1/2}(B^1_{\theta\ i}{}^{m} + B^1_{\theta\ i-1}{}^{m})}{2r_i\Delta r}$. (4.28)

$$\frac{\eta^1_{\ }{}^{m+1/2}}{\eta^0_{\ }{}^{m+1/2}} = -\frac{3\ T^1_{\ }{}^{m+1/2}}{2\ T^0_{\ }{}^{m+1/2}} \qquad (4.29)$$

$$\frac{B_{\theta\ i}^{1\ m+1} - B_{\theta\ i}^{1\ m}}{\Delta t} = - ik\, v_{z\ i}^{1\ m+1/2} B_{\theta\ i}^{0\ m+1/2} - \eta^{0\ m+1} k^2 B_{\theta\ i}^{1\ m+1}$$

$$- \frac{v_{r\ i+1/2}^{1\ m+1/2} B_{\theta\ i+1/2}^{0\ m+1/2} - v_{r\ i-1/2}^{1\ m+1/2} B_{\theta\ i-1/2}^{0\ m+1/2}}{\Delta r}$$

$$- \frac{\eta^{1\ m+1/2} j_{z\ i+1/2}^{0\ m+1/2} - \eta^{1\ m+1/2} j_{z\ i-1/2}^{0\ m+1/2}}{\Delta r}$$

$$+ \frac{\eta^{0\ m+1}}{(\Delta r)^2} \left(\frac{r_{i+1} B_{\theta\ i+1}^{1\ m+1} - r_i B_{\theta\ i}^{1\ m+1}}{r_{i+1/2}} - \frac{r_i B_{\theta\ i}^{1\ m+1} - r_{i-1} B_{\theta\ i-1}^{1\ m+1}}{r_{i-1/2}} \right) \qquad (4.30)$$

$$\frac{T^{1\ m+1} - T^{1\ m}}{\Delta t} = \frac{1}{N} \sum_{i=1}^{NC} (\Gamma-1) \{ \eta^{1\ m+1/2} j_{z\ i}^{0\ m+1/2} j_{z\ i}^{0\ m+1/2}$$

$$+ 2\eta^{0\ m+1/2} j_{z\ i}^{0\ m+1/2} j_{z\ i}^{1\ m+1}$$

$$- p_i^{0\ m+1/2} \left(\frac{r_{i+1/2} v_{r\ i+1/2}^{1\ m+1/2} - r_{i-1/2} v_{r\ i-1/2}^{1\ m+1/2}}{r_i \Delta r} + ik v_{z\ i}^{1\ m+1/2} \right) \}$$

$$- \frac{2 n_i^{1\ m+1}\ T^{0\ m+1}}{3\ t^{m+1}} \cdot 2\pi r_i \Delta r \qquad (4.31)$$

where $$j_{z\ i}^{1\ m+1} = \frac{r_{i+1/2}(B_{\theta\ i+1}^{1\ m+1} + B_{\theta\ i}^{1\ m+1}) - r_{i-1/2}(B_{\theta\ i}^{1\ m+1} + B_{\theta\ i-1}^{1\ m+1})}{2 r_i \Delta r}. \qquad (4.32)$$

$$\frac{\eta^{1\ m+1}}{\eta^{0\ m+1}} = - \frac{3\ T^{1\ m+1}}{2\ T^{0\ m+1}} \qquad (4.33)$$

$$\frac{p_i^{1\ m+1}}{p_i^{0\ m+1}} = \frac{n_i^{1\ m+1}}{n_i^{0\ m+1}} + \frac{T^{1\ m+1}}{T^{0\ m+1}} \qquad (4.34)$$

The loop of equations 4.23 to 4.34 is then repeated to advance the variables to the next timestep.

The implicit diffusion terms of the magnetic field diffusion equation 4.30 are solved by a standard tridiagonal recursion technique (e.g Potter 1974 p 88).

The boundary conditions employed on axis are:

$$v_r{}^1{}_{1/2}{}^{m+1/2} = 0 \qquad (4.35)$$

and

$$B_\theta{}^1{}_1{}^m = (1/3)\, B_\theta{}^1{}_2{}^m. \qquad (4.36)$$

The first condition arises from the symmetry of axisymmetric perturbations: there is no displacement of the axis. The second comes from the postulated finiteness of $j_z{}^1$ on axis, which implies that $B_\theta{}^1 \propto r$ for small r, so that $B_\theta{}^1{}_1{}^m = B_\theta{}^1(\Delta r/2, m\Delta t) = (1/3)B_\theta{}^1(3\Delta r/2, m\Delta t) = (1/3)B_\theta{}^1{}_2{}^m$.

Boundary condition 4.20 at the edge is satisfied by incorporating the following condition in the tridiagonal inversion routine for $B_\theta{}^1$:

$$\breve{p}^1{}_{NC}{}^{m+1} + B_\theta{}^1{}_{NC}{}^{m+1} B_\theta{}^0{}_{NC}{}^{m+1} = (1/3)\,[\breve{p}^1{}_{NC-1}{}^{m+1} + B_\theta{}^1{}_{NC-1}{}^{m+1} B_\theta{}^0{}_{NC-1}{}^{m+1}] \qquad (4.37)$$

where $\breve{p}^1$ is an approximation to p^1 (which is not calculated until B^1 has been advanced to time m+1) obtained by using the estimate $T^{m+1} \simeq (3/2)T^{m+1/2} - (1/2)T^{m-1/2}$ in equation 4.34. $v_r{}^1{}_{NC+1/2}{}^{m+1/2}$ cannot be calculated by equation 4.23 because $n^0{}_{NC+1/2}{}^m = 0$, but since this velocity only ever appears as a small part of the integrands of eqns. 4.26 and 4.31 a simple linear extrapolation is used to define $v_r{}^1$ at the edge of the pinch:

$$v_r{}^1{}_{NC+1/2}{}^{m+1/2} = 2v_r{}^1{}_{NC-1/2}{}^{m+1/2} - v_r{}^1{}_{NC-3/2}{}^{m+1/2} \qquad (4.38)$$

This is not entirely satisfactory, but it works in practice.

Since the system of equations 4.12 to 4.19 contains sound waves, Alfven waves and magnetic field diffusion, the timestep Δt employed in the code is limited by the following hybrid diffusion-CFL condition:

$$\Delta t = \lambda \min\{(\Delta r)^2/2\eta^0,\ \Delta r/\sqrt{(B^{0\,2}/n^0)},\ \Delta r/\sqrt{(\Gamma p^0/n^0)}\} \qquad (4.39)$$

where, for accuracy and stability the multiplier λ is usually taken to be 0.1. At early times the equations are dominated by diffusion and $\Delta t \propto (\eta^0)^{-1} \propto t$, while at later times advection dominates and $\Delta t \propto (B^0)^{-1} \propto t^{-1/3}$.

4.4 Tests of the numerical scheme

The following tests were performed on the computer coded version of the numerical scheme described above.

The first test is the invariance of the results of the code under a reduction of the cell size Δr. By equation 4.39 this automatically leads to a reduction in the timestep Δt. The calculations leading to figures 4.1 to 4.6 (see later) were found to be invariant following a doubling of the number of cells from 100 to 200. Similarly the $kr_0 = 0.1$ and $kr_0 = 10$ results of table 4.1 and figure 4.7 were found to be invariant under this reduction in cell size/time step. Thus the code is seen to be free of any significant truncation error.

A more stringent test of the code is the high temperature limit, $t >> 1$. As noted in chapters one and three the equilibrium is changing slowly in this regime and therefore ideal MHD should be valid at late times. Unfortunately ideal MHD is an *adiabatic* theory whereas the model described above is *isothermal*. However, if the $\Gamma = 1$ limit is taken in both theories then the ideal MHD perturbed temperature is identically zero, and therefore uniform, and in this case the results of the two codes should agree. They do: the variables in the code grow exponentially with an instantaneous growth rate that agrees to within 0.5% with the ideal MHD growth rate deduced from the shooting code (chapter one). The eigenfunctions produced from the two codes are difficult to distinguish by eye.

This is an appropriate place to reiterate the point made in section 3.3 concerning the difference in ($\Gamma = 5/3$) growth rates between the adiabatic and the isothermal models. Table 4.1 shows the two growth rates for values of kr_0 between 0.1 and 10. The maximum difference is less than 4% over the entire wavelength range, confirming the hypothesis that the distribution of the perturbed temperature has very little effect on the stability of the pinch in the ideal regime.

The acid test of the code is the reproducibility of its results. Section 4.6 contains a comparison of the results of this code with the corresponding results

kr_o	0.1	0.3	1.0	3.0	10.0
$\hat{\gamma}$ (adiabatic)	0.146	0.429	1.238	2.481	4.521
$\hat{\gamma}$ (isothermal)	0.146	0.435	1.266	2.570	4.616

Table 4.1 Normalised instantaneous m = 0 growth rate as a function of kr_o in adiabatic (ideal MHD) and isothermal (section 4.2) approximations.

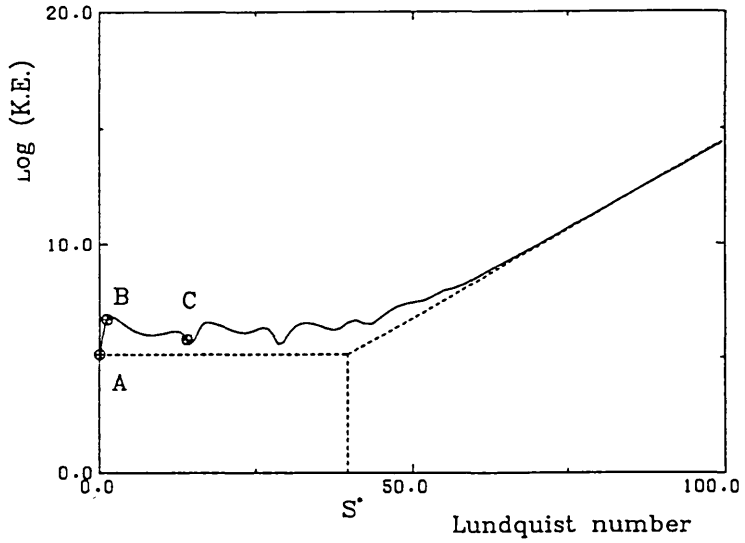


Figure 4.1 Perturbed kinetic energy against Lundquist number ($\propto t^{4/3}$) for m = 0, kr_o = 1 orthogonal initial perturbation.

of a two-dimensional non-linear code written by F. L. Cochran at the Naval Research Laboratory, Washington DC, USA. There it is shown that, despite the differences in approach, the results of the two codes are in good agreement, confirming the integrity of both.

4.5 Results

A convenient measure of the 'amplitude' of a perturbation is given by the perturbed kinetic energy

$$\text{K.E.} = 1/2 \int m_i n^0 \underline{v}^2 d^3r. \qquad (4.40)$$

Figure 4.1 is a graph of the (logarithm of the) kinetic energy of a $kr_0 = 1$ perturbation versus the Lundquist number (eqn. 1.29) which is proportional to $t^{4/3}$ for the equilibrium considered here, i.e. figure 4.1 is essentially a graph of the kinetic energy *history*. Two distinct regions are discernible. At early times the pinch is *stable*, the perturbed kinetic energy remaining approximately constant. At later times log(K.E.) is seen to be growing linearly with $S \propto t^{4/3}$. This can be identified with the exponentially growing ideal MHD instability since in MHD the growth rate γ_{mhd} is proportional to V_A/r_0, which is proportional to $t^{1/3}$ for this equilibrium. A WKB analysis (e.g Mathews and Walker 1970 p 27) shows that

$$\exp(\int_0^t \gamma(t')dt') = \exp(3/4\ \gamma(t)t) \qquad (4.41)$$

is an approximate solution of $d^2x/dt^2 = \gamma^2(t)x$ when γ is changing very slowly on the timescale γ^{-1} i.e. in the ideal MHD limit. [See later for a more detailed discussion of this point.] Thus, in this limit, the logarithm of a perturbed quantity varies linearly with $\gamma(t)t$ i.e. with $t^{4/3}$, and hence the linear part of figure 4.1 can be identified with the ideal MHD limit. The growth rate, normalised with respect to the *instantaneous* ion thermal transit time can be calculated from eqn. 4.41: this procedure produced the data for table 4.1.

The boundary between the stable and unstable regions of figure 4.1 can be described in terms of a *critical Lundquist number* S^*, the algorithm for calculating this quantity being defined by figure 4.1. [Explicitly: S^* is defined to be the position of the intersection between the initial value of the kinetic energy and the projection of the asymptotic linear part of the curve into the low Lundquist number regime.] Other diagnostics such as the perturbed temperature

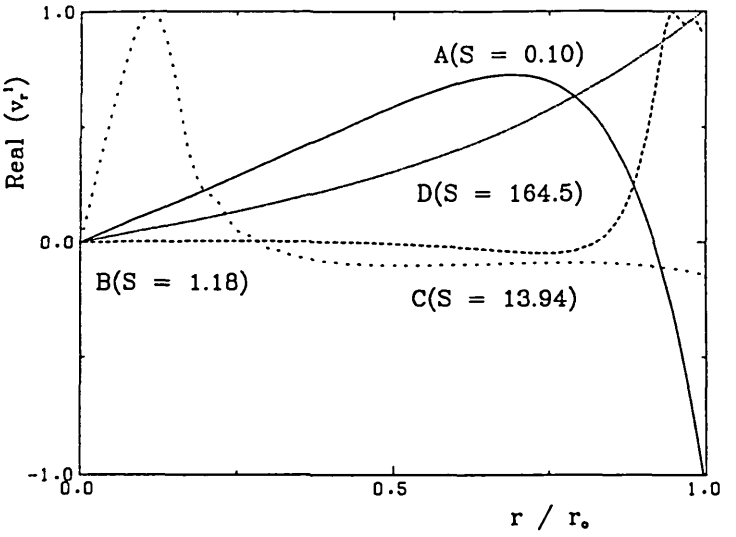


Figure 4.2 Profiles of perturbed radial velocity Re(v_r^1), normalised to a maximum value of unity, at times indicated in fig. 4.1 (m = 0, kr_o = 1).

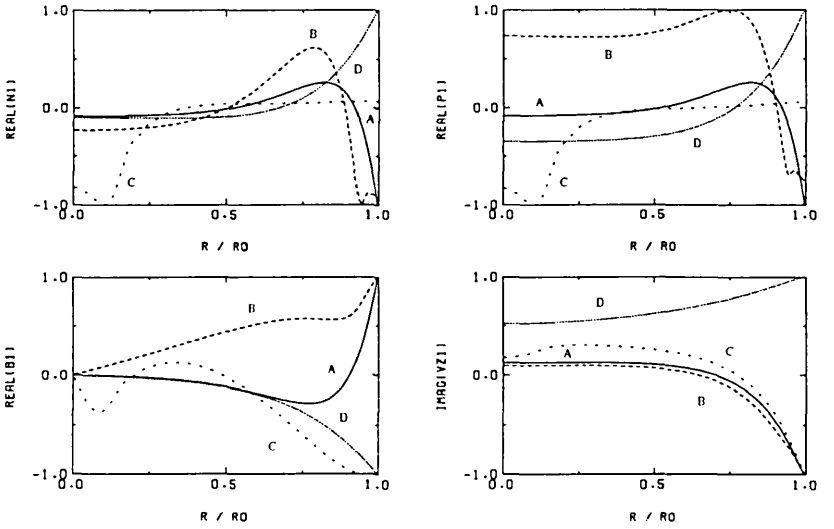


Figure 4.3 Profiles of Re(n^1), Re(p^1), Re(B_θ^1), and Im(v_z^1), normalised to maximum magnitudes of unity, at times indicated in fig. 4.1 (m = 0, kr_o = 1).

and the perturbed axial number density display the same period of stability before going exponentially unstable; in particular they define the same critical Lundquist number S^*. Notice that for the $kr_0 = 1$ modes of figure 4.1 S^* is approximately *40*, an order of magnitude greater than might at first be expected i.e. the pinch remains stable for *longer* than the intuitive estimate $S^* \simeq 1$ would suggest.

Figure 4.2 shows 'snapshots' of the perturbed radial velocity $Re(v_r^1)$ at the times indicated in figure 4.1; figure 4.3 gives snapshots of the other variables $Re(n^1)$, $Re(p^1)$, $Re(B_\theta^1)$, and $Im(v_z^1)$ at these times, all quantities being normalised to a maximum magnitude of unity. The evolution of the profiles from their initial forms, through the stable period in which they have no easily discernible structure until they converge to the ideal MHD eigenfunctions in the exponentially unstable regime is apparent.

The initial perturbation in the above case was the $\Gamma = 1$, $kr_0 = 1$ *second fastest growing MHD eigenfunction*, which is *automatically orthogonal* to the fastest growing mode (chapter one, section 1.3). Figure 4.4 displays the kinetic energy history which follows when the initial perturbation is given by the *fastest growing* $kr_0 = 1$ *mode*, i.e the mode which ultimately appears in the ideal MHD limit. As before, there is a period of stability at early times before the system goes exponentially unstable, although in this case the critical Lundquist number is less than the corresponding value for the 'orthogonal' perturbation of figure 4.1. Note that in this case the calculated value of S^* is conservative: judging figure 4.4 by eye it would probably be said that the pinch is stable until the last minimum of the kinetic energy curve at $S \simeq 17$, i.e. about 30% greater than the computed value.

Figures 4.5 and 4.6 are the corresponding versions for this 'parallel' perturbation of figures 4.2 and 4.3 for the 'orthogonal' perturbation. Again, the absence of any eigenfunction structure during the stable phase is clear. The slight discrepancy between the initial and final perturbations is not due to a lack of convergence: it is because the initial perturbation is defined by $\Gamma = 1$ (since this is the only case in which the ideal MHD perturbed temperature is uniform) whereas the code produces $\Gamma = 5/3$ eigenfunctions.

It has been shown that the period of stability $S < S^*$ is smaller for 'parallel' perturbations than for 'orthogonal' perturbations. Intuitively it might be expected that these two cases represent the smallest and largest possible values of S^* for *any* initial perturbation. Table 4.2 shows the values of S^* obtained from various

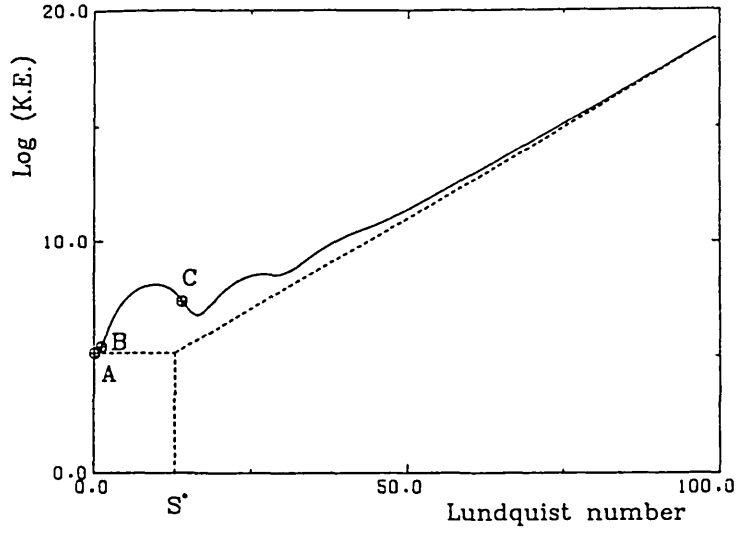


Figure 4.4 Perturbed kinetic energy against Lundquist number ($\propto t^{4/3}$) for m = 0, kr_o = 1 parallel initial perturbation.

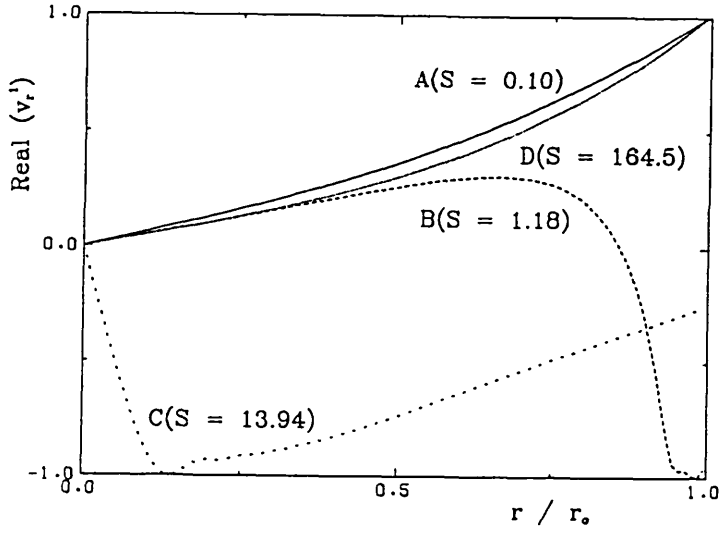


Figure 4.5 Profiles of perturbed radial velocity Re(v_r^1), normalised to a maximum value of unity, at times indicated in fig. 4.4 (m = 0, kr_o = 1).

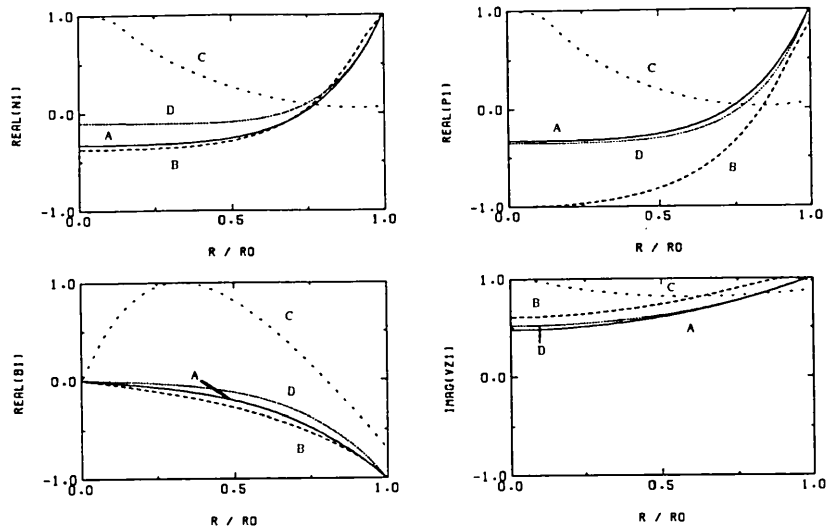


Figure 4.6 *Profiles of* $Re(n^1)$, $Re(p^1)$, $Re(B_\theta{}^1)$, *and* $Im(v_Z{}^1)$, *normalised to maximum magnitudes of unity, at times indicated in fig. 4.4* ($m = 0$, $kr_o = 1$).

Initial perturbation	$\hat{\gamma}$	S^*
Fastest growing	1.726	13
2nd fastest growing	0.352	40
3rd fastest growing	0.216	37
Stable	1.965 i	38
Random in 'r'	——	15

Table 4.2 *Variation of critical Lundquist number* S^* *with the form of the initial perturbation* ($m = 0$, $kr_o = 1$).

initial perturbations (all for $kr_o = 1$): the first, second, and third fastest growing ideal MHD modes, a *stable* ideal MHD mode (i.e. one with $\gamma^2 < 0$), and a perturbation defined randomly across the pinch radius. As expected, the first two *do* appear to give lower and upper bounds on the values of S^* obtainable from any initial perturbation.

The above work was performed with $kr_o = 1$ perturbations. Qualitatively similar results are obtained for perturbations of other wavelengths. Figure 4.7 shows the values of S^* for parallel and orthogonal perturbations as a function of kr_o over the range $0.1 < kr_o < 10$. A least-squares fit to the empirical data shows that

$$S^*(\text{parallel}) \simeq 25\ (kr_o)^{-1.1} \tag{4.42}$$

and

$$S^*(\text{orthogonal}) \simeq 73\ (kr_o)^{-0.82} \tag{4.43}$$

and that the arithmetic mean of the two, $\langle S^* \rangle$, has the approximate dependence

$$\langle S^* \rangle \simeq 50\ (kr_o)^{-0.86}. \tag{4.44}$$

Re-expressing this in terms of the normalised ideal MHD growth rate $\hat{\gamma}$ leads to

$$\langle S^* \rangle \simeq 65\ (\hat{\gamma})^{-1.2}. \tag{4.45}$$

4.6 Discussion and conclusions

In this chapter the development of axisymmetric perturbations in a time-dependent equilibrium has been studied using a one-dimensional linearised resistive initial-value code. The necessity of an initial-value rather than an eigenvalue approach has been emphasised.

The code has been successfully tested for numerical stability and accuracy, and in the high temperature, $\Gamma = 1$, limit it has been shown to agree with the results of ideal MHD theory obtained using a semi-analytical model (the shooting code).

It has been shown that there is a period of gross stability at low temperatures before the pinch develops exponential instabilities as it enters the

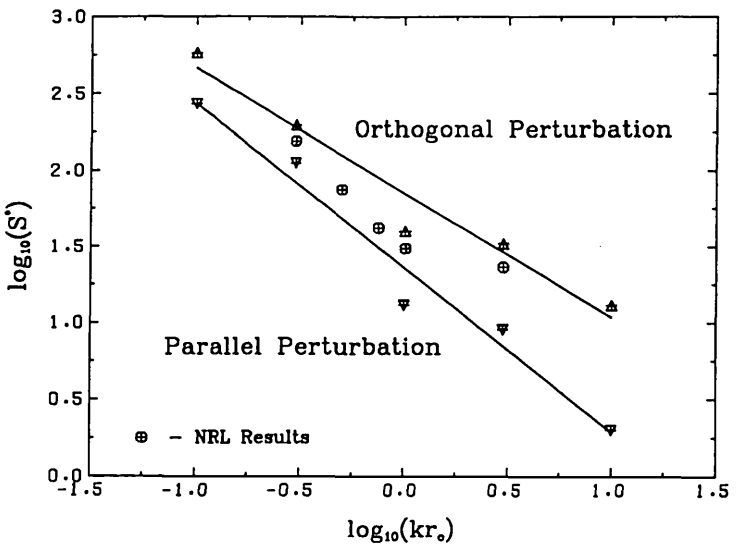


Figure 4.7 Critical Lundquist number S^* versus kr_o for $m = 0$ 'parallel' and 'orthogonal' initial perturbations. Cochran and Robson's 1989 NRL results also shown.

ideal MHD regime. The threshold of stability of the pinch can be defined by a critical Lundquist number S^*, such that if S is less than S^* then the pinch is stable.

The ideal MHD growth rate γ_{mhd} is proportional to $t^{1/3}$ as has been said before. Thus, even if resistivity has *no effect* on the development of the perturbation in itself, there will still be a delay before the development of the instability simply due to the small value of the ideal MHD growth rate at early times. The following simple analytical model was developed in order to determine if this effect could account for the results 4.42 to 4.45.

The equation

$$d^2x/dt^2 = \gamma^2(t)\, x \qquad (4.46)$$

subject to the boundary conditions

$$x(0) = 0; \quad dx/dt\ (0) = 1. \qquad (4.47)$$

can be considered to be a very simple ('zero−dimensional') model of the development of an instability 'x' with an instantaneous growth rate $\gamma(t)$ (c.f. the ideal MHD force equation 1.9, in which $\underline{F}$ depends on time). Setting

$$\gamma(t) = c\, t^{1/3} \qquad (4.48)$$

for some constant 'c' ($\propto \hat{\gamma}$) then makes the model appropriate for the equilibrium considered here. The solution of eqns. 4.46 and 4.48 subject to 4.47 is

$$x(t) = A\, c^{-3/8}\, t^{1/2}\, I_{3/8}(3ct^{4/3}/4) \qquad (4.49)$$

where $A = (3/8)^{-3/8}\, \Gamma(11/8)$, $I_{3/8}$ is a modified Bessel function of the first kind, and Γ is the gamma function. Asymptotically, at $t \to \infty$, eqn. 4.49 becomes

$$x(t) \simeq (3\pi/2)^{-1/2}\, A\, c^{-7/8}\, t^{-1/6} \exp(3ct^{4/3}/4) \qquad (4.50)$$

so that

$$dx(t)/dt \simeq (3\pi/2)^{-1/2}\, A\, (ct^{4/3})^{1/8} \exp(3ct^{4/3}/4). \qquad (4.51)$$

[This explains why the logarithm of a perturbed quantity varies linearly with $t^{4/3}$ in the ideal regime: c.f. the discussion following eqn. 4.41.] The kinetic energy,

$1/2\ (dx/dt)^2$ of the function x(t) defined by eqn. 4.49 has a broadly similar shape to the kinetic energy histories of figures 4.1 and 4.4. In particular, it has a 'kink', separating the 'flat' portion of the curve from the linearly increasing part. This kink can be used to define a threshold of stability as in the case of the results of the code. By equating the asymptotic form of the kinetic energy (from eqn. 4.51) to its initial value (=1/2) it can be seen that the position of the kink is defined by some critical value of $ct^{4/3}$, of the order of unity. Remembering that the Lundquist number $S \sim \tau_{ohm}/\tau_{mhd} \sim t/(r_o/V_A)$ (eqns. 1.31 to 1.33), and that the normalised growth rate $\hat{\gamma} = \gamma_{mhd}(t)\tau_{mhd}(t)$, it can be seen that in this simple model

$$(ct^{4/3})^* = \gamma_{mhd}(t^*)t^* = \hat{\gamma}\, t^*/\tau_{mhd}(t^*) \sim \hat{\gamma}\, S^* \sim 1 \qquad (4.52)$$

i.e. that

$$S^* \sim 1\ \hat{\gamma}^{-1}. \qquad (4.53)$$

The agreement of the scaling $S^* \propto (\hat{\gamma})^{-1}$ with the numerical result $S^* \propto (\hat{\gamma})^{-1.2}$ (equation 4.45) is remarkable. However, the proportionality constants (1 and 65 respectively) are very dissimilar. The conclusion of this analysis is therefore that the degree of stabilisation discovered numerically cannot be attributed to the small ideal MHD growth rates in the resistive phase – rather, it is the effect of resistivity on the *perturbation* (rather than on the *equilibrium*) that causes the stability in the resistive regime.

It has been shown that there is a significant difference (factor of about 3) between the values of S^* obtained for initial perturbations that are 'parallel' and 'orthogonal' to the perturbation which ultimately appears when the pinch goes unstable. Strong evidence has been given to suggest that these two cases give lower and upper bounds (respectively) on the value of S^* that could be obtained with *any* initial perturbation.

The variation of S^* with the wavelength of the perturbation has been investigated: the results are shown in figure 4.7. Also shown in this figure are the values of S^* calculated by Cochran and Robson (1989) at NRL, Washington DC using their two-dimensional non-linear code mentioned in section 4.4. As expected their results lie between the lower and upper bounds calculated in this analysis and their agreement in the trend of S^* with kr_o is very good.

Quantitatively the approximate law $S^* \simeq 50\ (kr_o)^{-0.86}$ has been derived. This indicates that for long wavelength modes (say $kr_o < 1$) the threshold of

instability is at least two orders of magnitude greater than might be naively expected (i.e. if $S^* \simeq 1$). This result offers a possible explanation of the enhanced stability observed in the fibre pinch experiments of Hammel and Scudder (1987) and Sethian *et. al.* (1987). Cochran and Robson (1989) have noted that the maximum Lundquist numbers appearing in these experiments are usually less than 50 and rarely exceed 200 (e.g. the point marked 'NRL' in figure 1.5 has a Lundquist number of 21, and the point marked 'LANL' has a Lundquist number of 32). The work of this chapter therefore offers a partial explanation of the enhanced stability of these pinches: they do not reach the unstable ideal MHD regime before the maximum of the current, and consequently they are stable during this period. It also follows from this result that because $S \propto r_0 I^4/N^2$ (eqn. 1.21) $\propto r_0 T^2$ (eqn. 1.18), smaller radius pinches can reach higher temperatures before going unstable.

In reality of course the pinch current does not vary as $t^{1/3}$: its profile is in fact approximately linear. Therefore the experimental fibre pinches are not in exact pressure balance, but are evolving under the action of the rising current. This seems unlikely, however, to have much effect on the stability of the pinches, since experimentally the pinch velocity is always found to be much less than the Alfven velocity, at least while the current is rising. A more serious failing of the analysis presented here is that the short wavelength modes are only slightly stabilised by resistivity ($S^* \propto (kr_0)^{-0.86}$) and that these modes are generally the most unstable anyway. An obvious response is that viscosity, an effect completely neglected here, has the largest effect on short wavelength modes. The hope is that by including resistivity and viscosity, both long wavelength and short wavelength modes would be stabilised, and that there would then be an intermediate wavelength with the worst possible stability characteristics. Stabilising this mode would then make the pinch unconditionally stable to an $m = 0$ perturbation of any wavelength.

Work is currently in progress on the inclusion of viscosity into the model presented in this chapter. The next chapter is concerned with a different generalisation of the model, namely the study of $m = 1$ modes. Since these modes have *never* been observed in the deuterium fibre pinch experiments, and since they do not possess significantly smaller ideal MHD growth rates, it is extremely interesting to study their development in the resistive regime.

CHAPTER FIVE

THE DEVELOPMENT OF HELICAL (M=1) INSTABILITIES IN THE RESISTIVE REGIME

5.1 Introduction

It was shown in the last chapter that an equilibrium Z-pinch could be stable to long wavelength axisymmetric (m = 0) perturbations provided that the Lundquist number was less than about 50. This chapter is concerned with the corresponding analysis for helical (m = 1) perturbations. This is a relatively straightforward generalisation of the linearised, Fourier-analysed model introduced in the last chapter, although the corresponding modification to a non-linear study - the increase in the dimensionality of the problem from two to three - would be considerably more difficult.

The approach of this chapter is very similar to that of chapter four. Section 5.2 contains a description of the equations and boundary conditions to be obeyed by the perturbed variables. Again the approximation of uniform equilibrium and perturbed temperatures is made. In section 5.3 the numerical scheme used to solve this set of equations is discussed, and in section 5.4 tests of the code are described. Section 5.5 discusses the results of the code and section 5.6 contains a discussion of the principal conclusions of this chapter.

5.2 Equations and boundary conditions

By an analagous approach to that of chapter four the general plasma equations 4.1 to 4.6 are linearised and Fourier analysed, the first order perturbed quantities being assumed to have the axial and azimuthal dependence $\exp(ikz - im\theta)$, in which m is equal to unity. In the equations of this chapter factors of 'm' will be retained (rather than replaced with unity) in order to distinguish those terms which arise from the angular dependence of the perturbation and which, therefore, are absent from the m = 0 analysis of chapter four. Viscosity and bremsstrahlung radiation are again neglected. The following equations are produced.

$$\partial n^1/\partial t = (-1/r)\partial(rn^0v_r^1)/\partial r + (imn^0v_\theta^1/r) - ikn^0v_z^1 \qquad (5.1)$$

$$m_i n^0 \partial v_r^1/\partial t = -j_z^0 B_\theta^1 - \partial p^1/\partial r - (B_\theta^0/\mu_o r)\partial(rB_\theta^1)/\partial r$$

$$- imB_\theta^0 B_r^1/\mu_o r \qquad (5.2)$$

$$m_i n^0 \partial v_\theta^1/\partial t = j_z^0 B_r^1 + imp^1/r \qquad (5.3)$$

$$m_i n^0 \partial v_z^1/\partial t = - ikp^1 - (iB_\theta^0/\mu_o r)(mB_z^1 + krB_\theta^1) \qquad (5.4)$$

$$\partial B_r^1/\partial t = - (im/r)(v_r^1 B_\theta^0 - \eta^1 j_z^0) + (2ik\eta^0 B_z^1/\mu_o r)$$

$$+ (\eta^0/\mu_o r^2)\{\partial(r\partial(rB_r^1)/\partial r)/\partial r - (m^2 + k^2r^2)B_r^1\} \qquad (5.5)$$

$$\partial B_\theta^1/\partial t = - ikv_z^1 B_\theta^0 - \partial(v_r^1 B_\theta^0)\partial r - mk\eta^0 B_z^1/\mu_o r + \eta^1 \partial j_z^0/\partial r$$

$$+ (im\eta^0/\mu_o)\partial(B_r^1/r)/\partial r - \eta^0 k^2 B_\theta^1/\mu_o$$

$$+ (\eta^0/\mu_o)(\partial(1/r\ \partial(rB_\theta^1)/\partial r)/\partial r) \qquad (5.6)$$

$$\partial B_z^1/\partial t = - imv_z^1 B_\theta^0/r - (\eta^0/\mu_o r^2)(m^2 + k^2r^2)B_z^1$$

$$+ (\eta^0/\mu_o r)(\partial(r\partial B_z^1/\partial r)/\partial r) \qquad (5.7)$$

$$dT^1/dt = (1/N)\int_0^{r_0}((\Gamma-1)/2k_B)\{\eta^1 j_z^0 j_z^0 + 2\eta^0 j_z^0 j_z^1$$

$$- p^0[1/r\partial(rv_r^1)/\partial r - imv_\theta^1/r + ikv_z^1]\} - n^1 dT^0/dt \quad 2\pi r dr \qquad (5.8)$$

where N is the pinch line density

$$\mu_o j_z^1 = 1/r\ \partial(rB_\theta^1)/\partial r + imB_r^1/r \qquad (5.9)$$

$$\eta^1/\eta^0 = (-3/2)\ T^1/T^0 \qquad (5.10)$$

$$p^1/p^0 = n^1/n^0 + T^1/T^0 \qquad (5.11)$$

Equations 5.5 to 5.7 are obtained by linearising

$$\partial \underline{B}/\partial t = \nabla \wedge (\underline{v} \wedge \underline{B} - \eta \underline{j}) \qquad (5.12)$$

together with the application of the 'solenoidal' condition

$$\nabla \cdot \underline{B} = 0 \qquad (5.13)$$

which eqn. 5.12 implies. The equations are written in this form in order to simplify their discretisation (section 5.3).

The boundary condition is given by the continuity of the total perturbed pressure across the perturbed boundary (chapters one and three). The result is (eqn. 3.12 after using eqn. 3.8 to eliminate $\xi_r(r_o^-)$)

$$p^1 + (B_\theta^0/\mu_o)(B_\theta^1 + im\chi B_r^1) = 0 \qquad (5.14)$$

at $r = r_o$, where the constant χ is defined by

$$\chi = K_m(kr_o)/kr_oK_m'(kr_o) < 0. \qquad (5.15)$$

This boundary condition, derived in the ideal MHD limit, is still valid in the resistive regime since its derivation only requires the equation of motion and Ampere's law, equations that are unmodified by the inclusion of resistivity.

It is also necessary to ensure that the right hand sides of eqns. 5.2 to 5.4 vanish at the plasma edge $r = r_o$ where the equilibrium density n^0 vanishes.

The equilibrium variables are the same as those used in chapter four (eqns. 4.7 to 4.11) i.e. the infinite thermal conductivity $\Omega = \Omega_{crit}$ solutions of section 2.2.(iii).

The continuity equation and the equations of motion are solved in a leap−frog manner, the energy equation by first order Euler integration and the diffusion of the magnetic field is solved as implicitly as possible.

5.3 Details of the numerical scheme

The normalisation described in section 4.3 is also valid for $m = 1$ modes which shows that the results of the numerical scheme are 'universal' in the same sense as in chapter four.

The computational mesh is again defined as NC (typically 100) equally separated radial cells. Equations 5.1 to 5.11 are differenced most easily if v_r^1 and B_r^1 are defined at the cell *boundaries* (subscript i+1/2: 1/2 → NC+1/2) while the other variables are defined at the cell *centres* (subcript i: 1 → NC). v_r^1, v_θ^1, and v_z^1 are defined at the half timesteps (superscript m+1/2) while the other variables are defined at integer timesteps (superscript m). T^1 and η^1 are both defined at times $m\Delta t$ and $(m+1/2)\Delta t$, and both are uniform across the radius of the pinch. The equilibrium variables are defined at the cell boundaries and the cell centres, and can be evaluated at all times. n^0 does not depend on time because there is no zeroth order velocity.

The equations describing the evolution of the perturbed variables, in the order in which they are solved, are as follows (boundary conditions to follow later):

$$n^0_i \frac{v^{1\ m+1/2}_{\theta\ i} - v^{1\ m-1/2}_{\theta\ i}}{\Delta t} = \frac{imp^{1\,m}_i}{r_i} + j^{0\ m}_{z\ i} \frac{B^{1\ m}_{r\ i+1/2} + B^{1\ m}_{r\ i-1/2}}{2} \qquad (5.16)$$

$$n^0_{i+1/2} \frac{v^{1\ m+1/2}_{r\ i+1/2} - v^{1\ m-1/2}_{r\ i+1/2}}{\Delta t} = -im \frac{B^{0\ m}_{\theta\ i+1/2} B^{1\ m}_{r\ i+1/2}}{r_{i+1/2}} - \frac{p^{1\ m}_{i+1} - p^{1\ m}_i}{\Delta r} - j^{0\ m}_{z\ i+1/2} \frac{B^{1\ m}_{\theta\ i+1} + B^{1\ m}_{\theta\ i}}{2} - B^{0\ m}_{\theta\ i+1/2} \frac{r_{i+1} B^{1\ m}_{\theta\ i+1} - r_i B^{1\ m}_{\theta\ i}}{r_{i+1/2}\Delta r} \qquad (5.17)$$

$$n^0_i \frac{v^{1\ m+1/2}_{z\ i} - v^{1\ m-1/2}_{z\ i}}{\Delta t} = -ikp^{1\ m}_i - ikB^{0\ m}_{\theta\ i} \left(B^{1\ m}_{\theta\ i} + \frac{m}{kr_i} B^{1\ m}_{z\ i}\right) \qquad (5.18)$$

$$\frac{n^{1\ m+1}_{\ i} - n^{1\ m}_{\ i}}{\Delta t} = - ikn^{0}_{\ i}\, v^{1\ m+1/2}_{z\ i} + imn^{0}\, \frac{v^{1\ m+1/2}_{\theta\ i}}{r_i}$$

$$- \frac{r_{i+1/2} n^{0}_{\ i+1/2}\, v^{1\ m+1/2}_{r\ i+1/2} - r_{i-1/2} n^{0}_{\ i-1/2} v^{1\ m+1/2}_{r\ i-1/2}}{r_i \Delta r} \qquad (5.19)$$

$$\frac{T^{1\ m+1/2} - T^{1\ m-1/2}}{\Delta t} = \frac{1}{N} \sum_{i=1}^{NC} (\Gamma-1)\{\eta^{1\ m}\, j^{0\ m}_{z\ i}\, j^{0\ m}_{z\ i} + 2\eta^{0\ m} j^{0\ m}_{z\ i} j^{1\ m}_{z\ i}$$

$$- p^{0\ m+1/2}_{\ i}\left(\frac{r_{i+1/2} v^{1\ m+1/2}_{r\ i+1/2} - r_{i-1/2} v^{1\ m+1/2}_{r\ i-1/2}}{r_i \Delta r} - im\, \frac{v^{1\ m+1/2}_{\theta\ i}}{r_i} + ikv^{1\ m+1/2}_{z\ i}\right)\}$$

$$- \frac{2n^{1\ m}_{i}\, T^{0\ m}}{3\ t^{m}} \cdot 2\pi r_i \Delta r \qquad (5.20)$$

where $N = \sum_{i=1}^{NC} n^{0}_{\ i}\, 2\pi r_i \Delta r$ is the pinch line density (5.21)

and $$j^{1\ m}_{z\ i} = \frac{r_{i+1/2}(B^{1\ m}_{\theta\ i+1} + B^{1\ m}_{\theta\ i}) - r_{i-1/2}(B^{1\ m}_{\theta\ i} + B^{1\ m}_{\theta\ i-1})}{2r_i \Delta r}$$

$$+ im\, \frac{B^{1\ m}_{r\ i+1/2} + B^{1\ m}_{r\ i-1/2}}{2r_i} . \qquad (5.22)$$

$$\frac{\eta^{1\ m+1/2}}{\eta^{0\ m+1/2}} = - \frac{3\ T^{1\ m+1/2}}{2\ T^{0\ m+1/2}} \qquad (5.23)$$

$$\frac{B^{1\ m+1}_{z\ i} - B^{1\ m}_{z\ i}}{\Delta t} = - im\, \frac{v^{1\ m+1/2}_{z\ i}\, B^{0\ m+1/2}_{\theta\ i}}{r_i}$$

$$- \eta^{0\ m+1}(m^2 + k^2 r_i^2)\, \frac{B^{1\ m+1}_{z\ i}}{r_i^2} + \frac{\eta^{0\ m+1}}{r_i\ (\Delta r)^2} \times$$

$$\{r_{i+1/2}(B^{1\ m+1}_{z\ i+1} - B^{1\ m+1}_{z\ i}) - r_{i-1/2}(B^{1\ m+1}_{z\ i} - B^{1\ m+1}_{z\ i-1})\} \qquad (5.24)$$

$$\frac{B_{r\ i+1/2}^{1\ m+1} - B_{r\ i+1/2}^{1\ m}}{\Delta t} = ik\eta^{0\ m+1} \frac{B_{z\ i+1}^{1\ m+1} + B_{z\ i}^{1\ m+1}}{r_{i+1/2}}$$

$$- \frac{im}{r_i} (v_{r\ i+1/2}^{1\ m+1/2} B_{\theta\ i+1/2}^{0\ m+1/2} - \eta^{1\ m+1/2} j_{z\ i+1/2}^{0\ m+1/2}) + \frac{\eta^{0\ m+1}}{r_i^2 (\Delta r)^2} \times$$

$$\{r_{i+1}(r_{i+3/2} B_{r\ i+3/2}^{1\ m+1} - r_{i+1/2} B_{r\ i+1/2}^{1\ m+1})$$

$$- r_i (r_{i+1/2} B_{r\ i+1/2}^{1\ m+1} - r_{i-1/2} B_{r\ i-1/2}^{1\ m+1})\}$$

$$- \frac{\eta^{0\ m+1}}{r_{i+1/2}^2} (m^2 + k^2 r_{i+1/2}^2) B_{r\ i+1/2}^{1\ m+1} \qquad (5.25)$$

$$\frac{B_{\theta\ i}^{1\ m+1} - B_{\theta\ i}^{1\ m}}{\Delta t} = - ik\, v_{z\ i}^{1\ m+1/2} B_{\theta\ i}^{0\ m+1/2} - mk\eta^{0\ m+1} \frac{B_{z\ i}^{1\ m+1}}{r_i}$$

$$- \frac{v_{r\ i+1/2}^{1\ m+1/2} B_{\theta\ i+1/2}^{0\ m+1/2} - v_{r\ i-1/2}^{1\ m+1/2} B_{\theta\ i-1/2}^{0\ m+1/2}}{\Delta r}$$

$$- \frac{\eta^{1\ m+1/2} j_{z\ i+1/2}^{0\ m+1/2} - \eta^{1\ m+1/2} j_{z\ i-1/2}^{0\ m+1/2}}{\Delta r}$$

$$+ \frac{im\eta^{0\ m+1}}{\Delta r} \left(\frac{B_{r\ i+1/2}^{1\ m+1}}{r_{i+1/2}} - \frac{B_{r\ i-1/2}^{1\ m+1}}{r_{i-1/2}}\right) - \eta^{0\ m+1} k^2 B_{\theta\ i}^{1\ m+1}$$

$$+ \frac{\eta^{0\ m+1}}{(\Delta r)^2} \left(\frac{r_{i+1} B_{\theta\ i+1}^{1\ m+1} - r_i B_{\theta\ i}^{1\ m+1}}{r_{i+1/2}} - \frac{r_i B_{\theta\ i}^{1\ m+1} - r_{i-1} B_{\theta\ i-1}^{1\ m+1}}{r_{i-1/2}}\right) \qquad (5.26)$$

$$\frac{T^{1\ m+1} - T^{1\ m}}{\Delta t} = \frac{1}{N} \sum_{i=1}^{NC} (\Gamma-1)\{\eta^{1\ m+1/2} j_{z\ i}^{0\ m+1/2} j_{z\ i}^{0\ m+1/2}$$

$$+ 2\eta^{0\ m+1/2} j_{z\ i}^{0\ m+1/2} j_{z\ i}^{1\ m+1}$$

$$- p_i^{0\ m+1/2} \left(\frac{r_{i+1/2} v_{r\ i+1/2}^{1\ m+1/2} - r_{i-1/2} v_{r\ i-1/2}^{1\ m+1/2}}{r_i \Delta r} - im \frac{v_{\theta\ i}^{1\ m+1/2}}{r_i} + ikv_{z\ i}^{1\ m+1/2}\right)\}$$

$$- \frac{2n^{1\ m+1}_{i}\ T^{0\ m+1}}{3\ t^{m+1}} \cdot 2\pi r_i \Delta r \qquad (5.27)$$

where $j^{1\ m+1}_{z\ i} = \dfrac{r_{i+1/2}(B^{1\ m+1}_{\theta\ i+1} + B^{1\ m+1}_{\theta\ i}) - r_{i-1/2}(B^{1\ m+1}_{\theta\ i} + B^{1\ m+1}_{\theta\ i-1})}{2r_i \Delta r}$

$$+ \text{im} \frac{B^{1\ m+1}_{r\ i+1/2} + B^{1\ m+1}_{r\ i-1/2}}{2r_i} . \qquad (5.28)$$

$$\frac{\eta^{1\ m+1}}{\eta^{0\ m+1}} = - \frac{3\ T^{1\ m+1}}{2\ T^{0\ m+1}} \qquad (5.29)$$

$$\frac{p^{1\ m+1}_{i}}{p^{0\ m+1}_{i}} = \frac{n^{1\ m+1}_{i}}{n^{0\ m+1}_{i}} + \frac{T^{1\ m+1}}{T^{0\ m+1}} \qquad (5.30)$$

The boundary conditions at the axis are:

$$v_{\theta}{}^{1}{}_{1}{}^{m+1/2} = 2v_{\theta}{}^{1}{}_{2}{}^{m+1/2} - v_{\theta}{}^{1}{}_{3}{}^{m+1/2} \qquad (5.31)$$

$$v_{r}{}^{1}{}_{1/2}{}^{m+1/2} = 2v_{r}{}^{1}{}_{3/2}{}^{m+1/2} - v_{r}{}^{1}{}_{5/2}{}^{m+1/2} \qquad (5.32)$$

$$v_{z}{}^{1}{}_{1}{}^{m+1/2} = (1/3)v_{z}{}^{1}{}_{2}{}^{m+1/2} \qquad (5.33)$$

$$n^{1}{}_{1}{}^{m+1} = 2n^{1}{}_{2}{}^{m+1} - n^{1}{}_{3}{}^{m+} \qquad (5.34)$$

$$B_{z}{}^{1}{}_{1}{}^{m+1} = (1/3)B_{z}{}^{1}{}_{2}{}^{m+1} \qquad (5.35)$$

$$B_{r}{}^{1}{}_{1}{}^{m+1} = B_{r}{}^{1}{}_{2}{}^{m+1} \qquad (5.36)$$

$$B_{\theta}{}^{1}{}_{1}{}^{m+1} = B_{\theta}{}^{1}{}_{2}{}^{m+1} \qquad (5.37)$$

$$p^{1}{}_{1}{}^{m+1} = (1/3)\ p^{1}{}_{2}{}^{m+1} \qquad (5.38)$$

An expansion of the variables as power series in r, valid close to r = 0, followed by a substitution of those expansions into equations 5.1 to 5.11 shows that $v_z{}^1$, $B_z{}^1$, and p^1 vanish at r = 0, giving eqns. 5.33, 5.35, and 5.38, and that $B_r{}^1$

and $B_\theta{}^1$ are 'flat' (i.e. their radial derivatives vanish) at r = 0 which gives boundary conditions 5.36 and 5.37. The other conditions, linear extrapolations from the values inside pinch, are found empirically to produce well behaved solutions, with none of the variables diverging at the axis.

At the edge of the pinch, $r = r_o$, the boundary conditions are:

$$v_\theta{}^1{}_{NC}{}^{m+1/2} = 2v_\theta{}^1{}_{NC-1}{}^{m+1/2} - v_\theta{}^1{}_{NC-2}{}^{m+1/2} \qquad (5.39)$$

$$v_r{}^1{}_{NC+1/2}{}^{m+1/2} = 2v_r{}^1{}_{NC-1/2}{}^{m+1/2} - v_r{}^1{}_{NC-3/2}{}^{m+1/2} \qquad (5.40)$$

$$v_z{}^1{}_{NC}{}^{m+1/2} = 2v_z{}^1{}_{NC-1}{}^{m+1/2} - v_z{}^1{}_{NC-2}{}^{m+1/2} \qquad (5.41)$$

$n^1{}_{NC}{}^{m+1}$ defined by eqn. 5.19 by putting i = NC (5.42)

$$mj_z{}^0{}_{NC}{}^{m+1}B_z{}^1{}_{NC}{}^{m+1} - k\chi\breve{p}^1{}_{NC}{}^{m+1} =$$

$$(1/3)[mj_z{}^0{}_{NC-1}{}^{m+1}B_z{}^1{}_{NC-1}{}^{m+1} - k\chi\breve{p}^1{}_{NC-1}{}^{m+1}] \qquad (5.43)$$

$$B_r{}^1{}_{NC+1/2}{}^{m+1} =$$

$$(-i/k\chi)[(3B_z{}^1{}_{NC}{}^{m+1}/2r_{NC}) - (B_z{}^1{}_{NC-1}{}^{m+1}/2r_{NC-1})] \qquad (5.44)$$

$$(3/2)[\breve{p}^1{}_{NC}{}^{m+1} + B_\theta{}^0{}_{NC}{}^{m+1}B_\theta{}^1{}_{NC}{}^{m+1}] -$$

$$(1/2)[\breve{p}^1{}_{NC-1}{}^{m+1} + B_\theta{}^0{}_{NC-1}{}^{m+1}B_\theta{}^1{}_{NC-1}{}^{m+1}] =$$

$$- im\chi B_r{}^1{}_{NC+1/2}{}^{m+1}B_\theta{}^0{}_{NC+1/2}{}^{m+1} \qquad (5.45)$$

$p^1{}_{NC}{}^{m+1}$ defined by eqn. 5.30 by putting i = NC (5.46)

Equations 5.39 to 5.41 are found empirically to produce well behaved solutions. Eqns. 5.42 and 5.46 require no comment. Equations 5.43, 5.44, and 5.45 are obtained by combining the pressure balance condition 5.14 with the conditions

$$p^1 + B_\theta{}^0(B_\theta{}^1 + (m/kr)B_z{}^1) = 0 \qquad (5.47)$$

and

$$p^1 - imrj_z{}^0B_r{}^1 = 0 \qquad (5.48)$$

at $r = r_o$, which come from the finiteness of v_z^1 and v_θ^1 at the boundary respectively (see eqns. 5.4 and 5.3). Eqns. 5.14, 5.47, and 5.48 lead to the conditions (at $r = r_o$):

$$mj_z{}^0B_z{}^1 - k\chi p^1 = 0 \qquad (5.49)$$

$$B_r{}^1 + (iB_z{}^1/kr\chi) = 0 \qquad (5.50)$$

and $$p^1 + B_\theta{}^0B_\theta{}^1 + im\chi B_\theta{}^0B_r{}^1 = 0, \qquad (5.51)$$

for which eqns. 5.43 to 5.45 are finite difference expressions. The quantities $\breve{p}^1{}_{NC}{}^{m+1}$ and $\breve{p}^1{}_{NC-1}{}^{m+1}$ which appear in these equations are estimates for the perturbed pressure at timestep m+1, the true pressure not being calculated until after the magnetic fields and temperature have been advanced to this time. $\breve{p}$ is therefore defined through equation 5.30 in which the temperature at time m+1, $T^{1\ m+1}$, is approximated according to the rule

$$\breve{T}^{1\ m+1} \simeq (3/2)\ T^{1\ m+1/2} - (1/2)\ T^{1\ m-1/2}. \qquad (5.52)$$

This procedure, while not being ideal, does not lead to error in practice.

As in chapter four the timestep is given by the hybrid diffusion−CFL condition 4.39 in which the timestep multiplier λ is never taken to be larger than 0.1.

5.4 Tests of the numerical scheme

The results to be presented in table 5.1 and figures 5.1 to 5.6 remain the same following a reduction in cell size by a factor of two. This procedure automatically reduces the timestep by a factor of four during the resistive phase and a factor of two during the advective phase (eqn. 4.39). The invariance of the results shows that the code is free from any significant truncation errors.

In the high temperature $\Gamma = 1$ regime the code should reproduce the results of $\Gamma = 1$ ideal MHD for the reasons discussed in section 4.4. It does: growth rates obtained from the shooting code and from the code of this chapter agree to within 1% and the eigenfunctions are indistinguishable to the eye.

As in the case of m = 0 modes it is valuable to compare the $\Gamma = 5/3$ results of the code with the $\Gamma = 5/3$ shooting code results. Table 5.1 gives the growth rates obtained from both codes for a range of wavelengths $0.1 < kr_0 < 10$. The maximum difference over this range is 12%, confirming the assertion made in chapter three that the distribution of the perturbed temperature has very little effect on the stability properties of a Z-pinch in the high temperature regime. This result was proved for m = 0 modes in chapter four; table 5.1 shows that the same is true for m = 1 modes.

5.5 Results

The amplitude of a perturbation is again measured by its kinetic energy (eqn. 4.40).

Figure 5.1 shows the kinetic energy history of a $kr_0 = 1$ mode. A period of stability is apparent, as is the exponential growth after a critical Lundquist number S^* is exceeded. Figures 5.2 and 5.3 display snapshots of $Re(n^1)$, $Re(v_r^1)$, $Im(v_\theta^1)$, $Im(v_z^1)$, $Re(p^1)$, $Im(B_r^1)$, $Re(B_\theta^1)$, and $Re(B_z^1)$, all normalised to a maximum magnitude of unity, at the instants indicated on figure 5.1. The evolution of the perturbation from its initial form (which in this case is the fastest growing $\Gamma = 1$, $kr_0 = 1$ ideal MHD mode i.e. the 'parallel' perturbation in the sense of section 4.5), through a complicated phase in which the pinch is stable, to the ideal MHD eigenfunction at late times is apparent.

Figures 5.4 to 5.6 are the corresponding versions of figures 5.1 to 5.3 for an initial perturbation that is 'orthogonal' to the final perturbation. For m = 1, $kr_0 = 1$ modes it is necessary to enter the *stable* side of the spectrum in order to find such a mode i.e. the initial perturbation of figures 5.4 to 5.6 is stable in ideal MHD theory ($\gamma^2 < 0$). [This is in contrast to the case of m = 0 modes where the presence of an accumulation point at $\gamma^2 = 0$ ensures the existence of an infinity of unstable eigenfunctions for all values of kr_0.] Nevertheless, this stable perturbation *does* become unstable in the ideal MHD limit, an effect not due to the necessarily imperfect numerical representation of the true stable solution since, as has been said before, S^* is invariant to a reduction in the cell size. As expected, S^* is larger for this perturbation than for the parallel perturbation of figs. 5.1 to 5.3.

In order to test the hypothesis that parallel and orthogonal initial

kr_o	0.1	0.3	1.0	3.0	10.0
$\hat{\gamma}$ (adiabatic)	0.254	0.531	1.014	1.549	2.964
$\hat{\gamma}$ (isothermal)	0.224	0.515	1.010	1.545	3.034

Table 5.1 Normalised instantaneous m = 1 growth rate as a function of kr_o in adiabatic (ideal MHD) and isothermal (section 5.2) approximations.

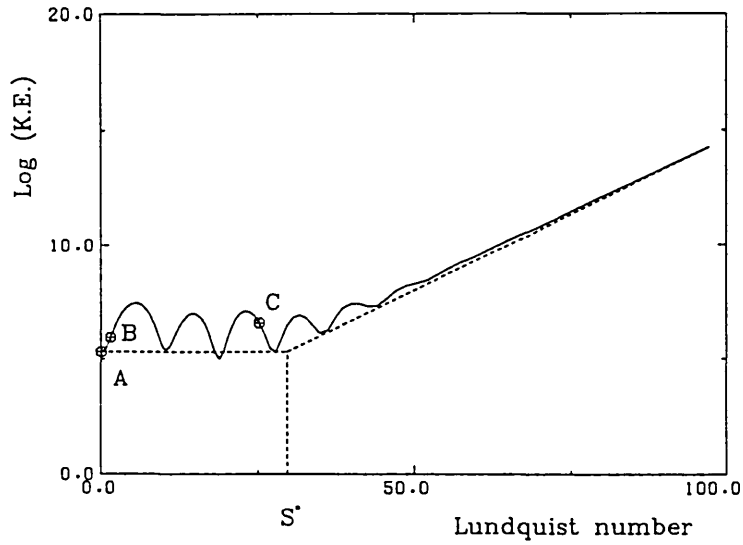


Figure 5.1 Perturbed kinetic energy against Lundquist number ($\propto t^{4/3}$) for m = 1, kr_o = 1 parallel initial perturbation.

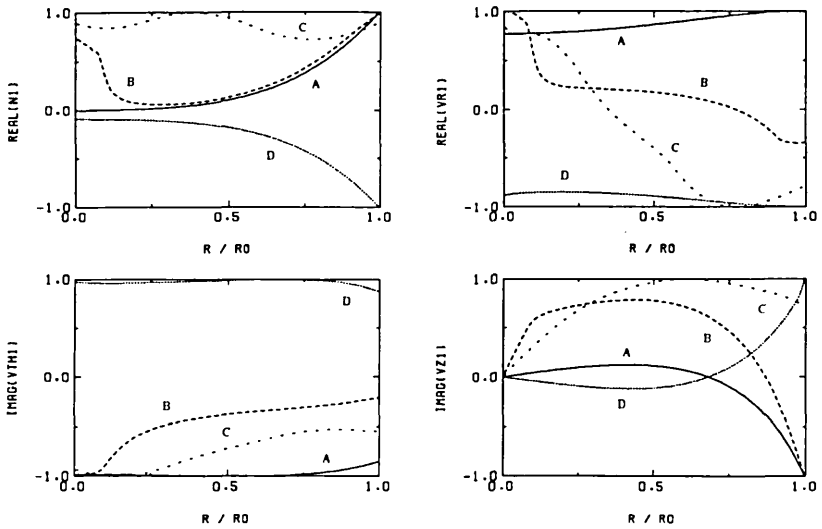


Figure 5.2 *Profiles of $Re(n^1)$, $Re(v_r{}^1)$, $Im(v_\theta{}^1)$, and $Im(v_z{}^1)$, normalised to a maximum value of unity, at times indicated in fig. 5.1 ($m = 1$, $kr_o = 1$). S(A) = 0.10, S(B) = 1.6, S(C) = 25, S(D) = 340.*

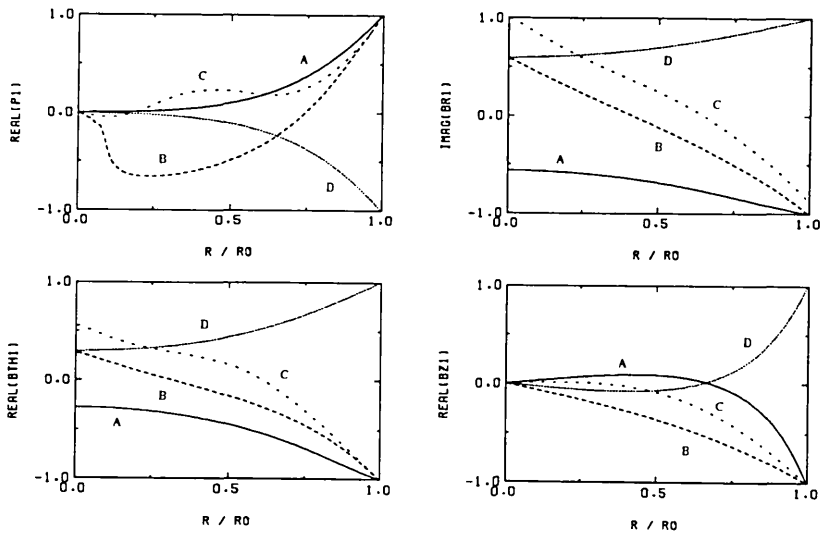


Figure 5.3 *Profiles of $Re(p^1)$, $Im(B_r{}^1)$, $Re(B_\theta{}^1)$, and $Re(B_z{}^1)$, normalised to maximum magnitudes of unity, at times indicated in fig. 5.1 ($m = 1$, $kr_o = 1$).*

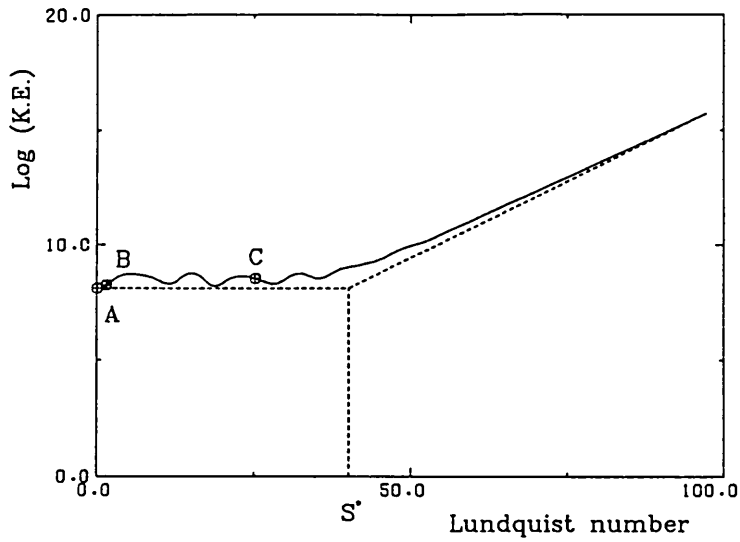


Figure 5.4 *Perturbed kinetic energy against Lundquist number ($\propto t^{4/3}$) for m = 1, kr_o = 1 orthogonal initial perturbation.*

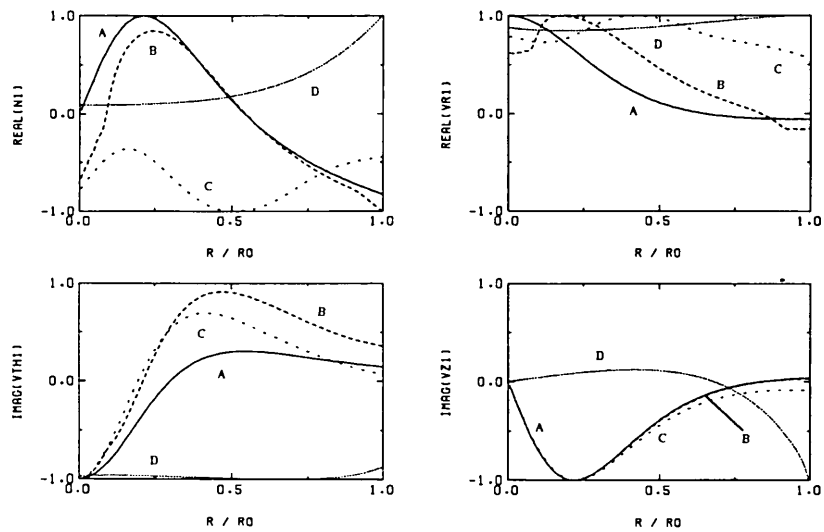


Figure 5.5 *Profiles of $Re(n^1)$, $Re(v_r{}^1)$, $Im(v_\theta{}^1)$, and $Im(v_z{}^1)$, normalised to a maximum value of unity, at times indicated in fig. 5.4 (m = 1, kr_o = 1). S(A) = 0.10, S(B) = 1.6, S(C) = 25, S(D) = 340.*

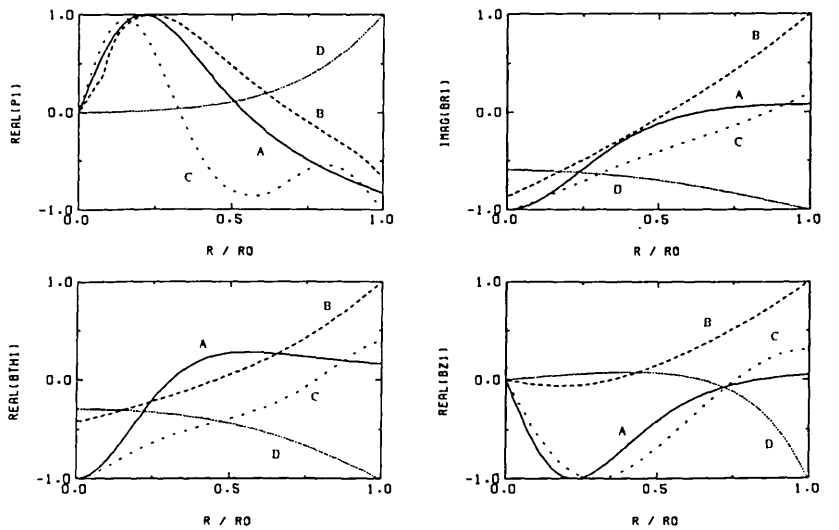


Figure 5.6 Profiles of $Re(p^1)$, $Im(B_r{}^1)$, $Re(B_\theta{}^1)$, and $Re(B_z{}^1)$, normalised to maximum magnitudes of unity, at times indicated in fig. 5.4 ($m = 1$, $kr_o = 1$).

Initial perturbation	$\hat{\gamma}$	S^*
Fastest growing	3.143	5
2nd fastest growing	1.234	12
3rd fastest growing	0.850	9
Stable	0.252 i	12
Random in 'r'	——	7

Table 5.2 Variation of critical Lundquist number S^* with the form of the initial perturbation ($m = 1$, $kr_o = 10$).

perturbations provide bounds on the value of S^* for any initial perturbation it is necessary to employ short wavelength modes, since long wavelength modes do not possess sufficiently many eigenfunctions. Table 5.2 gives the values of S^* for $kr_0 = 10$ modes found by using various initial perturbations: the fastest, second fastest, third fastest growing modes, a stable mode, and a random perturbation. As expected, the first of these has the smallest value of S^*, while the others (except the random perturbation) cluster around the same value, approximately twice the smallest value (c.f. table 4.2 in chapter four).

Figure 5.7 is a graph of S^*(parallel) and S^*(orthogonal) against kr_0. As for $m = 0$ modes the critical Lundquist number is found to vary inversely with kr_0, a least−squares fit to the data revealing that

$$S^*(\text{parallel}) \simeq 30\ (kr_0)^{-0.84}, \tag{5.53}$$

$$S^*(\text{orthogonal}) \simeq 49\ (kr_0)^{-0.70}, \tag{5.54}$$

and

$$\langle S^* \rangle \simeq 40\ (kr_0)^{-0.75} \tag{5.55}$$

where $\langle S^* \rangle$ is the arithmetic mean of the other two values.

5.6 Discussion and conclusions

In this chapter the development of helical ($m = 1$) perturbations in a time−dependent equilibrium has been studied using a one−dimensional linearised initial value code. The code has been succesfully tested with regard to truncation errors and in the ($\Gamma = 1$) ideal MHD limit.

There has been shown to be a period of stability, $S < S^*$, in which the pinch is found to be stable and after which the pinch succumbs to catastrophic ideal MHD instabilities. S^* has been shown to depend on the form of the initial perturbation and on the wavelength of that perturbation. The results are shown on figure 5.7.

Quantitatively the approximate law $\langle S^* \rangle \simeq 40\ (kr_0)^{-0.75}$ has been determined. This should be compared to the corresponding result for $m = 0$ modes, $\langle S^* \rangle \simeq 50\ (kr_0)^{-0.86}$ (equation 4.44). The agreement is interesting because it shows that each type of perturbation is stabilised to a similar degree

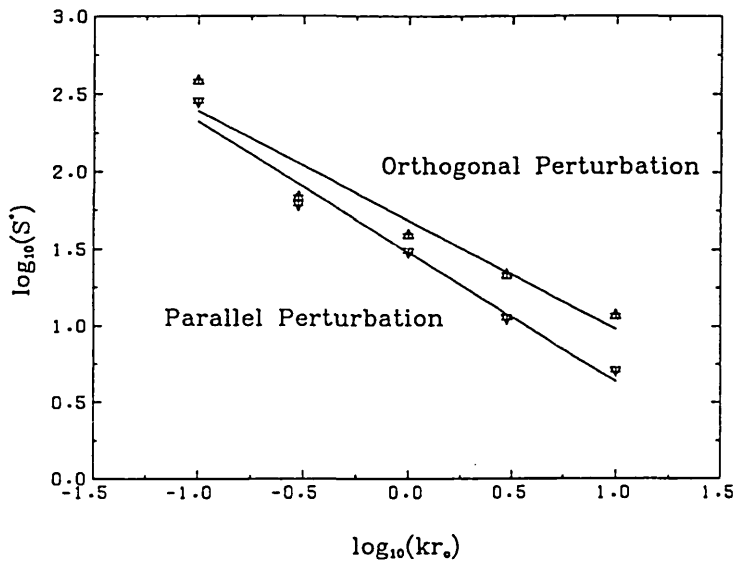


Figure 5.7 Critical Lundquist number S^* versus kr_o for m = 1 'parallel' and 'orthogonal' initial perturbations.

during the resistive phase. This is compatible with the experimental fact that fibre pinches are stable to both m = 0 and m = 1 perturbations while the current is rising. The development of m = 0 instabilities at peak current could not be explained by the work of the last chapter, since that analysis assumed that the equilibrium pinch was in pressure balance, an approximation that breaks down as soon as the current stops rising. For the same reason, the work of this chapter cannot explain the absence of m = 1 instabilities at peak current. The behaviour of the pinch after the current maximum can probably only be studied by accurate numerical simulation of the experimental situation, although the scaling of neutron yield with peak current, $Y \propto I_{max}{}^{10}$, has been explained analytically by McCall (1988).

The same analytical model as in chapter four, based on the equation $d^2x/dt^2 = \gamma^2(t)x$, indicates that the degree of stabilisation found numerically cannot be explained by the reduction in the MHD growth rate at early times, and must therefore be caused by the effect of resistivity directly on the perturbation.

The conclusion that m = 1 perturbations are not significantly more stabilised by resistivity than m = 0 modes indicates that Coppins' suggestion (Coppins 1988) concerning the Imperial College gas−embedded Z−pinch experiment − that it evolves into a Kadomtsev−stable equilibrium at an early time and then develops m = 1 instabilities − is probably correct, since the alternative theory that resistivity stabilises m = 0 modes while allowing m = 1 instabilities to develop is now untenable.

In summary, the work of this chapter shows that m = 1 perturbations are stabilised by resistivity and that, particularly for long wavelengths, the regime of stability is up to two orders of magnitude greater than might be expected intuitively (i.e. $S^* \simeq 100$ rather than 1). This result, and the corresponding version for m = 0 modes which was proved in chapter four, are the principal results of this thesis.

CHAPTER SIX

THE INVERSE SKIN EFFECT AND ITS OCCURRENCE IN THE COMPRESSIONAL PINCH

6.1 The inverse skin effect

It is well known that an alternating current flowing in a conductor can be concentrated near the conductor's surface provided that the current changes more rapidly than the resistive diffusion timescale of the conductor – this is the *skin effect* (see, for example, Stratton 1941 p 531). However, if a fully diffused current falls rapidly enough then it is possible that the current at the conductor's edge may be reduced or even reversed with respect to its value deep inside the conductor. This phenomenon was first studied (in the context of Z–pinches) by Haines (1959) who called it the *inverse skin effect*. A stationary Ohmically heated Z–pinch can only be held in pressure balance by a *rising* current (figure 1.6). Thus the inverse skin effect is associated with an expansion of the pinch. Haines postulated that if the current density is reversed at the plasma surface (causing a radially *outward* Lorentz force) then the outer region of the pinch may detach itself from the main body of plasma. Jones and Silawatshananai (1980) used holographic interferometry and streak photography to investigate a stabilised Z–pinch carrying a falling current. They observed an expansion of the pinch and the ejection of an outer layer of plasma after the surface current density reversed. They also found that the number density profiles were 'hollowed out' – that is, the peak density occurred off–axis.

This chapter presents a numerical study, using a single fluid one–dimensional Lagrangian code to be described in section 6.2, of the dynamics of a Z–pinch in which the total current is falling, and in which, therefore, the inverse skin effect can occur. In section 6.3 the basic properties of such a configuration are investigated by employing a current which falls linearly with time. Separation of part of the plasma is not found, although it is shown that a very dense narrow layer can arise near the plasma edge if the total current reverses. It is suggested that this phenomenon could easily be detected by the associated increase in bremsstrahlung emission from the plasma. In section 6.4 the code is used to model the falling current phase of the compressional pinch experiment at Imperial College (Haines *et. al.* 1988). An estimate is made of the maximum rate of

cooling consistent with the observed dynamical behaviour and in section 6.5 this is used to make a realistic assessment of the ideal magnetohydrodynamic stability of the pinch. On this basis the pinch would appear to show enhanced stability.

6.2 Lagrangian code modelling

A one-dimensional Lagrangian code, originally written by A. R. Bell and later modified by G. J. Rickard (private communications), is used to examine the nature of the inverse skin effect in the Z-pinch configuration. The code incorporates Spitzer resistivity and cross-field ion thermal conductivity appropriate to a fully ionised *hydrogen* (rather than deuterium) plasma with equal ion and electron temperatures (Braginskii 1965) but neglects all radiation losses. The pinch is initially assumed to be in an equilibrium state with uniform current density and temperature profiles and a parabolic number density distribution. Since in section 6.4 this code is used to model a particular experiment the relevant parameters of 4 mm radius and 2×10^{19} m^{-1} line density are used. The code is conservative in mass, energy, magnetic flux and momentum. The equations that it solves are the basic plasma equations 1.3, 1.4, 1.7, 1.8, 1.22, 1.23, and 1.24. Thermo-electric effects and end losses are neglected in the basic code (although in section 6.4 a simple estimate of the end losses is included) and therefore the heat flow $\underline{q}$ only has a radial component, $q_r = -\kappa_\perp^{(i)} \partial T/\partial r$, where $\kappa_\perp^{(i)}$ is the Spitzer cross-field ion thermal conductivity. An artificial viscosity pressure is introduced into the equation of motion 1.4 in order to damp out large amplitude, short wavelength oscillations associated with shock waves in the plasma fluid (Von Neumann and Richtmeyer 1950). The boundary condition used by the code is the value of the magnetic field at the plasma-vacuum boundary, or, equivalently, the total current carried by the pinch.

6.3 A simple example: linear current fall

A linearly falling current which falls from 100 kA to zero in a time t_o was incorporated into the code. The results for three different values of t_o are described in the following three sub-sections.

6.3.(i) $t_o = 100$ ns

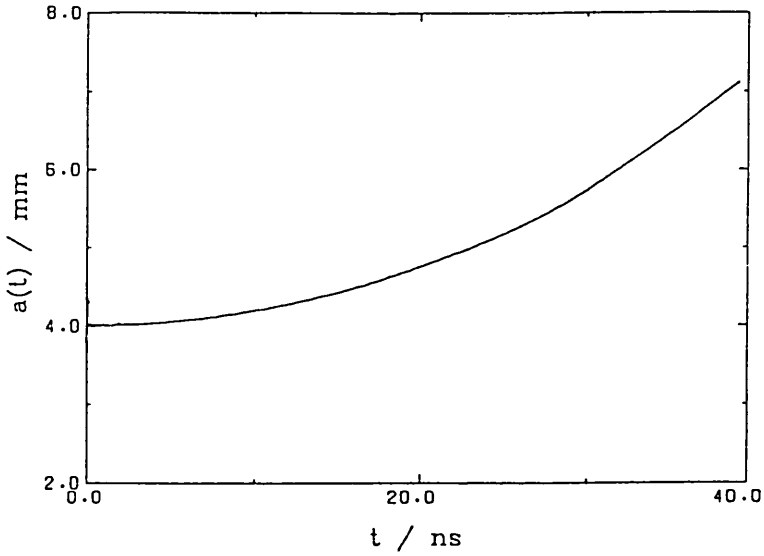


Figure 6.1 Linear current fall. Pinch radius 'a' against time. t_o = 100 ns.

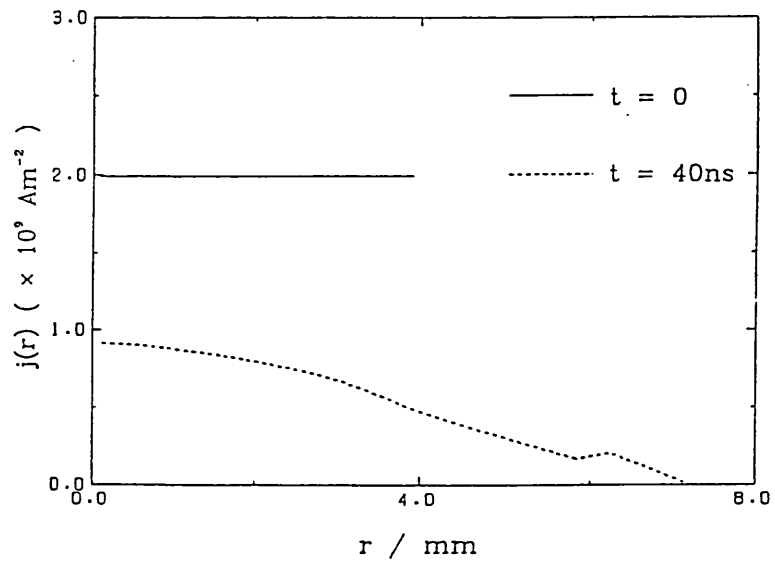


Figure 6.2 Linear current fall. Current density profiles at 0 and 40 ns. t_o = 100 ns.

In this case there is an increase in the pinch radius of about 80% in 40 ns (figure 6.1). Despite a reversed electric field at the edge of the plasma the surface current density is still positive (though reduced compared with its axial value) due to the large induced $(\underline{v} \wedge \underline{B})_z = v_r B_\theta$ electric field (figure 6.2). Nevertheless the resultant (Lorentz minus pressure gradient) force on the plasma surface is outwards, leading to the characteristic expansion associated with the inverse skin effect. The pinch number density remains a monotonically decreasing function of radius during the 40 ns of observation, and a region near the edge does not separate from the main body of plasma (figure 6.3). The expansion rate div($\underline{v}$) is highest at the plasma edge and the temperature is lowest there.

6.3.(ii) $t_o = 10$ ns

During the first 10 ns of the simulation the pinch expands as in section 6.3.(i), although in this case the surface current density reverses before t_o. After the total current reversal at 10 ns the magnetic field at the plasma edge reverses with respect to its value near the axis of the pinch and so the Lorentz force on the plasma is radially inwards. Thus after current reversal there are three regions in the pinch : (I) a central region and (III) a surface region in which the $\underline{j} \wedge \underline{B}$ Lorentz force is radially *inwards*, and (II) an annular region near the plasma edge where $\underline{j} \wedge \underline{B}$ is *outwards*. It is therefore clear that plasma may be compressed at the boundary between regions (II) and (III) resulting in a high density, high temperature region near the plasma surface. It is also clear that contraction of the pinch may occur provided that $|\underline{j} \wedge \underline{B}|$ is greater than $|\nabla p|$ at the plasma surface.

In figure 6.4 the radius of the pinch is plotted as a function of time. The initial expansion of the pinch while the current is falling but still positive is clear (c.f. figure 6.1, the corresponding regime for the $t_o = 100$ ns example), as is the contraction of the pinch long after current reversal. It is suggested that the the 'bounce' that occurs at about 20 ns has the following physical interpretation. The initial contraction (after about 14 ns) is caused by the inward $\underline{j} \wedge \underline{B}$ and ∇p forces in region (III) above. However, the plasma in region (II) is moving outwards at that time (because the pressure and Lorentz forces are outwards in this region) and it is the inertia of this large mass of plasma that causes the brief re−expansion of the pinch after about 15 ns. Eventually, since the magnitude of the (negative) current is increasing rapidly with time, the reversed magnetic field increases in magnitude at the plasma surface and diffuses inwards, so that the inwards $\underline{j} \wedge \underline{B}$ Lorentz force in region (III) dominates again and the plasma

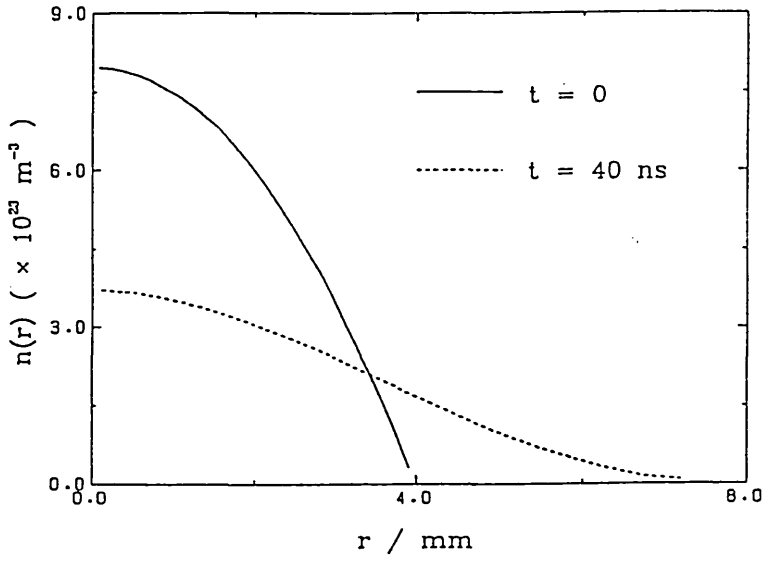


Figure 6.3 Linear current fall. Number density profiles at 0 and 40 ns. t_o = 100 ns.

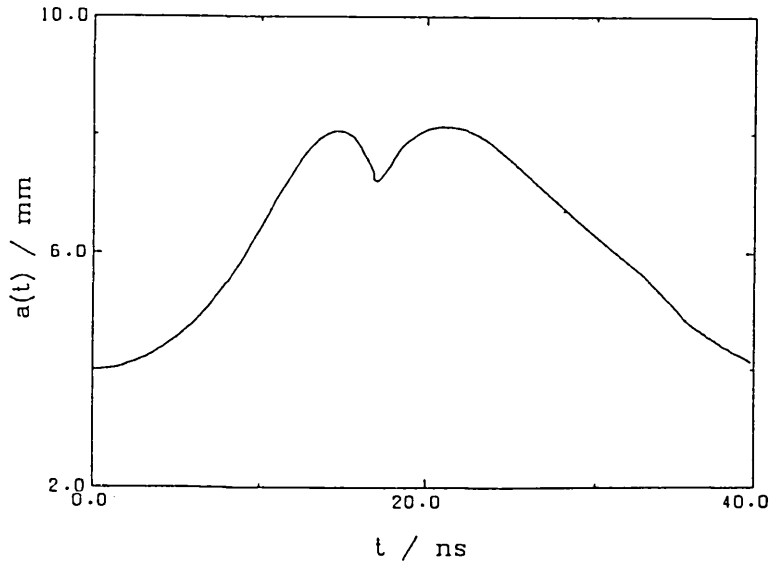


Figure 6.4 Linear current fall. Pinch radius 'a' against time. t_o = 10 ns.

contracts uniformly after about 20 ns.

In figure 6.5 the plasma number density is plotted as a function of radial position within the pinch at various times. The development of a dense annular region near the plasma surface and a hollowed out region on-axis is evident. (In passing it is also worth noting the presence at 40 ns of the shock front at $r \approx 2$ mm moving at approximately 2×10^5 ms^{-1} into the inner region wherein the sound speed is 7×10^4 ms^{-1}). Since the local bremsstrahlung emission is proportional to $n^2(r)T^{1/2}(r)$ (Glasstone and Lovberg 1960) it is clear that the dense region will radiate strongly. In figure 6.6 the total bremsstrahlung radiation from the pinch is plotted as a function of time. The radiation from the plasma decreases as the pinch expands and cools and then increases above its initial value during the post-reversal compression. This is suggested as a possible diagnostic for the formation of hollowed-out density profiles. [The neglect of radiation cooling on the dynamics of the pinch is justified since the peak current of 100 kA is less than 10% of the Pease-Braginskii limiting current.]

6.3.(iii) $t_o = 1$ ns

The effects described above are accentuated when t_o is reduced to this value.

Figure 6.7 shows the current density and magnetic field profiles at 0.5 ns, clearly demonstrating a reversed surface current density. In fact, the reversed electric field at the plasma edge drives the surface current density negative after about 0.03 ns, long before the total current reversal at 1 ns. This is because the inertia of the pinch prevents the formation of a large and positive induced $v_r B_\theta$ electric field on the 1 ns timescale. This behaviour should be contrasted with the $t_o = 100$ ns example where the surface current density remains positive for at least 40 ns - comparatively much further into the current drop than in this case.

In figure 6.8 the number density and magnetic field profiles are plotted at 4.5 ns. The emergence of a dense region containing a large magnetic flux is clear. This flux is prevented from diffusing out by the presence of a very hot (approximately 4 keV compared with the axial plasma temperature of 80 eV) inwardly moving layer. The local bremsstrahlung emission is again peaked in the dense region and the integrated bremsstrahlung emission now increases monotonically with time: the pinch does not have sufficient time to expand and cool before the current reverses and the plasma is forced to contract.

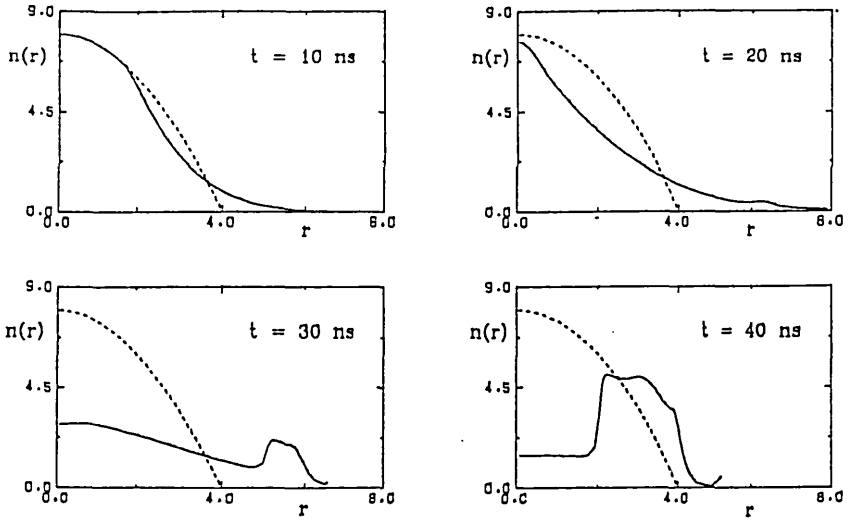


Figure 6.5 Linear current fall. Number density profiles at 10, 20, 30, and 40 ns, with initial profile shown as broken line for comparison. n(r) in 10^{23} m^{-3}, r in mm. t_o = 10 ns.

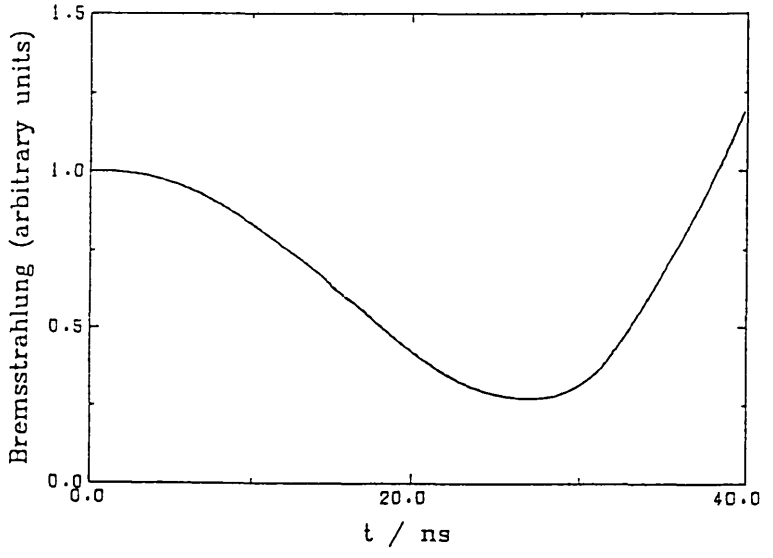


Figure 6.6 Linear current fall. Radially integrated bremsstrahlung emission (normalised to an initial value of unity) plotted as a function of time. t_o = 10 ns.

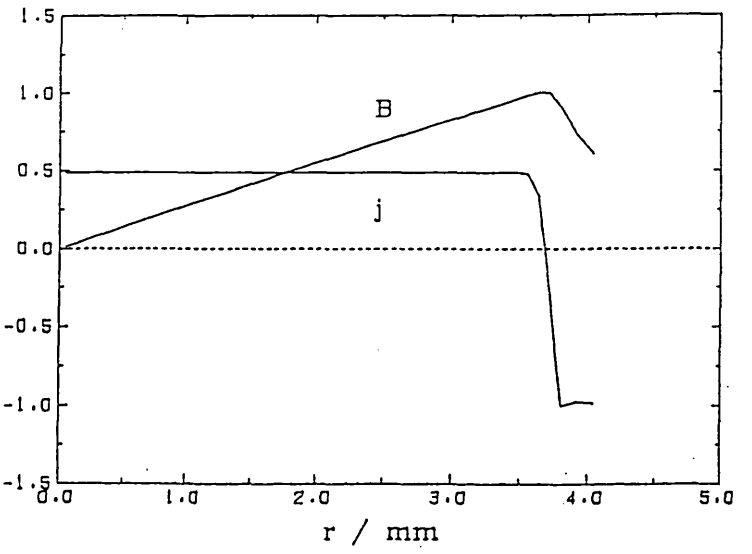


Figure 6.7 Linear current fall. Current density j and magnetic field B (normalised to a maximum value of unity) plotted against radius at 0.5 ns. t_o = 1.0 ns.

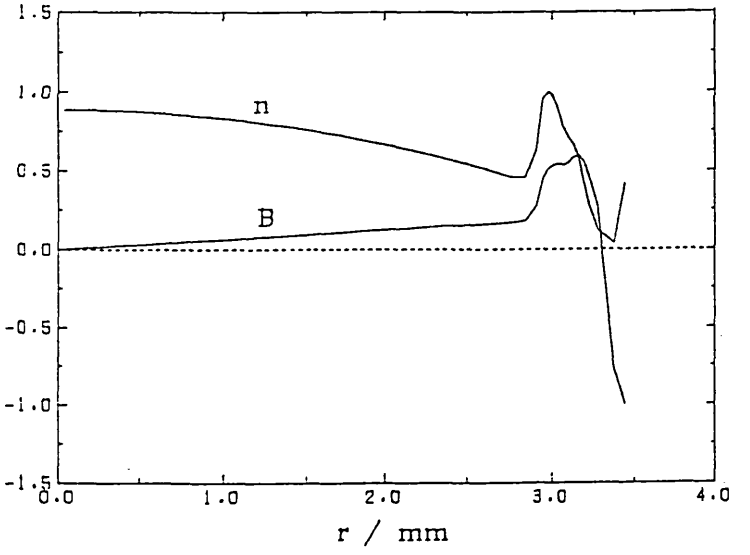


Figure 6.8 Linear current fall. Number density n and magnetic field B (normalised to a maximum value of unity) plotted against radius at 4.5 ns. t_o = 1.0 ns.

6.4 The compressional pinch

This section contains a detailed model of the Imperial College compressional Z-pinch experiment (Haines *et. al.* 1988). For part of its duration this pinch carries a falling current and therefore the expansion induced by the inverse skin effect should appear. Such an expansion has *not* been observed experimentally and this fact enables an upper bound on the rate of fall of pinch current, and therefore temperature, to be made. This estimate is of interest because the history of the pinch temperature has not been measured, although recent measurements (Baldock *et. al.* 1987) indicate that the pinch temperature does not fall significantly during the pinch's stable phase.

Briefly, the compressional pinch is formed when a 500 ns current pulse is driven through the pre-ionised hydrogen contained at a pressure of 1 torr within a cylindrical quartz tube 50 mm long and 20 mm in diameter. The discharge causes breakdown in the gas adjacent to the containing walls which then collapses under the influence of the magnetic field. The resulting shock wave heats the remaining plasma. The discharge attains a final radius of approximately one-third that of the quartz tube and remains grossly stable for the entire 500 ns of the discharge. The line density of 2×10^{19} m^{-1} is, to a good approximation, conserved throughout the duration of the experiment. A wall plasma with a thickness of about 2 mm is observed adjacent to the quartz tube.

The main circuit current rises linearly in time for about 60 ns, sustaining a peak value of about 130 kA for a further 140 ns. It then falls, approximately linearly, for 30 ns, remaining at about 30 kA for another 170 ns. Finally it reverses and falls smoothly to about -100 kA in the remaining 100 ns of observation.

The evolution of the pinch for 200 ns after peak current is modelled using the 1-D Lagrangian code described in section 2. It is assumed that an internal crow-bar is formed before peak current between the pinch and the wall plasma so that the pinch current lags behind the main circuit current by the resistive diffusion timescale of magnetic flux through the wall plasma (clearly related to the wall plasma temperature). Explicitly the pinch current in kA is taken to be:

$$I_{pinch} = I_{main} + (130 - I_{main})e^{-t/\tau} \qquad (6.1)$$

where

$$I_{main} = \begin{cases} 130 - 10t/3 \ \text{kA}, & 0 < t < 30 \ \text{ns} \\ 30 \ \text{kA} \quad , & 30 \ \text{ns} < t < 200 \ \text{ns} \end{cases} \qquad (6.2)$$

is taken as a simple but realistic model of the measured main circuit current (t = 0 being the time of peak current), and τ is the resistive diffusion timescale. Note that $\tau = 0$ implies that I_{pinch} is equal to I_{main} for all times and that $\tau = \infty$ implies that I_{pinch} remains constant at 130 kA. The main circuit current and the pinch current corresponding to $\tau = 1000$ ns are shown in figure 6.9.

The pinch is initially assumed to be in an equilibrium state with uniform current density and temperature. A crude estimate of end losses to the electrodes is made by using the result that in the large $\omega_{ce}\tau_{ei}$ limit the axial heat flux is dominated by the enthalpy flow of the electron current (Shkarofsky, Bernstein and Robinson 1963):

$$q_z = -(5/2)\ (k_B T/e)\ j_z \qquad (6.3)$$

This is probably the best estimate that can be made of the end losses in a one-dimensional model ($\partial T/\partial z = 0$). The collisionless approximation is justified since in this experiment $\langle \omega_{ce}\tau_{ei} \rangle \simeq 200$.

Pinch currents corresponding to various values of τ were driven through the plasma and the simulated pinch behaviour was followed for 200 ns. The variations in mean plasma radius for four values of are shown in table 6.1. The small decrease in radius for $\tau = \infty$ shows that heat loss to the electrodes is marginally greater than Ohmic heating for a constant current of 130 kA. For other values of τ, $\underline{j} \wedge \underline{B}$ falls sufficiently fast to allow an overall expansion of the pinch. If it is estimated that an expansion of 20% in 200 ns is the threshold of experimental observation, and remembering that the compressional pinch is *not* observed to expand significantly for at least 200 ns after peak current, it can be seen that the resistive diffusion timescale τ can be no smaller than about 1000 ns. Equating this with the 'L/R' time constant of the crowbar circuit it is possible to show that $\tau = 1000$ ns is consistent with a wall plasma temperature of about 10 eV.

Radial profiles of number density, temperature and current density at 200 ns are shown in figures 6.10, 6.11 and 6.12 respectively for the critical value of

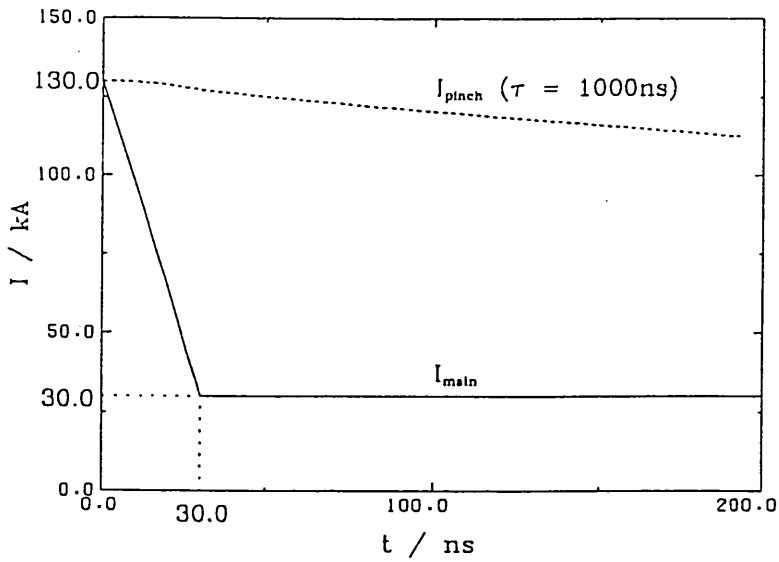


Figure 6.9 Compressional pinch. Main circuit current and pinch current (for τ = 1000 ns) plotted against time.

τ (ns)	$\Delta r_o / r_o$ (%)
∞	-1
2000	6
1000	20
500	50

Table 6.1 Compressional pinch. Fractional increase in radius in 200 ns against τ.

τ = 1000 ns. The temperature distribution remains relatively uniform across the radius except for a cool region near the plasma edge caused by the rapid expansion of that part of the pinch. Hence the Bennett temperature is very close to the temperature throughout the pinch (e.g. at 200 ns, T_B equals 98 eV and the axial temperature is 99 eV). At the critical value of τ there is a 30% decrease in the Bennett temperature of the pinch during 200 ns.

6.5 Discussion and conclusions

In this chapter a one-dimensional Lagrangian code has been used to examine the nature of the inverse skin effect in a Z-pinch. It has been shown that this effect can cause rapid expansion of a pinch, although complete detachment of a region near the surface of the pinch does not appear to occur. Physically, this is probably because magnetic flux would have to diffuse through any part of the plasma that detached itself in order to provide a vacuum flux between the detached and the remaining plasma, and this process occurs on the same timescale as the diffusion of current into the plasma. Hence the localised reversed current that could drive a plasma separation would diffuse away before the detachment could develop.

If the total current reverses (rather than just decreases), it was found that plasma could be trapped between two regions where the Lorentz forces are oppositely directed. It was suggested that the establishment of a hot dense region just inside the plasma surface could lead to an observable increase in the total bremsstrahlung emission of the pinch.

The surface reversed current density and the hollowing out of the number density profiles are in agreement with the experimental results of Jones and Silawatshananai. For the reason discussed above it is suggested that the luminous outer region observed in their experiment was *not* caused by the detachment of a plasma sheath but by plasma at the surface of the radially expanding pinch accumulating at the wall of the containing vessel.

By using the code to model the Imperial College compressional pinch experiment it was possible to obtain an upper bound on the rate of fall of pinch current which remains consistent with experimental observations. Assuming this rate of fall of current, it is possible to estimate $\int\gamma\ dt$, the number of ideal MHD growth times for which the pinch appears to be stable, where the growth rate γ

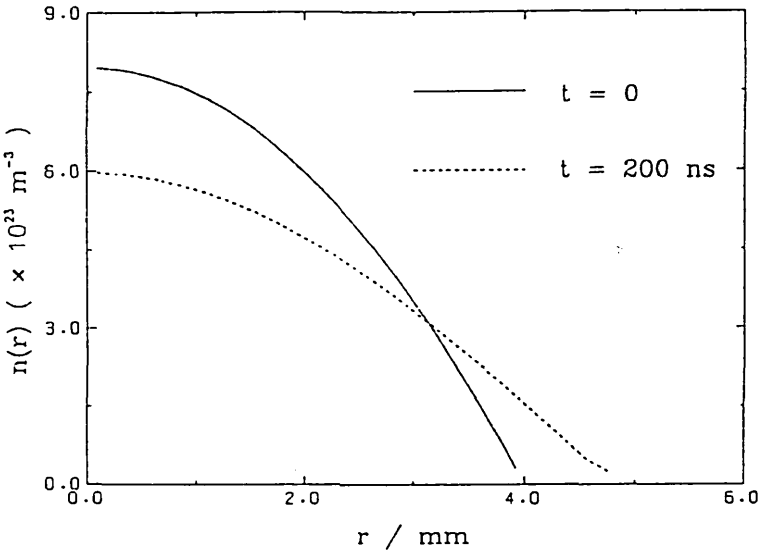


Figure 6.10 Compressional pinch. Number density profiles at 0 and 200 ns. τ = 1000 ns.

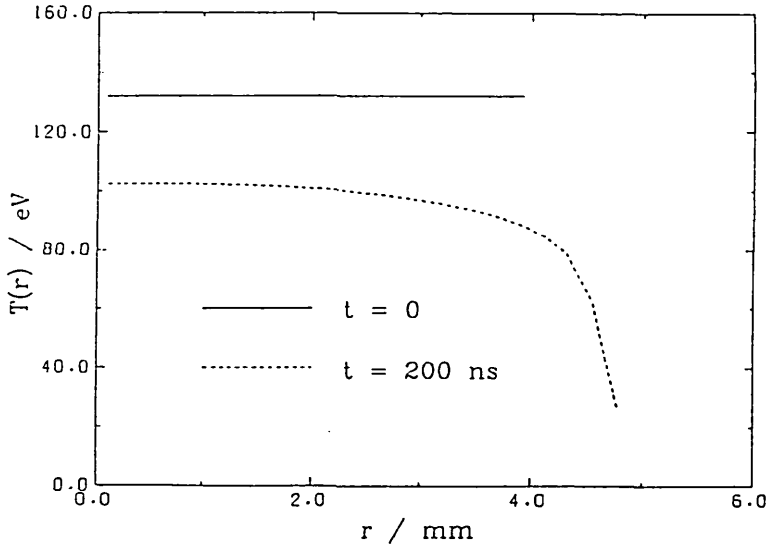


Figure 6.11 Compressional pinch. Temperature profiles at 0 and 200 ns. τ = 1000 ns.

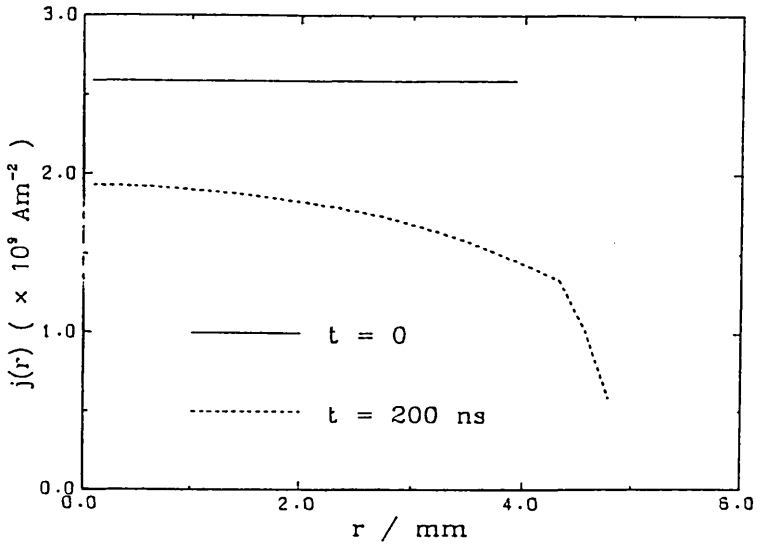


Figure 6.12 Compressional pinch. Current density profiles at 0 and 200 ns. τ = 1000 ns.

is approximated by the inverse of the ion thermal transit time at the Bennett temperature. The 200 ns period of observation can then be shown to correspond to at least *8* ideal MHD growth times. Given that the pinch is observed to remain stable for a further 100 ns, and that $\tau = 1000$ ns gives the *maximum* possible rate of cooling of the pinch, it is clear that the pinch displays anomalous stability. This is unlikely to be due to resistivity as the Lundquist number at peak current is of the order of 1000. It could, however, be due to the largely *collisionless* nature of the pinch (Freidberg's parameter $x \simeq 26$); a number of authors have described enhanced stability in this regime (Coppins 1989, Faghihi and Scheffel 1987). Alternatively, since Freidberg's parameter $y \simeq 0.13$, it may be that finite Larmor radius stabilisation (e.g. Rosenbluth *et. al.* 1962, Roberts and Taylor 1962) can explain the pinch's longevity.

As a footnote to this chapter it is worth noting that inverse skin effect may explain the large expansion observed in the NRL fibre pinch experiments when the current falls rapidly from its maximum value (Sethian *et. al.* 1987). It does not, of course, explain the development of instabilities at this time or their attendant neutron bursts.

CHAPTER SEVEN

CONCLUSIONS AND DISCUSSION

7.1 Introduction

The work presented in this thesis consists of a series of investigations into various aspects of Z-pinch theory relevant to the current and future generations of Z-pinch experiments. This final chapter contains a brief review and discussion of the main results of the work, together with suggestions of ways in which the studies presented here could be improved and generalised.

7.2 Chapter one

Chapter one stressed that ideal MHD is a legitimate model of plasma behaviour only if the three conditions of low collisionality, small ion Larmor radius, and low resistivity are satisfied. It was shown that in a Z-pinch these three criteria enable the $I^4 r_o - N$ plane to be partitioned into the various regions defined by figure 1.5. This figure demonstrates that the high line density deuterium fibre Z-pinch experiments performed at the Naval Research Laboratory and at the Los Alamos National Laboratory in the U.S.A. only enter the ideal MHD regime just before peak current. It was therefore suggested that the 'anomalously' stable behaviour of these pinches may be caused by the effects of resistivity in the early phases of the experiments.

It was also shown that the timescale on which an Ohmically heated Z-pinch evolves, τ_{ohm}, and the timescale for the development of ideal MHD instabilities, τ_{mhd}, are related by

$$\tau_{ohm}/\tau_{mhd} \sim \mu_o r_o V_A/\eta \sim S \qquad (7.1)$$

where the Lundquist number S is the ratio of the inductive to the resistive terms in Ohm's law (i.e. $S \sim |\underline{v} \wedge \underline{B}|/|\eta \underline{j}|$). Equation 7.1 shows that when resistivity is important ($S << 1$) it is essential to include the time-dependence of the equilibrium since in that case $\tau_{ohm} << \tau_{mhd}$; conversely when resistivity is negligible ($S >> 1$) *ideal* MHD is valid and the equilibrium can be assumed to

be in a steady state (figure 1.6).

The above two points provide the motivation for and the methodology of the rest of the thesis − a study of the stability of resistive *and therefore* time−dependent Z−pinch equilibria.

7.3 Chapter two

Two classes of time−dependent Z−pinch equilibrium were discussed. The first type is stationary ($\underline{v} \equiv \underline{0}$), held in pressure balance by a rising current ($I \propto t^{1/3}$); the second type expands ($\underline{v} = (r/t, 0, 0)$) while carrying a falling current ($I \propto t^{-1/3}$).

In the collisionless low current phase, equilibria were found by neglecting thermal conductivity. The stationary type were found to be characterised by a monotonically increasing number density while the non−stationary type were found to have a well defined edge where the number density vanished.

In the more realistic case of finite thermal conductivity the form of the equilibria were found to depend critically on the magnitude of a dimensionless free parameter Ω, equal to the ratio of the magnetic field diffusion time to the Ohmic heating timescale. For the stationary equilibria there was found to be a critical value of Ω, $\Omega_{crit} \simeq 3.43$. For Ω below this value the equilibria are 'gas−embedded', being characterised by a finite edge density and heat flow out of the plasma; when Ω equals Ω_{crit} both these quantities vanish and the equilibria are 'thermally isolated'; and for Ω greater than Ω_{crit} the equilibria possess a finite thermal pressure at edge where the number density vanishes, the resultant pressure difference across the boundary being balanced by a magnetic pressure difference associated with a *skin current* at the plasma surface. The magnitude of the skin current was shown to increase monotonically with Ω for $\Omega > \Omega_{crit}$ (figure 2.8) and this behaviour was given a simple physical explanation. In the non−stationary case there was shown to be another critical value of Ω, $\Omega_{crit} \simeq 1.25$, *below* which the equilibria are gas−embedded, *at* which the become thermally isolated and *above* which they carry skin currents at the plasma surface. In this case however there is a limiting value of Ω, $\Omega_{max} \simeq 1.96$, just below which the skin current *reverses* and above which the equilibria have to be rejected on physical grounds (figure 2.16). A physical explanation of this behaviour was also given.

Analytical solutions for both types of equilibrium were obtained in the infinite thermal conductivity (uniform temperature) limit. The first solution is well known, the second is new. Remarkably, the *same* critical values of Ω appear in the analytical solutions as in the finite thermal conductivity cases.

Work has recently been done by Glasser (1989) which generalises the work of chapter two by including all of Braginskii's transport terms and discarding the assumption of exact pressure balance, while retaining the assumption of cylindrical symmetry. These quasi-equilibria can be found for any power law time-dependence of the plasma current, not just the $t^{1/3}$ and $t^{-1/3}$ cases that were studied here. The same range of profiles, from 'gas-embedded' to 'thermally isolated with a skin current' still appears, although the precise details (the value of Ω_{crit} etc) are of course different. Glasser's work effectively concludes the study of one-dimensional time-dependent Z-pinch equilibria.

7.4 Chapter three

This chapter contained a study of the ideal MHD stability of the stationary finite and infinite thermal conductivity equilibria of chapter two.

It was shown that the distribution of the plasma temperature, either in the equilibrium or in the perturbation, has very little effect on the stability of a Z-pinch in the high temperature regime.

It was also shown that the variation in the ideal MHD growth rate, over the entire range of accessible equilibria (Ω: $\Omega_{crit} \rightarrow \infty$, I_{skin}/I_{total}: $0 \rightarrow 100\%$) is very small, being less than 50% even in the most pronounced case of short wavelength $m = 1$ instabilites. From this it was deduced that the enhanced stability of the fibre pinch experiments could not be explained on the basis of the development of a particularly stable equilibrium in the ideal phase.

7.5 Chapter four

In this chapter the development of axisymmetric perturbations in a time-dependent Z-pinch equilibrium was studied by using a one-dimensional linearised initial value code. It was shown that there is a period of stability at early times (low currents) before the pinch enters the ideal MHD regime and

develops catastrophic instabilities. It was shown that this region could be described in terms of a critical Lundquist number $S^* \geqslant 50$ for $kr_o \leqslant 1$ modes.

S^* is determined to within a factor of about 3 since it depends on the form of the initial perturbation, but lower and upper bounds on S^* were calculated by using perturbations that were respectively 'parallel' and 'orthogonal' to the mode which ultimately emerges from the system when the pinch enters the ideal regime.

The following variation of the mean critical Lundquist number with wavelength was found:

$$\langle S^* \rangle \simeq 50\ (kr_o)^{-0.86}. \qquad (7.2)$$

This shows that for long wavelength modes (say $kr_o < 1$) the region of validity of ideal MHD is much smaller than the intuitve estimate $S^* = 1$ would suggest. If the revised threshold of instability is taken to be $S^* = 100$, then the line $y^2/x = 1$ in figure 1.5 must be translated *upwards* by a factor of $\log_{10}(100) = 2$, which puts the points marked 'NRL' and 'LANL' in the *resistive, stable* regime. Result 7.2 therefore offers a partial explanation of the 'anomalous' stability displayed by these pinches during the current rise: they simply do not reach the ideal phase (with its catastrophic instabilities) before the current maximum, and consequently they are stable during this time.

It was shown that the scaling with wavelength of equation 7.2 could be explained analytically by the rate of change of the equilibrium, but that the proportionality constant (50) could only be explained by the effects of resistivity directly on the development of the *perturbation.*

Equation 7.2 does not (and was not intended to) explain the sudden development of $m = 0$ instabilities *after* peak current, nor does it explain why short wavelength modes ($kr_o > 1$) fail to develop while the current is rising, although it is hoped that the inclusion of viscosity, an effect neglected in this analysis, will provide a solution to the second problem. Work on the effects of viscosity is currently being undertaken by the author and by Cochran (private communication 1989) and by Nebel (private communication 1989). No results are available yet.

Other possible modifications to the work of chapter four include the

incorporation of finite thermal conductivity, allowing the formation of temperature gradients in the equilibrium and the perturbation; the use of Glasser's quasi-equilibria to study the realistic case of a *linearly* rising current: on the basis of the analytical model described earlier this might be expected to alter the way in which S^* varies with kr_0, although it might be hoped that the magnitude of S^* would remain approximately the same as long as the the pinch expands much more slowly than the Alfven speed; and the inclusion of bremsstrahlung radiation, which could be a significant element in the next generation of fibre pinches, which are designed to carry a peak current of 1 MA. Since $S \propto I^4 r_0/N^2$, it seems that if resistivity is the *only* stabilising mechanism then the new pinches will probably go unstable *before* peak current.

7.6 Chapter five

This chapter contained a study, analagous to the m = 0 case in chapter four, of the development of helical (m = 1) instabilities in a time-dependent Z-pinch equilibrium by using a one-dimensional linearised initial value code. A critical Lundquist number S^* was found, below which the pinch is resistively stabilised and above which it develops ideal MHD instabilities. The mean value of S^*, averaged over all forms of initial perturbation, was found to vary with kr_0 as

$$\langle S^* \rangle \simeq 40\ (kr_0)^{-0.75}. \qquad (7.3)$$

Comparison of this result with eqn. 7.2 shows that m = 0 and m = 1 modes are stabilised to a comparable degree by resistivity, reinforcing the conclusion of chapter four that the enhanced stability of the deuterium fibre pinch experiments is due at least in part to resistive effects in the early part of the discharge.

Because of the similarity of the results of this chapter to those of chapter four, it seems sensible to postpone any generalisation of this work until the (simpler) corresponding generalisation of the m = 0 work has been completed.

7.7 Chapter six

This chapter was concerned with the inverse skin effect and in particular its occurrence in the Imperial College compressional pinch experiment. This effect is the reduction of the plasma surface current density following a decrease in the

total pinch current, and is usually associated with an expansion of the pinch.

Numerical simulation of a simple example of the inverse skin effect demonstrated that:

(i) If the current falls sufficiently fast then the current density at the pinch surface can *reverse*; otherwise it is kept positive by the large induced $(\underline{v} \wedge \underline{B})_z = v_r B_\theta$ electric field.

(ii) The outer region of the pinch does *not* detach itself from the main body of plasma during the current fall.

(iii) If the total current reverses, then a hot dense layer can appear between two regions where the Lorentz $\underline{j} \wedge \underline{B}$ forces are oppositely directed, leading to increased bremsstrahlung emission from the pinch.

The same code was used to model the compressional pinch. By assuming that the pinch current 'crow−barred' through a wall plasma circuit after peak current, it was possible to estimate the maximum rate of current fall, and therefore rate of cooling, that is consistent with the experimentally observed lack of expansion of the pinch after peak current. The maximum rate of fall of current is compatible with a wall plasma temperature of no less than 10 eV. Using this result it was shown that the pinch remains stable for *at least 8* ideal MHD growth times and is therefore anomalously stable with respect to this theory. It was suggested that either finite Larmor radius effects or the collisionless nature of the pinch might explain this stability, although no calculations to support these suggestions have been done. It would be interesting to see if these effects are sufficient to account for the stability or whether some more exotic stabilising mechanism is necessary to explain the pinch's longevity.

REFERENCES

Alfven H, (1950), "Cosmical Electrodynamics", (OUP).

Appert K, Gruber R and Vaclavik J, (1974), Phys. Fluids, 17, 1471.

Atkinson R E and Houtermans F G (1929), Z. Phys., 54, 9.

Baldock P, Coppins M, Culverwell I D and Dangor A E, (1987), Bull. Am. Phys. Soc., 32, No. 9, 1757, Paper 2T 9.

Bateman G, (1978) "MHD Instabilities" (MIT, Cambridge, Mass., (USA)).

Bennett W H, (1934), Phys. Rev., 45, 890.

Bernstein I B, Frieman E A, Kruskal M D and Kulsrud R M, (1958), Proc. Roy. Soc. Lond., A224, 17.

Braginskii S I, (1965), in "Reviews of Plasma Physics", (ed. M A Leontovich, Consultants Bureau, New York), Vol. 1, 205.

Braginskii S I and Shafranov R D, (1959), in "Plasma Physics and the Problem of Controlled Thermonuclear Reactions", (ed. M A Leontovich, Pergamon, London), 39.

Carruthers R and Davenport P A, (1957), Proc. Phys. Soc., B70, 49.

Cochran F L and Robson A E, (1989), to appear in Phys. Fluids B.

Coppins M, (1988), Plas. Phys. and Cont. Fusion, 30, 201.

Coppins M, (1989), Phys. Fluids, B1, 591.

Coppins M, Culverwell I D and Haines M G, (1988), Phys. Fluids, 31, 2688.

Cousins A W and Ware A A, (1951), Proc. Phys. Soc., B64, 159.

Culverwell I D, (1988), Imperial College internal report DZP/P46.

Culverwell I D and Coppins M, (1989a), Plas. Phys. and Cont. Fusion, 31, 1443.

Culverwell I D and Coppins M, (1989b), to appear in Phys. Fluids B.

Culverwell I D, Coppins M, Haines M G, Bell A R and Rickard G J, (1989), Plas. Phys. and Cont. Fusion, 31, 387.

Dangor A E, Favre Dominguez M B, Lee S and Kahan E, (1983), Phys. Rev., A27, 2751.

Faghihi M and Scheffel J, (1987), J. Phys. D (Appl. Phys.), 11, 1709.

Favre-Dominguez M B, (1985), PhD thesis, University of London.

Freidberg J P, (1982), Rev. Mod. Phys., 54, 801.

Gear C W, (1971), "Numerical Initial Value Problems in Ordinary Differential Equations", (Prentice Hall Inc., Englewood Cliffs, NJ (USA)).

Glasser A H, (1989), to appear in J. Comp. Phys.

Glasstone S and Lovberg R H, (1960), "Controlled Thermonuclear Reactions", Chap. 2 (Von Nostrand, Scarborough, CA (USA)).

Goedbloed J P, (1979), "Lecture Notes on Ideal Magnetohydodynamics",

(Fom-Institut voor Plasmafysica, Nieuwegein, Netherlands).

Goedbloed J P and Sakanaka P H, (1974), Phys. Fluids, 17, 908.

Haines M G, (1959), Proc. Phys. Soc., 74, 576.

Haines M G, (1960), Proc. Phys. Soc., 76, 249.

Haines M G, (1982), Phys. Scripta, T2/2, 380.

Haines M G, Bayley J, Baldock P, Bell A R, Chittenden J P, Choi P, Coppins M, Culverwell I D, Dangor A E, Figura E S, McCall G, and Rickard G J, (1988), Proc. 12th International Conference on Plasma Physics and Controlled Nuclear Fusion Research (Nice), Paper IAEA-CN-50/C-4-4-2.

Haines M G, Coppins M and Culverwell I D, (1989), to appear in Proc. of 2nd International Conference on High Density Z-pinches (Laguna Beach, CA (USA)).

Hammel J E, (1976), LANL report LA-6023-MS.

Hammel J E and Scudder D W, (1987), Proc. Fourteenth Euro. Conf. on Cont. Fusion and Plasma Phys., Part 2, 450.

Jones I R and Silawatshananai C, (1980), Plas. Phys., 22, 501.

Kadomtsev B B, (1966), in "Reviews of Plasma Physics", ed. M A Leontovich, (Consultants Bureau, New York), Vol. 2.

Kanellopoulos S, Coppins M and Haines M G, (1988), J. Plas. Phys., 39, 521.

Kruskal M and Schwarzchild M, (1954), Proc. Roy. Soc., A223, 348.

Laval G, Mercier C and Pellat R M, (1965), Nucl. Fusion, 5, 156.

Lawson J D, (1957), Proc. Phys. Soc., B70, 6.

Mathews J and Walker R L, (1970), "Mathematical Methods of Physics", (Addison Wesley), 2nd edition.

McCall G H, (1988), Proc. 2nd International Conference on Z-pinch and Plasma Focus, (Nice), 200.

Newcomb W A, (1958), Ann. Phys, 3, 347.

Pease R S, (1957), Proc. Phys. Soc. B70, 11.

Potter D, (1973), "Computational Physics", (Wiley, London).

Roberts K V and Taylor J B, (1962), Phys. Rev. Lett., 8, 197.

Robson A E, (1984), Proc. 1st International Conference on High Density Z-pinches, (Alexandria, VA, (USA)), 2.

Rosenau P, Nebel R A and Lewis H R, (1989), Phys. Fluids, B1, 1233.

Rosenbluth M N, Krall N A and Rostoker N, (1962), Nucl. Fusion Suppl., Part 1, 143.

Schkarofsky I P, Bernstein I B and Robinson B B, (1963), Phys. Fluids, 6, 40.

Schmidt G, (1979), "Physics of High Temperature Plasmas", second edition, (Academic Press, New York).

Sethian J D, Robson A E, Gerber K A and DeSilva A W, (1987), Phys. Rev. Lett., 59, 892; *ibid.* 1790.

Stratton J A, (1941), "Electromagnetic Theory", (McGraw−Hill, New York).

Tayler R J, (1957a), Proc. Phys. Soc., B70, 31.

Tayler R J, (1957b), Proc. Phys. Soc., B70, 1049.

Tayler R J, (1960), Harwell Report AERE T/R 3100.

Thonemann P C, (1950), Nature, 166, 903.

Tonks L, (1939), Phys. Rev., 56, 360.

Von Neumann J and Richtmeyer R D, (1950), J. Appl. Phys., 21, 232.